

DISSERTATION

REGIONAL ANALYSIS OF CONVECTIVE SYSTEMS DURING THE WEST  
AFRICAN MONSOON

Submitted by

Bradley Nicholas Guy

Department of Atmospheric Science

In partial fulfillment of the requirements

For the degree of Doctor of Philosophy

Colorado State University

Fort Collins, Colorado

Spring 2012

Doctoral Committee:

Advisor: Steven Rutledge  
Co-Advisor: Wei-Kuo Tao

Christian Kummerow  
Sue van den Heever  
Rob Cifelli  
Steven Reising

## ABSTRACT

### REGIONAL ANALYSIS OF CONVECTIVE SYSTEMS DURING THE WEST AFRICAN MONSOON

The West African monsoon (WAM) occurs during the boreal summer and is responsible for a majority of precipitation in the northern portion of West Africa. A distinct shift of precipitation, often driven by large propagating mesoscale convective systems, is indicated from satellite observations. Excepting the coarser satellite observations, sparse data across the continent has prevented understanding of mesoscale variability of these important systems. The interaction between synoptic and mesoscale features appears to be an important part of the WAM system. Without an understanding of the mesoscale properties of precipitating systems, improved understanding of the feedback mechanism between spatial scales cannot be attained. Convective and microphysical characteristics of West African convective systems are explored using various observational data sets. Focus is directed toward meso  $\alpha$  and  $\beta$  scale convective systems to improve our understanding of characteristics at this spatial scale and contextualize their interaction with the larger-scale.

Ground-based radar observations at three distinct geographical locations in West Africa along a common latitudinal band (Niamey, Niger [continental], Kawsara, Senegal [coastal], and Praia, Republic of Cape Verde [maritime]) are analyzed to determine convective system characteristics in each domain during a 29 day period in 2006. Ancillary datasets provided by the African Monsoon Multidisciplinary Analyses

(AMMA) and NASA-AMMA (NAMMA) field campaigns are also used to place the radar observations in context.

Results show that the total precipitation is dominated by propagating mesoscale convective systems. Convective characteristics vary according to environmental properties, such as vertical shear, CAPE, and the degree of synoptic forcing. Data are bifurcated based on the presence or absence of African easterly waves. In general, African easterly waves appear to enhance mesoscale convective system strength characteristics (e.g. total precipitation and vertical reflectivity profiles) at the inland and maritime sites. The wave regime also resulted in an increased population of the largest observed mesoscale convective systems observed near the coast, which led to an increase in stratiform precipitation. Despite this increase, differentiation of convective strength characteristics was less obvious between wave and no-wave regimes at the coast. Due to the propagating nature of these advecting mesoscale convective systems, interaction with the regional thermodynamic and dynamic environment appears to result in more variability than enhancements due to the wave regime, independent of location.

A 13-year (1998–2010) climatology of mesoscale convective characteristics associated with the West African monsoon are also investigated using precipitation radar and passive microwave data from the NASA Tropical Rainfall Measuring Mission satellite. Seven regions defined as continental northeast and northwest, southeast and southwest, coastal, and maritime north and south are compared to analyze zonal and meridional differences. Data are categorized according to identified African easterly wave (AEW) phase and when no wave is present. While some enhancements are observed in association with AEW regimes, regional differences were generally more

apparent than wave vs. no-wave differences. Convective intensity metrics confirm that land-based systems exhibit stronger characteristics, such as higher storm top and maximum 30-dBZ heights and significant 85-GHz brightness temperature depressions. Continental systems also contain a lower fraction of points identified as stratiform. Results suggest that precipitation processes also varied depending upon region and AEW regime, with warm-rain processes more apparent over the ocean and the southwest continental region and ice-based microphysics more dominant over land, including mixed-phase processes. AEW regimes did show variability in stratiform fraction and ice and liquid water content, suggesting modulation of mesoscale characteristics possibly through feedback with the synoptic environment.

Two mesoscale convective systems (MCSs) observed during the African Monsoon Multidisciplinary Analyses (AMMA) experiment are simulated using the three-dimensional (3D) Goddard Cumulus Ensemble model. One of the MCSs, the 8 September 2006 system, is associated with the passage of an African easterly wave trough while the other, the 14 July 2006 case, is not. Simulations are performed using 1 km horizontal grid spacing, a lower limit on current embedded cloud resolving models within a multi-scale modeling framework. Simulated system structure is compared to radar observations using contoured frequency-by-altitude diagrams (CFADs), calculated ice and water mass, and identified hydrometeor variables. Results indicate general agreement in the temporal distribution of hydrometeors. Vertical distributions show that ice hydrometeors are often underestimated at mid- and upper-levels, partially due to the inability of the model to produce adequate system heights. Abundance of high reflectivity values below and near the melting level in the simulation led to a broadening

of the CFAD distributions. Observed vertical reflectivity profiles indicate larger reflectivities aloft compared to simulated values. Despite these differences and biases, the radar–observed differences between the two cases are noticeable in the simulations as well, suggesting that the model is able to capture gross observed differences between the two MCSs.

## ACKNOWLEDGEMENTS

I would like to convey my utmost appreciation to my advisors, Drs. Steven Rutledge and Wei-Kuo Tao, for this opportunity. I would especially like to thank Dr. Steven Rutledge for his continual encouragement, support, and mentorship regarding my research and his advice and support of various career advancement opportunities. I would also like to acknowledge my committee members: Drs. Chris Kummerow, Sue van den Heever, Rob Cifelli, and Steven Reising for their comments and suggestions which benefited this research greatly.

Discussions with Drs. Karen Mohr, Xiping Zeng, Tom Rickenbach, Earle Williams, Chris Thorncroft, and the entire Mesoscale Dynamics and Modeling Group at the NASA Goddard Space Flight Center were extremely beneficial and enjoyable. Thank you to the AMMA community for their hard work and planning for acquiring data across West Africa and making the data easily available to researchers around the globe. My gratitude goes out to Dr. Gareth Berry for making the African easterly wave tracking code available; and Dr. Chuntao Liu for his gracious help with accessing and processing the University of Utah TRMM Precipitation Feature database.

Also, a special thanks is in order to the CSU radar group for their advice and friendship and to coffee group for their advocacy of caffeinating and humor over the years, both essential to finishing this work. Finally, but most importantly, I would like to thank my wife, Carrie, and my daughter, Micah, for dealing with a sleep-deprived (and sometimes cranky) graduate student in the house and for their absolute support during this endeavor. I could not have accomplished this without them.

This research was supported by the Center for Earth and Atmospheric Studies (CEAS) fellowship grant NNX08AT77G and NASA Precipitation Measurement Mission under grant NNX10AG88G.

## TABLE OF CONTENTS

<b>PART I: INTRODUCTION TO THE DISSERTATION .....</b>	<b>1</b>
<b>PART II: RADAR CHARACTERISTICS OF CONTINENTAL, COASTAL, AND MARITIME CONVECTION OBSERVED DURING AMMA/NAMMA .....</b>	<b>4</b>
1. INTRODUCTION.....	5
2. DATA AND METHODOLOGY .....	10
2.1. Radar data and precipitation feature analysis .....	10
2.2. Radiosonde data.....	13
2.3. Reanalysis data and easterly wave analysis.....	14
3. RESULTS.....	18
3.1. Study area and environmental characteristics.....	18
3.2. Precipitation characteristics .....	23
3.3. Convective characteristics and easterly waves .....	26
4. CONCLUSIONS .....	42
REFERENCES .....	47
<b>PART III: REGIONAL COMPARISON OF WEST AFRICAN CONVECTIVE CHARACTERISTICS: A TRMM-BASED CLIMATOLOGY.....</b>	<b>55</b>
1. INTRODUCTION.....	56
2. DATA AND METHODOLOGY .....	61
3. RESULTS.....	70
3.1. Precipitation feature characteristics .....	70
3.2. Vertical structure.....	74
3.3. Microphysical characteristics .....	79
4. CONCLUSION .....	96
REFERENCES .....	101
<b>PART IV: GODDARD CUMULUS ENSEMBLE MODEL PERFORMANCE ON SAHELIAN MESOSCALE CONVECTIVE SYSTEMS.....</b>	<b>109</b>
1. INTRODUCTION.....	110

2. SIMULATION SETUP .....	113
3. OBSERVATIONAL DATA .....	116
4. SYNOPTIC AND MESOSCALE DESCRIPTION .....	121
4.1. 8 September 2006 case .....	121
4.2. 14 July 2006 case.....	123
5. OBSERVATIONAL DISCUSSION .....	131
6. SIMULATION DISCUSSION.....	137
7. SUMMARY AND CONCLUSIONS.....	151
REFERENCES .....	155
<b>PART V: OVERALL SUMMARY AND DISCUSSION .....</b>	<b>162</b>
REFERENCES .....	172

**LIST OF TABLES**

**PART I**..... 1

**PART II**..... 4

    1.1. Sampling characteristics and locations of TOGA, NPOL, and MIT radars..... 9

    2.1. Data and methodology characteristics for TOGA, NPOL, and MIT radars. .... 16

    3.1. Convective system characteristics derived from precipitation feature analysis for all study times and within AEW and no-wave regimes..... 30

    3.2. Contribution of AEW regime precipitation features as a function of study period totals. .... 31

    4.1. Comparison of key characteristics for each location during 19 August – 16 September 2006..... 45

    4.2. AEW regime characteristics in relation to no-wave regime characteristics during 19 August – 16 September 2006. .... 46

**PART III**..... 55

    2.1. Number of precipitation features identified using TRMM precipitation radar and associated with objectively analyzed African easterly wave phase in northern regions in this study..... 66

    2.2. Number of precipitation features identified using TRMM precipitation radar and associated with objectively analyzed African easterly wave phase in southern regions in this study..... 67

    3.1. Mean values of properties associated with precipitation features in the seven study regions – maritime north (MarN) and south (MarS), coastal, continental northwest (ConNW), northeast (ConNE), southwest (ConSW) and southeast (ConSE) – during May–October, 1998–2010. .... 82

**PART IV** ..... 109

    6.1. Mean fraction skills score (FSS) of reflectivity distributions coinciding with observational time period and with model shifted for best agreement. Scores were calculated at each corresponding grid height of MIT radar observations and degraded GCE simulations..... 143

**PART V**..... 162

## LIST OF FIGURES

<b>PART I</b> .....	1
<b>PART II</b> .....	4
2.1. Map of West Africa with shaded topography. The three radar systems are located at the cross-hairs, with the encircled regions showing the approximate observational scan range. Objectively identified AEJ axis (dashed line) and AEW troughs (solid lines) are shown for 8 September 2006 at 1200 UTC, with trough ('T') and ridge ('R') positions labeled. ....	17
3.1. Time-longitude plot of TRMM 3B42 gridded rainfall product averaged between 12–17°N. Contours represent percentage of rainfall above threshold value (0.8 mm h-1, mean value during 2006 season), with greater values representing increased areas of rain rates in observed systems – a proxy for size of precipitating system. Exclusion of data below 12°N was used to reduce “noise” present from the southern track of precipitation associated with the summer monsoon. Objectively identified AEW trough tracks are overlaid (black lines), with all tracks that persist for less than 1.5 days and 8 degrees in longitudinal length filtered out. Vertical, dashed lines show the location of each radar system in the study. The bottom plot denotes mean elevation between 12–17°N.....	32
3.2. Time series of (a) radar-estimated unconditional rainfall rate, (b) CAPE, and (c) CIN for the continental location, 19 August – 16 September 2006. Hatched, vertical bars indicate the presence of AEW troughs within 500 km of the site. Arrow heads along the CIN plot abscissa indicate the first radar echo occurrence of mesoscale convective systems of large spatial (> 1000 km <sup>2</sup> ) and temporal (> 3 h) extent. ....	33
3.3. As in Fig. 3.2, but for the coastal location. ....	34
3.4. As in Fig. 3.2, but for the maritime location. ....	35
3.5. Frequency distribution of calculated environmental variables for the maritime (a–c), coastal (d–f), and continental (g–i) locations. CAPE (top row), CIN (middle row), and low-level shear (bottom row) are shown. Black bars represent values calculated during an AEW regime, while gray bars denote no-wave regime calculations. ....	36
3.6. Mean zonal (solid lines) and meridional (dashed lines) vertical wind profiles for the (a) maritime, (b) coastal, and (c) continental locations. Mean rawinsonde profiles are shown for the African easterly wave (black) and no-wave (gray) regimes. ....	37

3.7. Mean velocity azimuth display divergence profiles for the (a) maritime, (b) coastal, and (c) continental locations. Profiles of 40 km annuli centered about ranges of 24, 44, 60, and 76 km from the radar are averaged for AEW (black) and no-wave (gray) regimes. Profiles are made up of both convective and stratiform components.....	38
3.8. Contribution by precipitation features, at the maritime (solid line), coastal (dotted line) and continental (dashed line), to (a,d) total volumetric rainfall as a function of mean (a-c) 20 dBZ and (d-f) 30 dBZ echo-top heights. Convective (b,e) rain volume-weighted reflectivity occurrence distributions normalized by maximum occurrence were used to illuminate the convective mode of precipitation. The same methodology was used for stratiform (c,f) contributions. ....	39
3.9. Difference in cumulative frequency distributions between AEW and no-wave regimes for a) precipitation feature area, b) convective and c) stratiform volumetric rainfall. Maritime (solid line), coastal (dotted line), and continental (dashed line) locations are shown. Positive values correspond to an increase during the AEW regime. Less (more) volumetric rainfall may be interpreted as a decrease (increase) in precipitation rate and/or increase (decrease) in precipitation spatial coverage...	40
3.10. Vertical radar reflectivity profiles for (a) convective and (b) stratiform regimes at the maritime (green), coastal (blue), and continental (red) locations. Mean profiles for AEW passages (solid line) and no-wave (dashed line) are shown along with the difference between the AEW and no-wave regime profiles (dotted line). Secondary plots to right of each main plot shows the number of points averaged at each vertical height, note that the order of magnitude is the same throughout the bottom 11 km. ....	41
<b>PART III</b> .....	<b>55</b>
2.1. West African and Atlantic Ocean regions ( $6^{\circ} \times 6^{\circ}$ ) chosen for climatological analysis. Plots inside each regional domain indicate the relative proportion of precipitation features (using contiguous precipitation radar reflectivity) occurring in the trough ('T'), southerly ('S'), ridge ('R'), and northerly ('N') African easterly wave phases; and when no wave was identified ('O'). Fractions are calculated by using the number of features in each phase divided by the total number of features in that region.....	68
2.2. TRMM overpass 50098 on 0530 UTC 31 August 2006 showing precipitation radar reflectivity swath. Boxes are regions discussed in this study, with the swath passing through the coastal region. Arrows indicate 700 hPa wind vectors. The solid black line is the objectively-identified African easterly wave trough axis for 0600 UTC on the same day. The gray contours show the identified trough region retained after thresholding procedure. Precipitation features within the coastal domain were identified as trough-associated for this case. ....	69
3.1. Precipitation feature frequency distribution in each study region during May–October. Each month is partitioned by objectively identified AEW trough (solid black), southerly (dashed black), ridge (dotted black), and northerly (dashed gray)	

phase along with when no AEW phase (solid gray). Note the different ordinate axis scale between regions. ....	83
3.2. Cumulative frequency distributions of precipitation feature maximum storm height for each study region. Objectively identified AEW phases along with no identified AEW are displayed as in Fig. 3.1. ....	84
3.3. As in Fig. 3.2, except for stratiform fraction. ....	85
3.4. As in Fig. 3.2, except for precipitation feature area. ....	86
3.5. Mean values of (a) feature area, (b) maximum storm height (solid lines with open squares) and 30-dBZ height (dashed lines with open triangles), minimum (c) 37-GHz (dashed lines with open triangles) and 85-GHz (solid lines with open squares) PCTs, and (d) stratiform fraction during trough ('T'), southerly ('S'), ridge ('R'), and northerly ('N') AEW phase and when no AEW phase is identified ('O'). Continental northeast (red), continental northwest (orange), continental southeast (purple), continental southwest (brown), coastal (black), maritime north (green), and maritime south (blue) regions are displayed. ....	87
3.6. Mean convective vertical reflectivity profiles of TRMM precipitation radar observations for each study region. Trough (solid black), southerly (dashed black), ridge (dotted black), and northerly (dashed gray) AEW phase along with no identified AEW (solid gray) are shown. ....	88
3.7. Same as Fig. 3.6, except for stratiform component. ....	89
3.8. Mean (a) convective and (b) stratiform vertical reflectivity profiles for continental northeast (red), continental northwest (orange), continental southeast (purple), continental southwest (brown), coastal (black), maritime north (green), and maritime south (blue) regions. Line styles as in Figs. 3.6–3.7, designating AEW phase. ....	90
3.9. Same as Fig. 3.6, except for ice water content. ....	91
3.10. Same as Fig. 3.6, except for liquid water content. ....	92
3.11. Cumulative (top) and probability (bottom) frequency distributions, for each study region, of minimum 85-GHz polarization corrected temperature. Line styles as in Fig. 3.6. ....	93
3.12. As in Fig. 3.2, except for ice water path fraction, defined as ice water path divided by the sum of ice and liquid water path. Distributions are additionally separated by convective (red) and stratiform (blue) classification. ....	94
3.13. As in Fig. 3.12, except for liquid water path fraction, defined as liquid water path divided by the sum of ice and liquid water path. ....	95
<b>PART IV</b> .....	109
2.1. Map of the simulated region (solid-lined box) in West Africa. The sounding domain (dash-dot lines) used to calculate the large-scale forcing data for the	

simulations is shown, with radiosonde sites labeled. The circle indicates the 150 km radius MIT ground–radar observed domain. ....	115
4.1. Observed infrared brightness temperatures at 0600 UTC on 8 September 2006. Objectively identified African easterly wave trough axis (red solid line) and African easterly jet axis (blue dashed line) are shown along with 700 hPa wind vectors (arrows). ....	125
4.2. An example of MIT radar reflectivity (a) 2 km CAPPI at 0501 UTC on 8 September 2006. Vertical structure of the squall line mesoscale convective system is indicated by a cross–section of (b) reflectivity, and (c) HID analysis results. Distances in (a) are relative to radar location and the dashed, black A–B line represents cross–sections displayed in (b) and (c). Hydrometeors identified in (c) are melting ice (MI), hail (H), wet graupel (WG), dry graupel (DG), wet snow (WS), and dry snow (DS), rain (RN), drizzle (DZ), and unclassified (UN). ....	126
4.3. Time series of a) CAPE (solid line) and CIN (dash–dot line), b) wind magnitude and direction (toward arrow head), c) low–level vertical wind shear, and d) equivalent potential temperature anomaly for the 8 September 2006 case. Heavy vertical, dashed lines represent the time period corresponding to ground–based radar observations in Niamey, Niger. Thin, dotted lines show the times when MCS was directly over the radar. The abscissa axis format is day–UTC time. ....	127
4.4. As in Fig. 4.1, except for 0500 UTC on 14 July 2006. ....	128
4.5. As in Fig. 4.2, except for 0501 UTC on 14 July 2006. Note that some beam filling issues were present at upper levels at distances greater than 100 km. ....	129
4.6. As in Fig. 4.3, except for the 14 July 2006 case. ....	130
5.1. Time series of the (a) total (solid line), convective (dashed line), and stratiform (dotted line) volumetric rain, (b) maximum height of 0– and 30–dBZ (solid and dashed lines, respectively), and mean (c) ice and (d) liquid water path fractions for convective (solid line) and stratiform (dashed line) regions derived using MIT radar data from 8 September (black with squares) and 14 July (gray with triangles) 2006. Note that (a) and (c, d) are displayed with logarithmic ordinate axes. ....	134
5.2. (a) Mean and (b) maximum radar–derived water content during the 8 September 2006 case. Ice water content is open–contoured with intervals of 0.00001, 0.0001, 0.001, 0.005, and 0.01 in (a) and 0.01, 0.1, 0.5, 1.0, 5.0, and 10.0 in (b), while shading corresponds to liquid water content in both. Thin vertical, dotted lines show the approximate time of passage of the system over the radar. ....	135
5.3. As in Fig. 5.2, except for 14 July 2006. ....	136
6.1. Frequency of occurrence of rain rates estimated by the MIT radar (black) and produced by GCE simulations (gray) for 8 September (square) and 14 July (triangle) 2006. ....	144
6.2. Time evolution of maximum reflectivity values from (a) MIT radar observations and (b) GCE simulations for 8 September 2006. The abscissa corresponds to observed time in the radar domain in (a) and corresponding simulated time period. ....	145

6.3. CFADs of reflectivity for (a–c) MIT radar observations and (d–f) GCE simulations for the 8 September 2006 case. From top to bottom, rows correspond to all (a, d), convective (b, e), and stratiform (c, f) classified data. Shaded contour values for all plots are indicated in colorbar, with units of percentage at each vertical level. ....	146
6.4. As in Fig. 6.3, except for the 14 July 2006 case. ....	147
6.5. Occurrence frequency –height distributions of identified hydrometeor types using MIT radar reflectivity and temperature profiles for a) 8 September and b) 14 July 2006 cases. Eight hydrometeor types were identified: rain (solid black), drizzle (dotted black), dry (dash–dot black) and wet (dash–dot–dot black) snow, dry (dashed black) and wet (solid gray) graupel, hail (dashed gray), and melting ice (brightband; dash–do–dot gray). Frequencies were calculated as the number of occurrences for each HID specie at each vertical level divided by the total number for that specie over the column. ....	148
6.6. Mean observed liquid (dashed black) and ice (solid and dotted black) water contents calculated using MIT and WACR radar data; and simulated rain (dashed gray), snow (das –dot gray), graupel (solid gray), and cloud ice (dotted gray) mixing ratios during a) 8 September and b) 14 July 2006 cases. ....	149
6.7. Time evolution of hydrometeors during the 8 September (left column) and 14 July (right column) 2006 cases. Shading denotes probability frequency as a function of height for hydrometeors identified using MIT reflectivity and temperature profiles. Snow and graupel include both wet and dry identified components, while rain includes rain and drizzle hydrometeors. Overlaid are mixing ratios of corresponding hydrometeors with a contour interval of 0.01 g kg <sup>-1</sup> . ....	150
<b>PART V</b> .....	162

**PART I: INTRODUCTION TO THE DISSERTATION**

This dissertation is a combination of three complementary studies with a singular focus on the study of West African mesoscale convective systems. Each part builds upon the preceding part, forming a cohesive view of a particular outstanding problem: the need for improved understanding of West African monsoon (WAM) convection as a function of both geographic location and the major WAM synoptic feature, African easterly waves (AEWs). Detailed motivation and background are conveyed in each introductory chapter. The goals of this dissertation are two-fold: contribute to the understanding of the structure and associated environment of mesoscale convection, an important aspect of the temporal- and spatial-scale interactions during the monsoon season, and to provide comparative statistics and characteristics for use in future numerical simulations. Additionally, simulations are analyzed to gauge the performance of state-of-the-art model performance and the utility of using the aforementioned statistics to choose cases for study.

Parts II and III compare convective statistics including precipitation and vertical structure for three distinct locations, as well as differences in convective characteristics between convective systems associated with AEWs and those that are not. The primary data used in Part II were from three ground-based radars and radiosondes at a continental, coastal, and maritime location along a thermodynamic and dynamic transition region. The study contrasts statistics for each location from a 29 day period at the peak of the 2006 WAM season. Comparison of convective statistics is also presented

for mesoscale convective systems associated with AEWs and those that are not, region-by-region. Part III reports on “climatological” convective characteristics of precipitation features identified by the Tropical Rainfall Measurement Mission Precipitation Radar in seven distinct regions, at a scale smaller than previous studies in an attempt to illuminate the inherent geographical differences that are present in West African convection. Characteristics were partitioned into African easterly wave phase (trough, northerly, ridge, and southerly) and when no wave was present to examine differences associated with synoptic-scale regimes. Parts II and III were both published separately in the *Quarterly Journal of the Royal Meteorological Society* in the form presented in this dissertation.

Part IV explores the performance of the Goddard Cumulus Ensemble numerical model following recent updates in parameterization schemes that improve ice microphysics representation. This is accomplished via analysis of the representation of convective characteristics for two distinct events during the 2006 West African monsoon in the Sahel region: one associated with an AEW trough and another with no AEW influence. Results from Parts II and III were used to choose the cases. Part IV appears in the form of a manuscript submitted to *Monthly Weather Review*. Part V provides a summary of results for the entire body of work.

**PART II: RADAR CHARACTERISTICS OF CONTINENTAL, COASTAL, AND  
MARITIME CONVECTION OBSERVED DURING AMMA/NAMMA**

## CHAPTER 1

### INTRODUCTION

The West African monsoon (WAM) is characterized by the northward migration of the intertropical convergence zone (ITCZ), which reaches the furthest northward extent in August (Hastenrath 1991). The Sahel is among the northernmost regions affected by the encroaching moisture, receiving over 80% of its annual rainfall in boreal summer (Laurent et al. 1998; Mathon et al. 2002). Mesoscale convective systems (MCSs) are primary contributors of rainfall totals in West Africa (Le Barbé and Lebel 1997; D'Amato and Lebel 1998; Laurent et al. 1998; Mathon et al. 2002; Redelsperger et al. 2002; Fink et al. 2006), despite their small contribution to convective system population numbers (Mohr et al. 1999). Highly organized continental MCSs often take the form of squall lines (Hamilton et al. 1945; Eldridge 1957; Bolton 1984; Houze et al. 1989), while systems in the adjacent east Atlantic region are often more stratiform in nature (Schumacher and Houze 2003, 2006; Fuentes et al. 2008), with a transitional region for systems exiting the west African coast (Sall and Sauvageot 2005; DeLonge et al. 2010).

A key feature of the WAM are African easterly waves (AEWs), which have periods of 3–5 days (Carlson 1969a; Burpee 1972; Reed et al. 1977; Diedhiou et al.

1999), with wavelengths near 3000 km and mean speed of approximately  $8 \text{ m s}^{-1}$ . Disturbances (wave troughs) propagate westward along two tracks, one south and one north of the African easterly jet (AEJ), displaying a mixed barotropic–baroclinic growth mechanism. Hsieh and Cook (2005) showed that AEW generation may be correlated with convection within the ITCZ. More recently Thorncroft et al. (2008) suggested that upstream MCSs may provide the initial perturbation into the jet entrance required for AEW generation.

Favorable large-scale dynamical forcing for the generation of rainfall through the organization of MCSs may be provided by AEWs. For example, Fink and Reiner (2003) indicated that 40% of squall lines (SLs) in West Africa were forced by AEWs; and Taleb and Druyan (2003) reported that 30–40% of total rainfall recorded at stations in West Africa from 1953–1978 was associated with AEWs. A number of previous studies, based upon satellite and reanalysis data, have reported the effects of AEWs on the modulation of precipitation (Carlson 1969a; Burpee 1974; Duvel 1990; Diedhiou et al. 1999; Mathon et al. 2002; Fink and Reiner 2003; Gu et al. 2004; Mekonnen et al. 2006), with latitudinal phasing dependence. Debate remains as to the phasing of deep convection in West Africa with AEWs, with deep convection occurring ahead of, within, or behind the AEW trough (Payne and McGarry 1977; Diedhiou et al. 1999; Fink and Reiner 2003; Kiladis et al. 2006; Laing et al. 2008). These studies suggest synoptic-scale characteristic modulation, as opposed to mesoscale modulation (i.e. MCS characteristics) discussed in this study.

African MCS lifetimes have been reported between 2–3 hours (Chong et al. 1987) and greater than 2 days (Fink et al. 2006), though it is quite possible that extremely long

lifetimes could be a function of convective regeneration. Fortune (1980) and Peters and Tetzlaff (1988) observed that Sahelian SLs can move faster than AEWs with propagation speeds that average between 14–17 m s<sup>-1</sup> (Aspliden et al. 1976). Fink et al. (2006) found median values largely between 3–19 m s<sup>-1</sup>, dependent upon intensity metrics used. These observed MCS speeds indicate propagation into or through multiple phases of an AEW synoptic environment is possible, which suggests complex spatial scale interactions between AEWs and MCSs during the WAM season.

There have been numerous case studies involving ground-based radar data (Houze and Cheng 1977; Chong et al. 1987; Barthe et al. 2010), along with Doppler velocity analyses (Roux 1988; Roux and Ju 1990; Chong 2009) of individual African convective events. Previous studies have also examined convective characteristics for small (Buarque and Sauvageot 1997; Shinoda et al. 1999; Fink et al. 2006) and large (Geerts and Dejene 2005; Fuentes et al. 2008; Laing et al. 2008) spatial regions over West Africa. These studies focused on the timing and magnitude of precipitation along with general convective characteristics, but did not emphasize the comparison of mesoscale characteristics at different locations. The sites in this study are located in unique geographical (continental, coastal, and maritime) locations along a common latitudinal band near a transitional zone in the WAM, marked by the northward extent of monsoon moisture from the south.

The objective of this study is twofold. First, we compare MCS statistics including precipitation and vertical structure for three distinct locations in West Africa. This study benefits from the African Monsoon Multidisciplinary Analysis (AMMA; Redelsperger et al. 2006; Lebel et al. 2010) and the NASA-AMMA (NAMMA; Zipser et al. 2009)

experiments, which allowed access to a great deal of observational data in what is normally a sparsely observed area of the globe. The temporal extent of the study was determined by the common operating period (19 August – 16 September 2006, Table 1.1) of the three ground-based radars. Secondly, differences in convective characteristics between MCSs associated with AEWs and those that are not are explored for each radar location.

Table 1.1. Sampling characteristics and locations of TOGA, NPOL, and MIT radars.

	TOGA (Maritime) Praia, Cape Verde	NPOL (Coastal) Kawsara, Senegal	MIT (Continental) Niamey, Niger
3-dB beamwidth	1.66°	1.00°	1.40°
Pulse repetition frequency	1001 Hz	950 Hz	950 Hz
Repeat cycle	10 min	15 min	10 min
Wavelength	0.053 m	0.107 m	0.053 m
Range gate size	150 m	200 m	250 m
Unambiguous range	150 km	157 km	158 km
Pulse width	0.8 $\mu$ s	0.8 $\mu$ s	1.0 $\mu$ s
Latitude location	14.92°N	14.66°N	13.49°N
Longitude location	23.48°W	17.10°W	2.17°E
Period of operation, 2006	15 Aug – 16 Sep	19 Aug – 30 Sep	5 Jul – 27 Sep

## CHAPTER 2

### DATA AND METHODOLOGY

#### *2.1. Radar data and precipitation feature analysis*

Data and methodologies largely follow Cifelli et al. (2010), with additions elaborated hereafter. Radar data were the primary datasets for the analysis of convective characteristics. Fig. 2.1 shows the location of each radar site and the approximate maximum unambiguous range about each radar location. The continental (Massachusetts Institute of Technology; MIT) and maritime (Tropical Ocean and Global Atmosphere; TOGA) radar systems were both C-band, single polarimetric, while the coastal radar system (NASA Polarimetric Radar; NPOL) operated at S-band with dual polarimetric capabilities. The NPOL dual polarimetric information was not used in this study. Sampling characteristics, along with the location of each radar system are listed in Table 1.1. Quality control was performed on each dataset to remove spurious echoes. In addition to internal calibrations performed in the field, calibration comparisons of radar reflectivity against the TRMM precipitation radar (TRMM PR) were performed following methodologies described in Anagnostou et al. (2001) and Lang et al. (2009). Adjustment values are shown in Table 2.1. The attenuation correction algorithm of Patterson et al. (1979) was applied to both C-band radar systems.

Radar polar coordinate data were interpolated to a 2 km vertical and horizontal resolution Cartesian grid using the National Center for Atmospheric Research REORDER software (Mohr et al. 1986). The grid extended 130 km in the  $x$  and  $y$  directions from the radar location listed in Table 1.1. The spacing chosen was a direct result of different sampling characteristics (Table 1.1), so data interpolated to the Cartesian grid did not exceed maximum spatial resolution of any dataset at the maximum unambiguous range.

Radar reflectivity ( $Z$ ) volume scans were partitioned into convective and stratiform components using the Steiner et al. (1995) algorithm. This technique uses a convective threshold value to identify convective cores, along with a convective peakedness criterion which evaluates surrounding pixels for convective classification. Rainfall ( $R$ ) estimates were made from power-based  $Z$  (in  $\text{mm}^6 \text{m}^{-3}$ )– $R$  (in  $\text{mm h}^{-1}$ ) relationships (Table 2.1). The relations chosen were based upon radar–rain gauge comparisons for the GARP Atlantic Tropical Experiment (GATE) region (Hudlow 1979) for TOGA; and disdrometer data in Dakar (Nzeukou et al. 2004) and Niamey (Sauvageot and Lacaux 1995) for the NPOL and MIT radars, respectively. The TOGA relationship produced a higher rainfall rate for the same  $Z$  value when compared to the corresponding  $Z$ – $R$ s used for NPOL and MIT, consistent with previous  $Z$ – $R$  relationships for oceanic regimes. A single  $Z$ – $R$  relation was used for both convective and stratiform portions at each location. As with any precipitation estimator, there is inherent error associated with the use of  $Z$ – $R$  relations.

Divergence profiles were calculated using the method described by Mapes and Lin (2005), which is a refined derivative of the Browning and Wexler (1968) velocity

azimuth display (VAD) method. Briefly, polar-coordinate radar data were processed via a space-time binning algorithm (CYLBIN) to retain range-dependent characteristics. Data were pooled into 50 hPa vertical levels to account for sparse data at upper levels, while 8 km annuli were used in horizontal processing over ranges from 4–92 km. Methodology for attaining mean divergence profiles follows Hopper and Schumacher (2009), in which 40 km annuli (five-range pooling) centered about 28, 44, 60, and 76 km were used.

Ground-based radar observations in this study do not allow examination of the evolution and structural differences of the largest MCSs, due to both geographic position and limited observational domains. The spatial extent of MCSs may be several times larger than the radar scan domain and Hodges and Thorncroft (1997) showed that MCSs are preferentially generated greater than  $5^\circ$  from the most eastward radar location. Despite these limitations, ground-based observations allow detailed analysis of a smaller subset of convective systems. In order to analyze convective characteristics of radar data, precipitation features (PFs) were identified using an objective algorithm described in Cifelli et al. (2007), related to an approach developed for TRMM satellite observations (Nesbitt et al. 2000, 2006). A contiguous echo region that meets a minimum threshold reflectivity (10 dBZ) and size criterion (8 km or 4 pixels in this case) was identified in the lowest grid level (1 km AGL). The algorithm then broke these into three categories: MCS ( $\geq 1000 \text{ km}^2$ , with at least one convective grid point), sub-MCS ( $< 1000 \text{ km}^2$ , with at least one convective grid point), and no convective (NC; features that did not display required convective criteria regardless of spatial scale). Statistics of associated precipitation, reflectivity, vertical structure, and number of elements were recorded for

each feature. In addition, representative thermodynamic variables (discussed later) were retained.

While ground-based radar data provides high spatial and temporal resolution, it is important to note the limitation of the radar scan area. Due to the high frequency of large convective systems extending beyond the scan range of the radar, it is impossible to completely sample the largest convective systems within the view area of a single radar system (confirmed through infrared [IR] satellite animations; not shown). Buarque and Sauvageot (1997), using radar and rain gauge data from Niamey, suggested that rainfall estimates may scale radar estimates, dependent upon the mode of convection (i.e. SL, convective line, stratiform region) for an area calculation technique. Nesbitt et al. (2006) showed that feature area is comparable for continental and ocean systems, though the continental site did display overall larger system size in West Africa (confirmed in the present study). In this study, the continental site exhibited the largest fraction of partial features (feature that occurs at the edge of scan region and was not fully sampled; Table 2.1). Further analysis showed partial features contributed similar fractions of rain volume and feature area at all sites. Because the emphasis of this study is on understanding the relative trends in the statistics, the occurrence of partial features should not adversely affect the analysis.

## *2.2. Radiosonde data*

Radiosonde data collected near each radar location (Praia [TOGA], Kawsara/Dakar [NPOL], and Niamey [MIT]) have undergone extensive quality control and corrections (Nuret et al. 2008; Agustí-Panareda et al. 2009). Sounding launch

intervals were approximately 4 hours (0, 4, 8, 12, 16, 20 UTC) at Praia, roughly 6 hours (0, 6, 12, 18 UTC) at Niamey and Kawsara, and twice daily (0, 12 UTC) at Dakar. Missing data at Kawsara reduced the number of usable soundings. Inspection of time series and variable distributions showed that Kawsara and Dakar soundings were nearly the same, therefore given their close proximity (approximately 40 km); these two datasets were combined to improve temporal resolution. A number of thermodynamic characteristics were calculated for each sounding to characterize local environments for convective generation conditions, including convective available potential energy (CAPE), convective inhibition (CIN), and low-level shear (surface to low-level maximum zonal wind). Pseudo-adiabatic parcel ascent from mixed layer (bottom 50 hPa of sounding) was used in CAPE and CIN calculations. The methodology of Lucas et al. (2000) was used for the shear calculations. Time series correlations were tested using rank and product-moment correlations. The Wilcoxon-Mann-Whitney hypothesis test was applied at the 95% significance level for non-normal data distributions (i.e. CAPE), which is a nonparametric rank method that tests whether two samples are from the same or different populations.

### *2.3. Reanalysis data and easterly wave analysis*

The NASA Goddard Space Flight Center (GSFC) Global Modeling and Assimilation Office (GMAO) Modern Era Retrospective-analysis for Research and Applications (MERRA) product (Bosilovich et al. 2006), based upon the Goddard Earth Observing System Version 5 (GEOS-5) general circulation model (Rienecker et al. 2008), was used for identifying AEWs during the 2006 season.

Wave identification was performed using 700 hPa winds and the methodology discussed by Berry et al. (2007), in which the westward advection of curvature vorticity is employed for trough tracking. This algorithm is one of the few that explicitly attempts to reduce noise associated with the vorticity field from individual MCSs through the elimination of divergent flow. Results using the native resolution ( $0.5^\circ$  latitudinal x  $0.67^\circ$  longitudinal) resulted in a discontinuous vorticity field between time steps. By degrading the reanalysis product to a  $1^\circ$  x  $1^\circ$  grid, the algorithm produced a cleaner vorticity field in which trough tracking was easily attained. Wave identification results using MERRA were found to be comparable to those produced by the European Centre for medium-range weather forecasts interim reanalysis (not shown). An example of a typical objectively identified AEJ axis (dashed line) and AEW troughs (solid lines) are shown in Fig. 2.1.

Due to previous association of precipitation and AEW troughs, it was of interest to analyze convective characteristics while in the presence of an AEW (wave regime) and while no AEW was present (no-wave regime). To accomplish this, systems occurring within 500 km of an AEW trough identified in the MERRA dataset were assumed to be associated with the wave regime (approximately a mean AEW wavelength). Previous research has shown triggering and maintenance of convection occurs at this scale (Berry, 2009), including the top 10<sup>th</sup> percentile of intense convective events (Nicholls and Mohr 2010).

Table 2.1. Data and methodology characteristics for TOGA, NPOL, and MIT radars.

Location	Radar reflectivity adjustment via TRMM comparison (dB)	Z-R relationship	Partial features (%)
Maritime (TOGA)	-3.6	$Z = 230R^{1.25}$	34
Coastal (NPOL)	+2.0	$Z = 368R^{1.24}$	18
Continental (MIT)	+0.0	$Z = 364R^{1.36}$	52

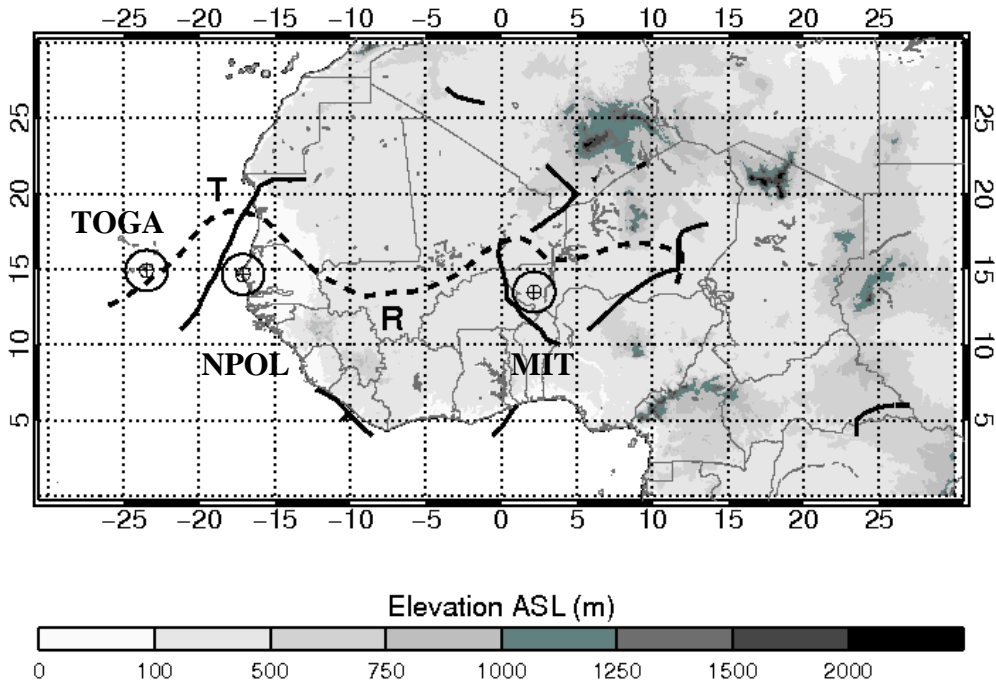


Fig. 2.1. Map of West Africa with shaded topography. The three radar systems are located at the cross-hairs, with the encircled regions showing the approximate observational scan range. Objectively identified AEJ axis (dashed line) and AEW troughs (solid lines) are shown for 8 September 2006 at 1200 UTC, with trough ('T') and ridge ('R') positions labeled.

## CHAPTER 3

### RESULTS

#### *3.1. Study area and environmental characteristics*

The 2006 July–September (JAS) season was found to have small precipitation anomalies (less than 5%) from climatological values at each location using TRMM 3B42 gridded precipitation data. A time–longitude diagram using data from 2006 averaged over 12–17°N is shown in Fig. 3.1. Data below 12°N (southern humid region in continental Africa) may skew regional analyses via the introduction of an area with less variability (Mohr et al. 2009), and was therefore excluded. The depiction of precipitation fraction data allows the cycle of convective decay and regeneration to be observed as a function of system propagation. Streaks of variable precipitation were observed, corresponding to westward propagating PFs – similar to OLR diagrams (Laing et al. 2008; Cifelli et al. 2010). Greater than 10 advecting (or propagating) modes are evident in Fig. 3.1, with varying life cycles in terms of precipitation intensities, duration, and phase speed. Objectively identified AEW trough tracks are overlaid (solid black lines). Ten AEW troughs were associated with the continental site, eight with the coastal site and 12 with the maritime site. Propagating modes averaged a speed of  $14.9 \text{ m s}^{-1}$ , while mean AEW speed was  $8.5 \text{ m s}^{-1}$ . In some cases, westward propagating precipitation

events were evident along AEW trough tracks; while other trough regimes were void of precipitation. It is possible that variations in thermodynamic conditions and topography could have driven precipitation irregularity observed in the propagating modes (Laing et al. 2008).

Focusing on the radar locations, time series of radar reflectivity–estimated precipitation, CAPE, and CIN are shown for the continental (Fig. 3.2), coastal (Fig. 3.3), and maritime (Fig. 3.4) locations, with AEW trough passages superimposed (hatched shading). Precipitation events of long duration and large spatial coverage were generally represented by unconditional rain rates (mean over entire scan domain) greater than  $0.5 \text{ mm h}^{-1}$ . Continental convective systems were linear in organization and faster moving than those found over the east Atlantic (Laing and Fritsch 1993; Hodges and Thorncroft 1997) resulting in narrower peaks inland.

Time series of maritime CAPE in Fig. 3.4b showed more variability than one might expect, likely because soundings were launched from an island large enough for nocturnal surface cooling to help establish a low–level inversion prior to daytime heating. Small values of CIN were prevalent at the coast, with greater variability at the continental and maritime sites. The largest values of CIN were observed with more frequency at the continental site. No significant correlations or anti–correlations (including lag correlation) were found between time series at each radar location. Spectral analysis of the time series showed no common precipitation or environmental periodicities between variables plotted in Figs. 3.2–3.4, suggesting little dependence upon wave–driven dynamics. However, AEW and no–wave regime environmental variable populations were shown to be significantly different (discussed later).

More frequent occurrence of MCSs ahead of AEW troughs at the continental and maritime sites (60%), and an even distribution ahead and behind the trough at the coastal location were observed, in agreement with earlier studies (Carlson 1969b; Payne and McGarry 1977; Duvel 1990; Machado et al. 1993; Diedhiou et al. 1999; Kiladis et al. 2006). During MCS events at each radar site, the AEJ was predominantly located north of the radar, which agrees with observations from Mohr and Thorncroft (2006) that found the most intense convective systems occurred south of the jet axis in September.

Interpretation of PF results was dependent upon understanding the environment within which convection occurs. Mohr and Thorncroft (2006) showed that environments of high shear and high CAPE can result in a high probability of the most intense convective systems (SLs) in West Africa, in agreement with simulations (Weisman and Klemp 1982). Vertical wind shear is an essential component to linearly organized convective systems (Bluestein and Jain 1985; Weisman et al. 1988; Coniglio et al. 2006). Nicholls and Mohr (2010) found that the top 10<sup>th</sup> percentile West African convective systems exhibited significantly stronger low-level shear. Though MCSs exist in environments with a wide range of shear, organization and system strength tend to increase with increasing shear (also true in this study despite low correlation values). Fig. 3.5 depicts the relative frequency of CAPE (top row), CIN (middle row), and low-level shear magnitudes (bottom row) at each site. The distribution of CAPE at the maritime location (Fig. 3.5a; 1090 J kg<sup>-1</sup> median value) was skewed toward lower values, while the coastal location displayed a tendency toward larger CAPE values (Fig. 3.5d; 1842 J kg<sup>-1</sup> median value). The continental site (Fig. 3.5f; 1044 J kg<sup>-1</sup> median value) was centered about more moderate CAPE values; though extremely large quantities up to

6000 J kg<sup>-1</sup> were observed (not shown), but confined to less than one percent of cases. Extreme CAPE values at the continental site were mostly unrealized, occurring in unfavorable conditions for convection (e.g. lack of synoptic-scale convergence, very little vertical shear, and large CIN). The continental domain exhibited a 50% larger CAPE value during AEW regimes (found to be significant to the 95% confidence level); while the coastal and maritime locations remained nearly unchanged between wave and no-wave regimes. Median values and distributions of CAPE are generally consistent with Fink et al. (2006) and Nicholls and Mohr (2010).

Distributions skewed toward small CIN values were observed at each location. Maritime and continental values (Figs. 3.5b,h) showed occasional large CIN, with tails extending beyond 400 J kg<sup>-1</sup>, while the relative occurrence of small CIN was most frequent at the coastal site (Fig. 3.5e). Occurrence fraction of sub-MCS features (fraction of time when sub-MCS convection was present) at the coastal site was 23%, while only 16% at the continental site indicating that smaller CIN at the coastal site may have allowed for a higher relative occurrence of sub-MCS systems. Convective storms able to overcome the larger convective cap (shown by larger CIN values) inland resulted in more “intense” convection in terms of vertical growth and reflectivity statistics (shown later) and is consistent with Nicholls and Mohr (2010) that found both larger CAPE and CIN values were present during intense events when compared to less-intense occurrences.

Similar median low-level wind shear values were observed for the maritime (easterly  $3.7 \times 10^{-3} \text{ s}^{-1}$ ), coastal (easterly  $4.1 \times 10^{-3} \text{ s}^{-1}$ ), and continental (easterly  $4.1 \times 10^{-3} \text{ s}^{-1}$ ) locations; however, distributions differ for each location. Mean vertical wind profiles

in Fig. 3.6 show the presence of the AEJ near 650 hPa, and a westerly low-level jet (LLJ) near the surface for both the continental and coastal sites. This configuration is consistent with the higher frequency of larger easterly shear values at these locations. Southwesterly flow at the surface gives way to easterly flow aloft inland. At the coast, mean southwesterlies were overlaid by northeasterlies up to the AEJ level. The largest difference between the AEW and no-wave regime wind profiles occurs at the coast, where a difference of approximately  $3 \text{ m s}^{-1}$  existed throughout the profile. In addition, the westerly LLJ was more pronounced during the no-wave regime. Calculations of shear from the surface to the westerly LLJ (not shown) revealed that the coastal site exhibited larger mixing potential at low levels during wave passage. Despite prominent changes in environmental wind profiles between AEW and no-wave regimes, the coastal location exhibited the smallest inter-regime changes in precipitation and convective characteristics in the study (shown later). Along with the relative homogeneity of CAPE mentioned earlier, this suggests that when favorable large-scale dynamics are absent, MCSs at the coastal location draw upon buoyancy to maintain their intensity, despite less environmental shear.

Mean VAD divergence profiles (Fig. 3.7) may be used to assess the effect of MCSs on the large-scale environment. Convective cells are characterized by convergence at the surface and divergence aloft, while stratiform regions display divergence at the surface, midlevel convergence and divergence aloft (Gamache and Houze 1982; Mapes and Houze 1993a). Standard deviation associated with the profiles was too large to yield significant differences between the AEW and no-wave regimes. The maritime profile (Fig. 3.7a) exhibited the same structure as the intermediary case (a

system during the conversion process from being convective to stratiform in nature) discussed in (Mapes and Houze 1993b), also for an oceanic profile. The coastal profile (Fig. 3.7b) showed divergence near the surface, mid-level convergence, and divergence aloft. The continental site exhibited the same general pattern (Fig. 3.7c), with decreased divergence at the surface and peak convergence occurring lower in the atmosphere. This suggests distinct heating profiles for each location. It should be noted that these profiles could be driven by time-of-arrival of propagating MCSs that were often in a similar stage of development (see Chapter 3.3).

### *3.2. Precipitation characteristics*

Table 3.1 lists statistics derived from PF analysis for the study time period, along with the statistics for both AEW and no-wave regimes. Less than 4% of total scans over the continent and even less over the coastal and maritime locations contained MCS events. Even though MCSs were infrequent, MCS rain volume fractions (of total observed precipitation) were large, in line with previous studies using IR (80–90%; Mathon and Laurent 2001) and TRMM microwave satellite data (60–80%; Mohr et al. 1999; Nesbitt et al. 2006) with a mean Sahelian value near 80% of annual precipitation.

A marked decrease at successive westward locations is observed in MCS area fractions (echo area coverage contributed by MCS-scale features; Table 3.1). The percentage of area covered by continental and coastal MCSs was larger than sub-MCSs, while maritime MCSs and sub-MCSs covered equivalent percentage of area, which agrees with Liu et al. (2008) that showed the population of large satellite-observed systems decreased from West Africa into the East Atlantic at this latitude.

Contrary to results from previous studies, the stratiform precipitation fraction increased from west to east. Stratiform precipitation fractions for the maritime (36%) and coastal (37%) regions generally agree with Schumacher and Houze (2006), while the continental site fraction (49%) was larger by nearly 10%. This difference may be explained by the fact that this study used only one month of data compared to five years in Schumacher and Houze (2006) and that spaceborne precipitation estimates do not account for the evaporation of precipitation in the boundary layer. Stratiform area accounts for 90% of MCS area, which may lead to underestimation from ground-based observations which view a much smaller domain than spaceborne observations and may not sample the entire MCS area. Additionally, strong easterly low-level shear in this region produced leading convective line, trailing stratiform MCSs that greatly affected boundary layer properties. Boundary layer relative humidity (not shown) increases an average of 5% (> 20% in some cases) with the passage of the convective line of these MCSs (denoted by arrow heads along the bottom abscissa in Fig. 3.2), thereby retarding evaporation of the following stratiform precipitation and increasing observed stratiform precipitation fraction. Generally, upper-level humidity increases via transport by strong convective updrafts were observed during periods of high precipitation.

To further investigate precipitation in terms of vertical structure, precipitation contributions as a function of two characteristic reflectivity levels were calculated at each vertical level. First, 20-dBZ (Figs. 3.8a-c) echo top heights were chosen to closely match the minimum threshold of the TRMM PR and minimize contamination from spurious echo missed in the radar QC process. Second, 30-dBZ (Figs. 3.8d-f) echo top heights were chosen to identify intense convective cells with significant mixed-phase

processes (DeMott and Rutledge 1998). Data for all occurrences are shown; exclusion of sub-MCSs did not affect the distributions.

A strong bimodal distribution at the maritime location (9 and 15–17 km peaks), a weak bimodal distribution at the coast (9 and 15 km peaks), and a broad, unimodal distribution (15 km peak) at the continental site were seen in the 20–dBZ distributions. The maritime and coastal distributions suggest distinct modes, while the continental site appears to be influenced by a deeper spectrum of vertical development. Convective precipitation controls the contribution from the deep mode at all sites, while the stratiform precipitation occurs at a lower height. The stratiform contribution generally exhibits a more narrow vertical distribution, with the exception of the broad stratiform distribution at the continental site.

The 30–dBZ distributions indicate that the continental and coastal locations had deeper, more intense convective modes than the maritime site. The continental and coastal distributions fall off less rapidly from the 7–9 km peak, with a secondary peak in the coastal distribution near 13 km. More vertically–developed storms display a greater propensity for mixed–phase processes (DeMott and Rutledge 1998; Nesbitt et al. 2006), enhancing the stratiform region and leading to larger precipitation contribution over the course of the study from deep convection observed over the continent (Figs. 3.8e–f). DeLonge et al. (2010) showed that MCSs transitioning from land to ocean exhibit signs of disorganization resulting in less intense convective characteristics over the ocean. Fig. 3.3 indicated that storms at the coast experienced a higher likelihood to enter a region with higher CAPE, which would theoretically produce stronger updrafts and significant lofting of precipitation–sized particles. Greater low–level shear over the land could act to

enhance linear organization, resulting in two distinct modes (ocean and land) of vertical development present during the study period.

It is well established that the diurnal cycle of precipitation in West Africa is largely controlled by propagating MCSs (McGarry and Reed 1978; Shinoda et al. 1999; Mohr 2004; Fink et al. 2006; Laing et al. 2008; Rickenbach et al. 2009) and is a function of distance from genesis and redevelopment regions (e.g. high terrain; Hodges and Thorncroft 1997; Mohr 2004). This pattern was confirmed in this study in conjunction with Meteosat imagery (not shown), showing peak precipitation occurring near 0800 LT at the continental site, 0200 LT at the coastal and maritime sites.

### *3.3. Convective characteristics and easterly waves*

Analysis of longer time period radar–estimated precipitation at the continental site showed a peak precipitation interval every 3–4 days (Nieto Ferreira et al. 2009), suggesting a correlation to AEW trough passage at this longitude. While precipitation events did occur near trough passages during the time frame of this study, many events also occurred when no wave was identified (see Table 2.1). As a result, no significant correlation between AEWs and precipitation was noted at the continental site. Given the current debate concerning the impact of AEWs on precipitation, it was of interest to compare convective system characteristics during periods of AEW passage and periods of no AEW forcing. The intent was to take advantage of radar data from the three sites to further elucidate effects of AEW forcing on convective characteristics (i.e. vertical and horizontal structure) and to understand possible feedbacks of these mesoscale features onto the larger scale (i.e. MCS latent heat release).

Table 3.2 lists contributions of AEW regime PFs during the study period, with 37–57% (32–45%) of total rain volume (feature area) associated with the AEW regime at all sites; less than previous results. Only the continental site showed greater than half of the total estimated precipitation occurred during the AEW regime. Laing et al. (2008) found that about 80% of deep convective area (as identified by satellite cold cloud streaks) was associated with AEWs for a region from 10°W–10°E. The discrepancy with the current study may be attributed to differences between the PF definition used here and the classification of convection based upon minimum IR brightness temperatures. Ground-based radar observations yield a more direct picture of the spectrum of precipitating features, while IR precipitation estimates are based upon persistent, high cloud shields associated with MCSs. Therefore the estimation and temporal evolution of precipitation may differ between these methodologies and result in partitioning differences.

To further consider differences during AEW and no-wave regimes, cumulative frequency distributions (CFDs) of feature area (Fig. 3.9a) and rain volume (Figs. 3.9b–c) were created and the distribution differences ( $CFD_{AEW} - CFD_{no-wave}$ ) analyzed. Regime populations were found to be significantly different to the 99% confidence level. The AEW regime was associated with broad increases in PF size at the continental and coastal locations, with the coastal peak increase offset to larger systems. Feature size decreased during the AEW regime at the maritime location with a maximum decrease at the sub-MCS scale. Examination of convective and stratiform precipitation volume distributions revealed that continental convective precipitation (Fig. 3.9b) was enhanced during the AEW regime, while stratiform precipitation (Fig. 3.9c) decreased. Little change was

observed at the coast for convective precipitation, with an increase in stratiform precipitation during the AEW regime. Convective precipitation decreased at the maritime site during the AEW, while stratiform precipitation showed little deviation between regimes. Inspection of PF distribution along with environmental variables may help clarify the differences shown in convective and stratiform precipitation.

The increase in system size and convective rain volume at the continental site (Fig. 3.9a) is consistent with increased CAPE, decreased CIN, and stronger shear resulting in a shift of sub-MCSs to MCS-scale that occurred during the AEW regime compared to the no-wave regime. Increased large system population at the coast may have been driven by increased CIN and vertical shear which resulted in a greater thermodynamic triggering barrier and provided increased organization for larger systems at the expense of smaller systems. A reduction in CIN and weaker vertical shear in the lowest 3 km were observed during the wave regime at the maritime site, explaining the formation of weaker, smaller convection.

Differences in convective and stratiform contributions can be further elucidated in terms of mean vertical reflectivity profiles (Fig. 3.10). Convective (stratiform) profiles for each site are similar, with near surface mean values between 36–40 (22–28) dBZ. The decrease in reflectivity with height is similar for all three locations. Continental and maritime AEW regime convective profiles were more intense and exhibited higher reflectivity values aloft compared to the no-wave regime, suggesting hydrometeor loading aloft due to strong updrafts. Note that the number of points used to construct the profiles was an order of magnitude less for the continental no-wave regime, also suggesting less vertical growth overall. The coastal site exhibited very little difference in

convective reflectivity profiles for AEW and no-wave regimes, which agrees with convective precipitation differences noted earlier (Fig. 3.9b). Land-to-ocean transitioning MCSs (coastal site) have been shown to diminish in strength (e.g. DeLonge et al. 2010) due to less favorable thermodynamic (e.g. lower specific humidity) and dynamic (e.g. reduced vertical wind shear) conditions. The changes associated with this transition may have mitigated enhanced synoptic scale moisture flux convergence and potential vorticity during the AEW regime to mediate vertical reflectivity profiles.

A brightband signature, owing to the melting of aggregates common in organized MCSs (Houze et al. 1989), was observed near 3–5 km in the stratiform profile at the coastal and continental sites. Decreasing reflectivity below this level toward the surface is a signature of droplet evaporation below cloud base, consistent with mesoscale descent. The continental AEW regime stratiform profile decreased more rapidly with height when compared to the no-wave regime, consistent with the reduction in stratiform rain area (Fig. 3.9c) noted earlier. The order of magnitude difference in the continental number of points profile might suggest the importance of large-scale dynamics during the AEW regime on MCSs for the maintenance of the stratiform shield at this site. The consequences of these profiles are that MCS heating profiles at the coastal and maritime locations are comparable for the wave and no-wave regimes, whereas at the continental site, differences arise due to the modification of stratiform structure. Weaker upper-level stratiform signal during the AEW regime results in a reduction of heating aloft and a less top-heavy heating profile (Mapes and Houze 1995).

Table 3.1. Convective system characteristics derived from precipitation feature analysis for all study times and within AEW and no-wave regimes.

Location	Regime	MCS occurrence fraction (%)	MCS rain volume fraction (%)	MCS area fraction (%)	Convective (Stratiform) rain volume fraction (%)	Convective (Stratiform) area fraction (%)	Number of precipitation features identified
Maritime (TOGA)	All	0.6	83	53	64 (36)	9 (91)	14 661
	AEW	0.3	81	57	61 (39)	9 (91)	6 622
	No wave	0.4	73	47	66 (34)	9 (91)	8 039
Coastal (NPOL)	All	1.4	85	72	63 (37)	17 (83)	9 507
	AEW	0.6	89	81	56 (44)	16 (84)	3 031
	No wave	0.9	81	65	68 (32)	18 (82)	6 476
Continental (MIT)	All	3.6	92	83	51 (49)	12 (88)	6 468
	AEW	2.0	95	88	53 (47)	12 (88)	2 620
	No wave	1.9	88	79	49 (51)	12 (88)	3 848

Table 3.2. Contribution of AEW regime precipitation features as a function of study period totals.

Location	Total feature fraction (%)	Total rain volume fraction (%)	Convective rain volume fraction (%)	Stratiform rain volume fraction (%)
Maritime	45	37	35	41
Coastal	37	45	41	53
Continental	41	57	59	55

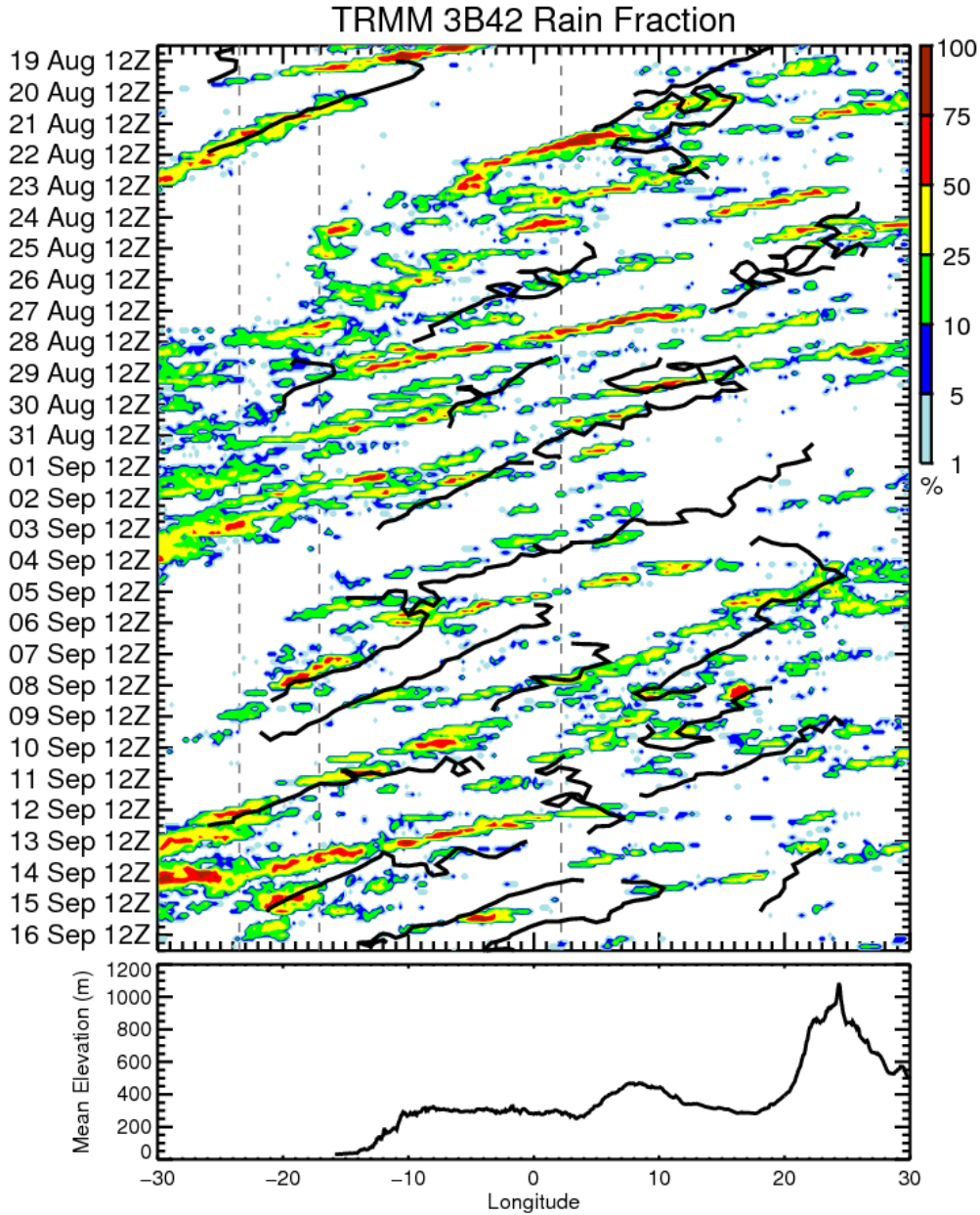


Fig. 3.1. Time–longitude plot of TRMM 3B42 gridded rainfall product averaged between 12–17°N. Contours represent percentage of rainfall above threshold value (0.8 mm h<sup>-1</sup>, mean value during 2006 season), with greater values representing increased areas of rain rates in observed systems – a proxy for size of precipitating system. Exclusion of data below 12°N was used to reduce “noise” present from the southern track of precipitation associated with the summer monsoon. Objectively identified AEW trough tracks are overlaid (black lines), with all tracks that persist for less than 1.5 days and 8 degrees in longitudinal length filtered out. Vertical, dashed lines show the location of each radar system in the study. The bottom plot denotes mean elevation between 12–17°N.

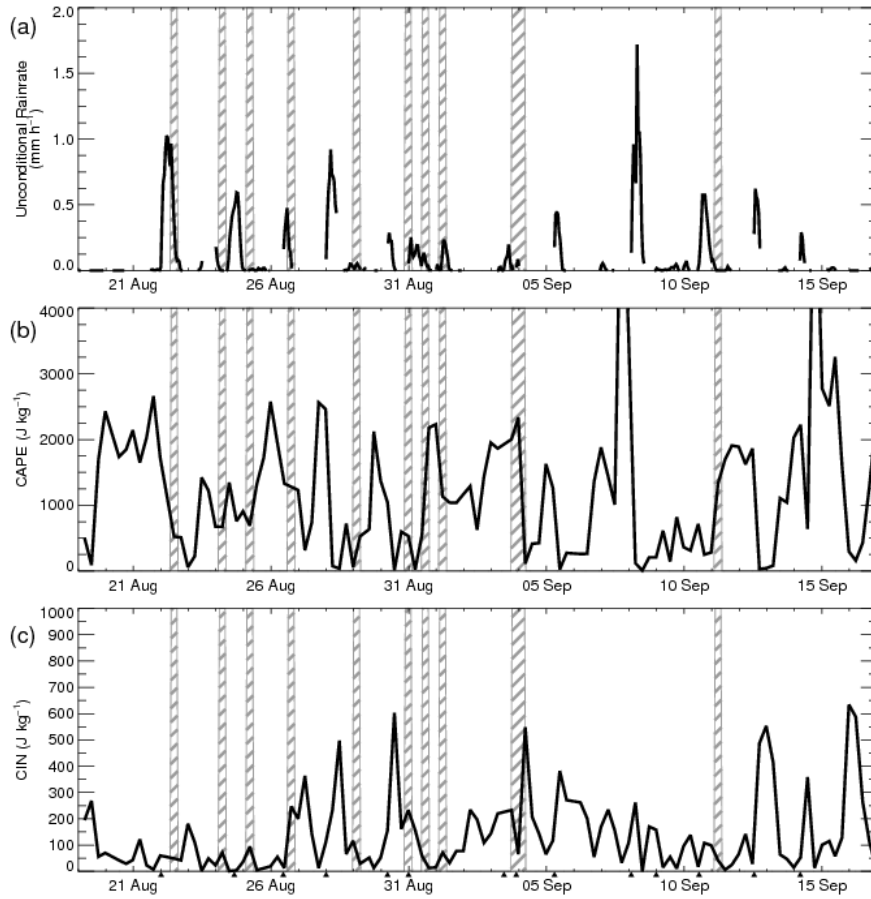


Fig. 3.2. Time series of (a) radar-estimated unconditional rainfall rate, (b) CAPE, and c CIN for the continental location, 19 August – 16 September 2006. Hatched, vertical bars indicate the presence of AEW troughs within 500 km of the site. Arrow heads along the CIN plot abscissa indicate the first radar echo occurrence of mesoscale convective systems of large spatial ( $> 1000 \text{ km}^2$ ) and temporal ( $> 3 \text{ h}$ ) extent.

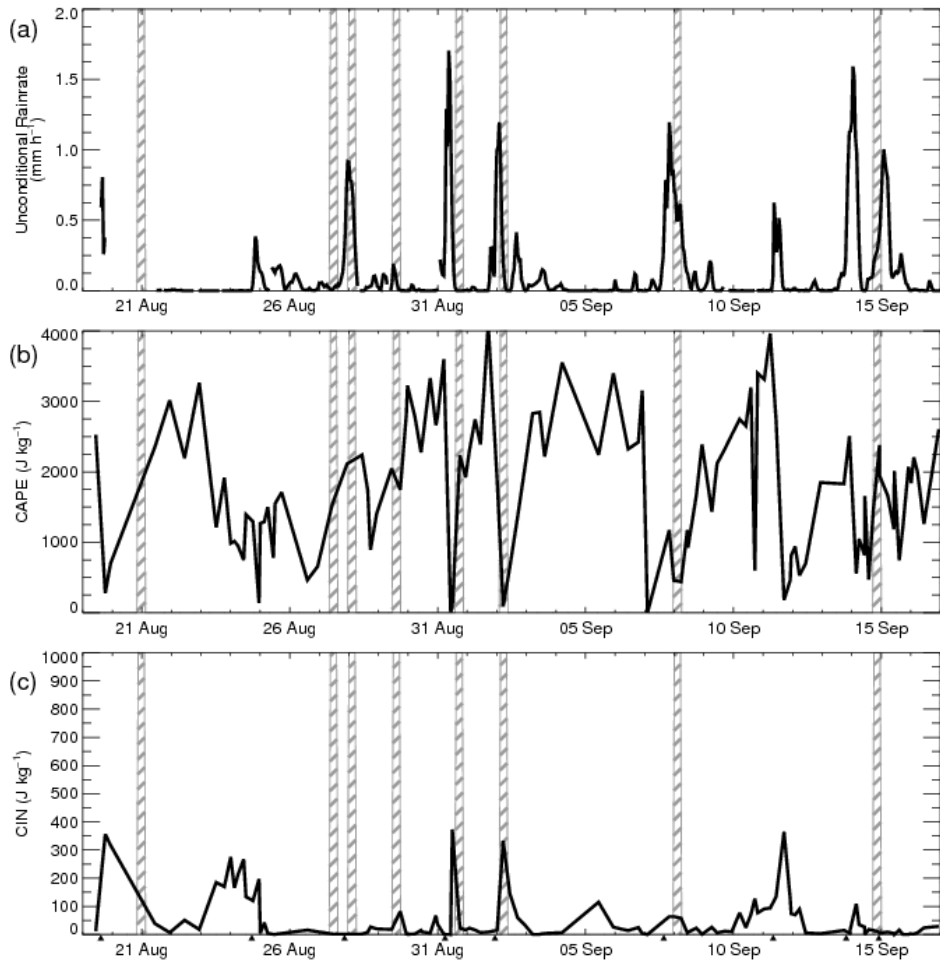


Fig. 3.3. As in Fig. 3.2, but for the coastal location.

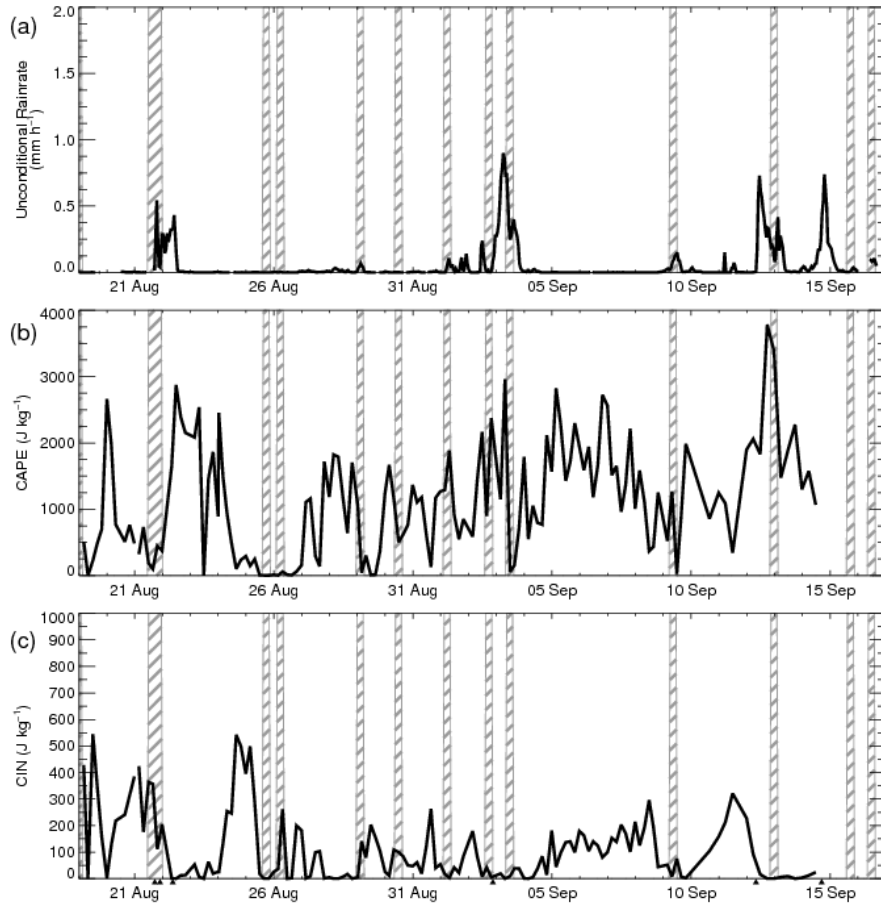


Fig. 3.4. As in Fig. 3.2, but for the maritime location.

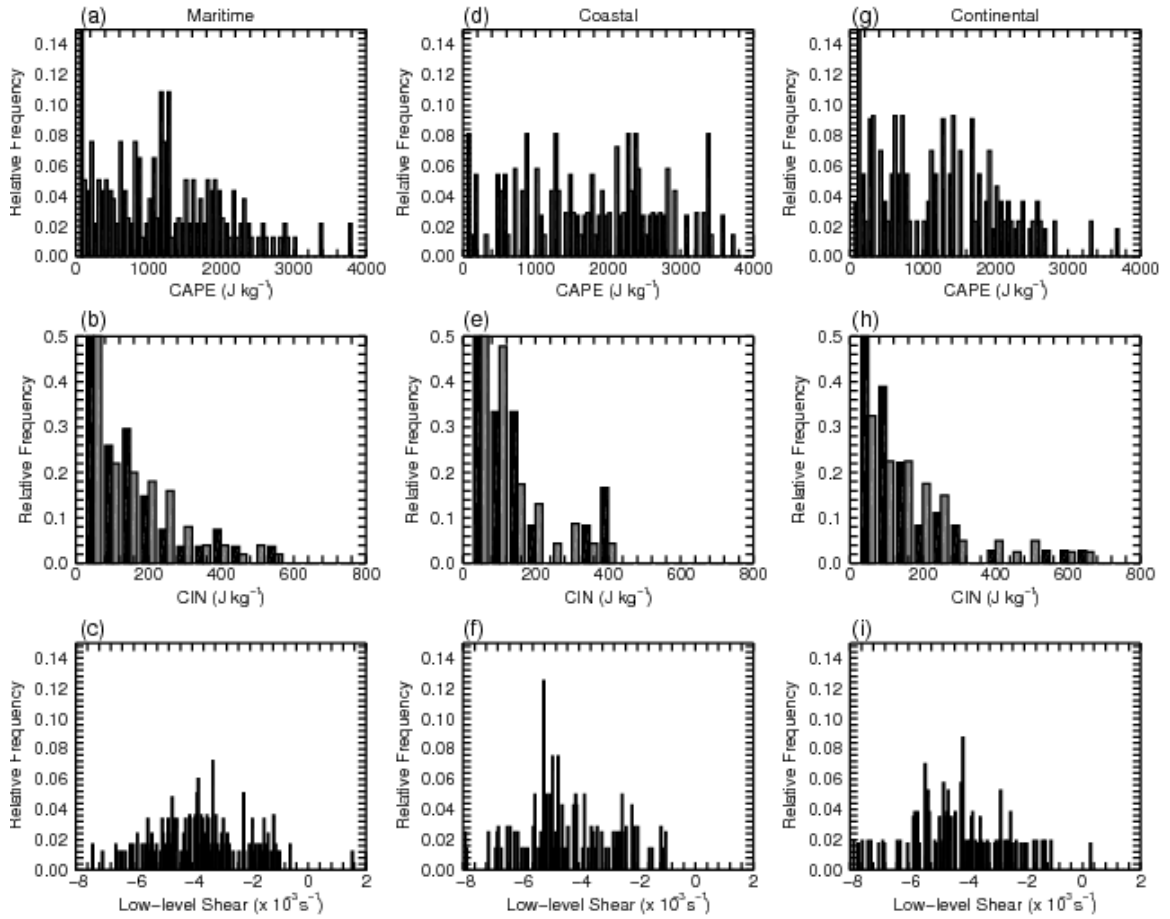


Fig. 3.5. Frequency distribution of calculated environmental variables for the maritime (a–c), coastal (d–f), and continental (g–i) locations. CAPE (top row), CIN (middle row), and low-level shear (bottom row) are shown. Black bars represent values calculated during an AEW regime, while gray bars denote no-wave regime calculations.

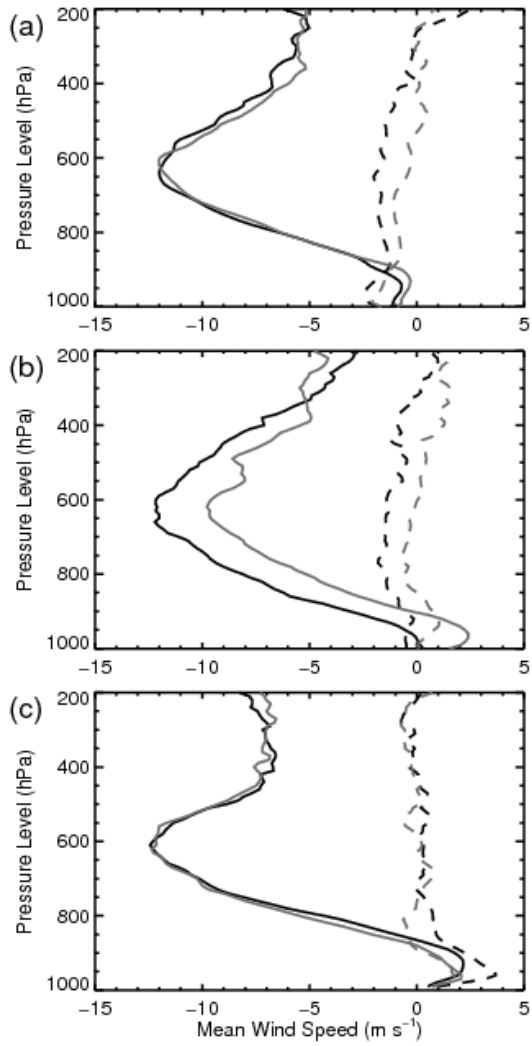


Fig. 3.6. Mean zonal (solid lines) and meridional (dashed lines) vertical wind profiles for the (a) maritime, (b) coastal, and (c) continental locations. Mean rawinsonde profiles are shown for the African easterly wave (black) and no-wave (gray) regimes.

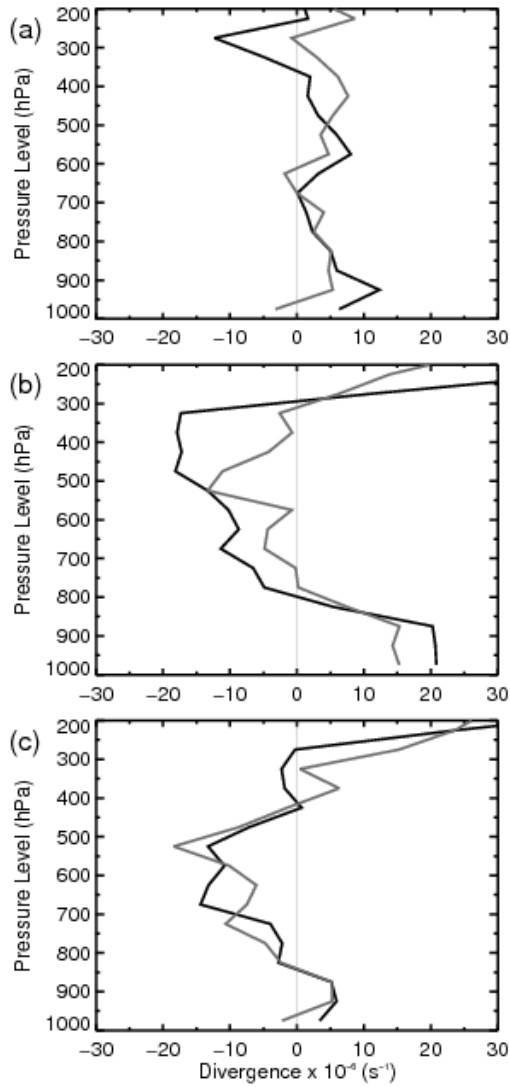


Fig. 3.7. Mean velocity azimuth display divergence profiles for the (a) maritime, (b) coastal, and (c) continental locations. Profiles of 40 km annuli centered about ranges of 24, 44, 60, and 76 km from the radar are averaged for AEW (black) and no-wave (gray) regimes. Profiles are made up of both convective and stratiform components.

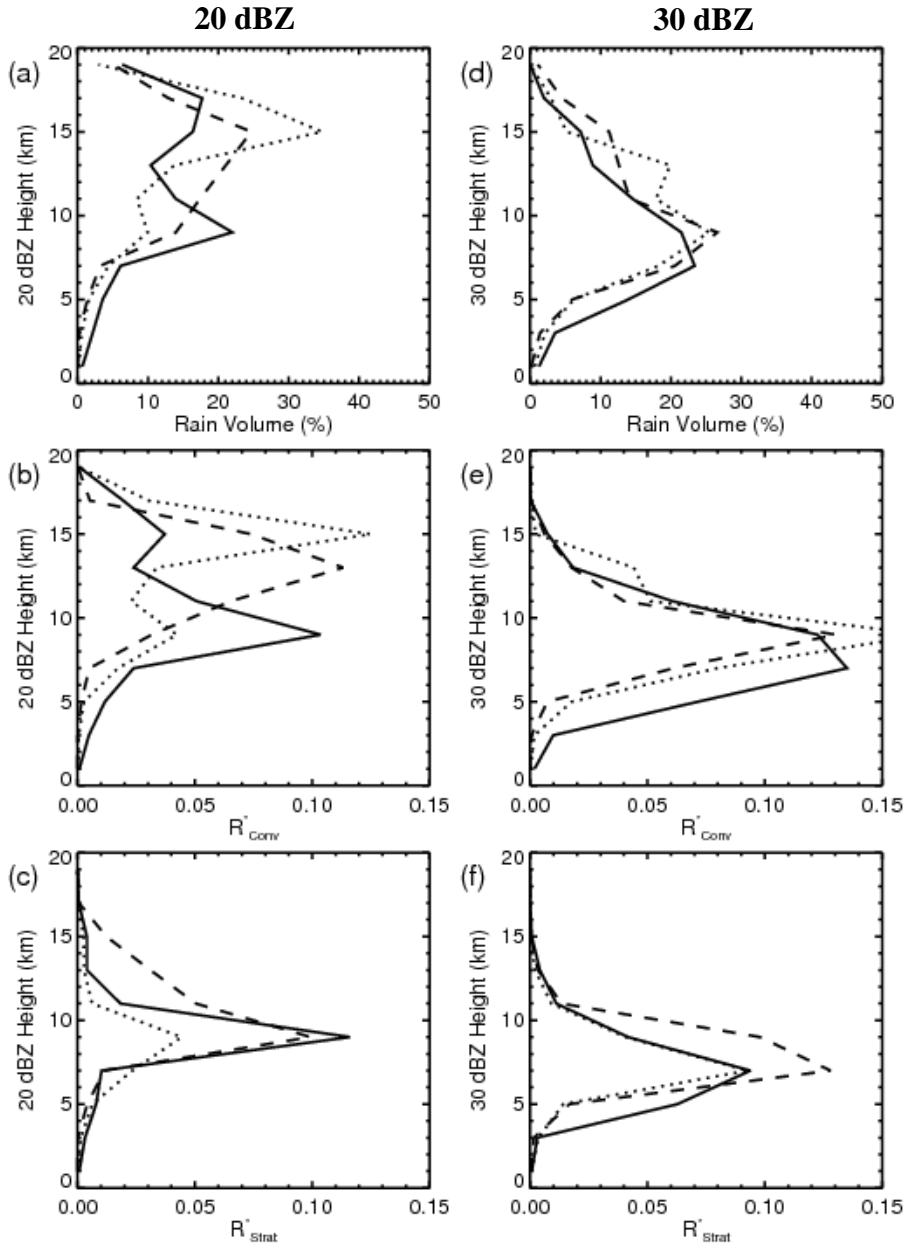


Fig. 3.8. Contribution by precipitation features, at the maritime (solid line), coastal (dotted line) and continental (dashed line), to (a,d) total volumetric rainfall as a function of mean (a–c) 20 dBZ and (d–f) 30 dBZ echo–top heights. Convective (b,e) rain volume–weighted reflectivity occurrence distributions normalized by maximum occurrence were used to illuminate the convective mode of precipitation. The same methodology was used for stratiform (c,f) contributions.

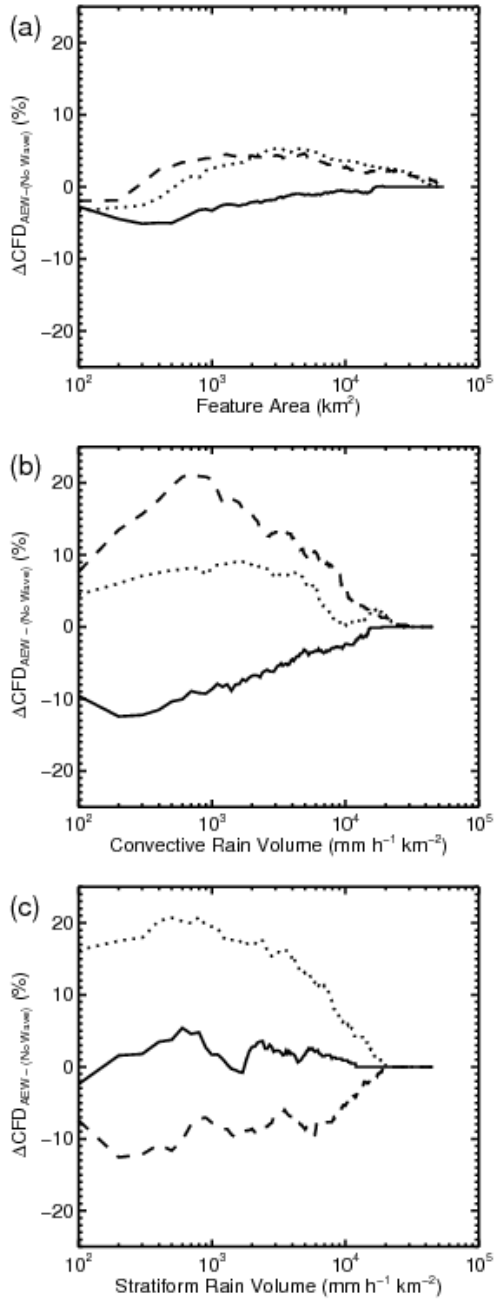


Fig. 3.9. Difference in cumulative frequency distributions between AEW and no-wave regimes for a) precipitation feature area, b) convective and c) stratiform volumetric rainfall. Maritime (solid line), coastal (dotted line), and continental (dashed line) locations are shown. Positive values correspond to an increase during the AEW regime. Less (more) volumetric rainfall may be interpreted as a decrease (increase) in precipitation rate and/or increase (decrease) in precipitation spatial coverage.

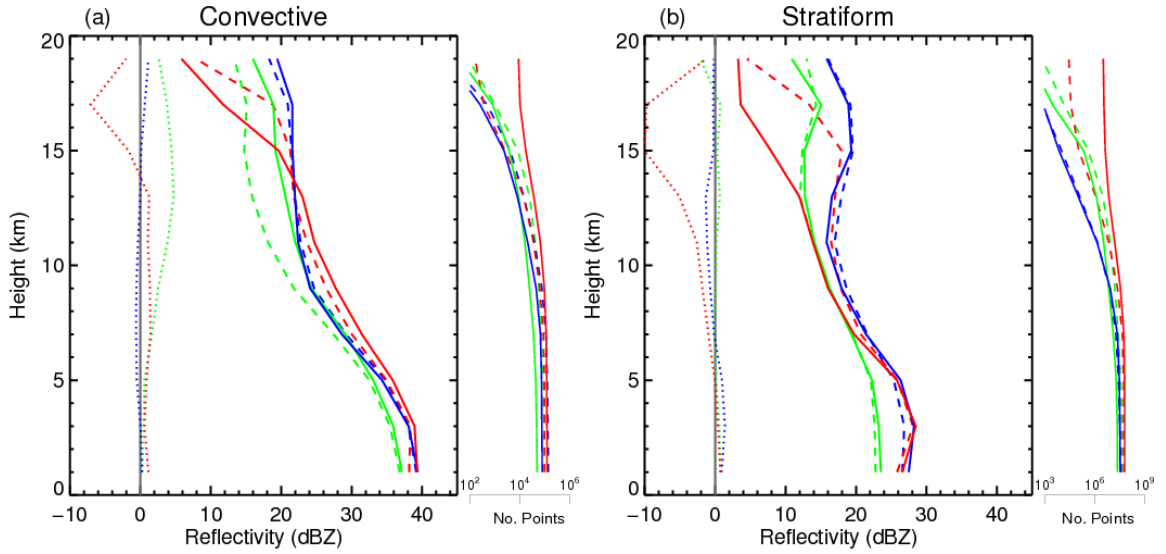


Fig. 3.10. Vertical radar reflectivity profiles for (a) convective and (b) stratiform regimes at the maritime (green), coastal (blue), and continental (red) locations. Mean profiles for AEW passages (solid line) and no-wave (dashed line) are shown along with the difference between the AEW and no-wave regime profiles (dotted line). Secondary plots to right of each main plot shows the number of points averaged at each vertical height, note that the order of magnitude is the same throughout the bottom 11 km.

## CHAPTER 4

### CONCLUSIONS

A comparison of convective characteristics via ground-based radar statistics for three unique geographic locations (continental, coastal, and maritime) was presented for the peak of the 2006 WAM season. High spatial and temporal resolution ground-based radar observations were complimented by sounding locations near each radar system, allowing characterization of convective events and the thermodynamic environment in which they occurred. A precipitation feature algorithm was employed to analyze precipitation and area characteristics at each site. Partitioning data in terms of convective and stratiform precipitation modes and AEW (or no-wave) presence was used to analyze geographic and regime variability of convective system structure and characteristics.

The diurnal cycle of precipitation at each location was largely dependent upon the time-of-arrival of propagating MCSs. The distribution of environmental conditions was important in determining differences in convective characteristics at each site. Key environmental and dynamical characteristics of each location are listed in Table 4.1. All locations were generally favorable for the formation and/or maintenance of deep convection, though the extent of organization, and therefore characteristics, depended upon the environment associated with each location. For example, the continental and coastal sites supported more

organized, linear convection, while the maritime site exhibited less organized convective systems (important in terms of vertical growth and heating profiles of MCSs).

Phasing of MCSs with AEW troughs differed on a regional basis and precipitation was uncorrelated to trough passage during this period. The mean speed of MCS systems was greater than AEWs, suggesting a somewhat complex interaction between mesoscale and synoptic disturbances. Table 4.2 notes the tendency of observed environmental and convective characteristics for each location during the AEW regime in comparison to the no-wave regime. The continental AEW regime displayed the greatest total precipitation, with near equal contributions from stratiform and convective components and an increase in precipitation during the AEW regime. In addition, less total precipitation was observed at the coastal and maritime locations during the AEW regime compared to the no-wave regime. Increased occurrence of large MCSs at the coast resulted in increased stratiform fraction and therefore increased stratiform precipitation. Together the results suggest important differences exist longitudinally across West Africa and to some degree whether convective systems interact with an AEW. Regional differences were generally more striking than those found between AEW and no-wave regimes at each site and were largely driven by differences in environmental characteristics.

Results presented here are limited by the short analysis period. Future work should examine climatological PFs via satellite observations, where a large number of convective systems can be sampled to better characterize differences between features associated with AEW and no-wave regimes. Timing of convection in terms of AEW passage would also be of interest to investigate systematic changes of environment by preceding convection for large systems leading to favorable feedback mechanisms with

the synoptic scale (and possible cyclogenesis precursor). In addition, comparisons to inferred microphysics of different synoptic regimes and convective and stratiform components within MCSs should be compared against model simulations. Detailed study of MCS kinematics at each region would help quantify structural variability associated with geographic location and AEW and no-wave phasing, leading to a better understanding of latent heating and momentum transfer in comparison to model simulations.

Table 4.1. Comparison of key characteristics for each location during 19 August – 16 September 2006.

	Maritime	Coastal	Continental
CAPE	Moderate	High	Moderate
CIN	Low-to-moderate	Low	Moderate
low-level Shear	Weak-to-moderate	Moderate	Moderate-to-high
Wind profile	No LLJ	Weak LLJ	Moderate LLJ
MCS location	Ahead of AEW trough	Equal ahead and behind of AEW trough	Ahead of AEW trough
AEJ location	N of radar	N of radar	N of radar

Table 4.2. AEW regime characteristics in relation to no-wave regime characteristics during 19 August – 16 September 2006.

		Maritime	Coastal	Continental
		No preference	00 UTC	06 UTC
	<b>AEW arrival</b>			
	<b>Rain volume</b>	-3%	+3%	+4%
Environmental	<b>CAPE</b>	0%	-22%	+50%
	<b>CIN</b>	-55%	+68%	-44%
	<b>low-level Shear</b>	+1%	+31%	-3%
Precipitation Features	<b>Area</b>	0%	+2%	+2%
	<b>Convective rain</b>	-2%	+3%	+6%
	<b>Stratiform rain</b>	+1%	+6%	-4%
	<b>Stratiform fraction</b>	+5%	+12%	-4%

## REFERENCES

- Agustí-Panareda, A., D. Vasiljevic, A. Beljaars, O. Bock, F. Guichard, M. Nuret, A. Garcia Mendez, E. Andersson, P. Bechtold, A. Fink, H. Hersbach, J. Lafore, J. Ngamini, D. J. Parker, J. Redelsperger, and A. M. Tompkins, 2009: Radiosonde humidity bias correction over the West African region for the special AMMA reanalysis at ECMWF. *Quart. J. Roy. Meteor. Soc.*, **135**, 595-617.
- Anagnostou, E. N., C. A. Morales, and T. Dinku, 2001: The use of TRMM precipitation radar observations in determining ground radar calibration biases. *J. Atmos. Oceanic Technol.*, **18**, 616-628.
- Aspliden, C., Y. Tourre and J. Sabine, 1976: Some climatological aspects of West African disturbance lines during GATE. *Mon. Wea. Rev.*, **104**, 1029-1035
- Barthe, C., N. Asencio, J. Lafore, M. Chong, B. Campistron, and F. Cazenave, 2010: Multi-scale analysis of the 25-27 July 2006 convective period over Niamey: Comparison between Doppler radar observations and simulations. *Quart. J. Roy. Meteor. Soc.*, **136**(S1), 190-208.
- Berry, G., C. Thorncroft, and T. Hewson, 2007: African easterly waves during 2004—Analysis using objective techniques. *Mon. Wea. Rev.*, **135**, 1251-1267.
- Berry, G., 2009: *African Easterly Waves and Convection*, Ph.D. Dissertation, 209 pp. Department of Atmospheric and Environmental Sciences, University at Albany, SUNY: Albany, New York: Albany, New York.
- Bluestein, H. B., and M. H. Jain, 1985: Formation of mesoscale lines of precipitation: Severe squall lines in Oklahoma during the Spring. *J. Atmos. Sci.*, **42**, 1711-1732.
- Bolton, D., 1984: Generation and propagation of African squall lines. *Quart. J. Roy. Meteor. Soc.*, **110**, 695-721.
- Bosilovich, M. G., S. D. Schubert, M. Rienecker, R. Todling, M. Suarez, J. Bacmeister, R. Gelaro, G. Kim, I. Stajner, and J. Chen, 2006: NASA's Modern Era Retrospective-Analysis for Research and Applications (MERRA). *U.S. CLIVAR Variations*, **4**(2), 5-8.

- Browning, K. A., and R. Wexler, 1968: The determination of kinematic properties of a wind field using Doppler radar. *J. Appl. Meteor.*, **7**, 105–113.
- Buarque, S. R., and H. Sauvageot, 1997: The estimation of rainfall in the Sahelian squall line by the area-threshold method. *Atmos. Res.*, **43**, 207-216.
- Burpee, R. W., 1972: The origin and structure of easterly waves in the lower troposphere of North Africa. *J. Atmos. Sci.*, **29**, 77-90.
- Burpee, R. W., 1974: Characteristics of North African easterly waves during the summers of 1968 and 1969. *J. Atmos. Sci.*, **31**, 1556-1570.
- Carlson, T. N., 1969a: Some remarks on African disturbances and their progress over the tropical Atlantic. *Mon. Wea. Rev.*, **97**, 716-726.
- Carlson, T. N., 1969b: Synoptic histories of three African disturbances that developed into Atlantic hurricanes. *Mon. Wea. Rev.*, **97**, 256-276.
- Chong, M., P. Amayenc, G. Scialom, and J. Testud, 1987: A tropical squall line observed during the COPT 81 experiment in West Africa. Part 1: Kinematic structure inferred from dual-Doppler radar data. *Mon. Wea. Rev.*, **115**, 670-694.
- Chong, M., 2009: The 11 August 2006 squall-line system as observed from MIT Doppler radar during the AMMA SOP. *Quart. J. Roy. Meteor. Soc.*, **136**(S1), 209-226.
- Cifelli, R., S. W. Nesbitt, S. A. Rutledge, W. A. Petersen, and S. Yuter, 2007: Radar Characteristics of precipitation features in the EPIC and TEPPS regions of the East Pacific. *Mon. Wea. Rev.*, **135**, 1576-1595.
- Cifelli, R., T. Lang, S. A. Rutledge, N. Guy, E. J. Zipser, J. Zawislak, and R. Holzworth, 2010: Characteristics of an African easterly wave observed during NAMMA. *J. Atmos. Sci.*, **67**, 3-25.
- Coniglio, M. C., D. J. Stensrud, and L. J. Wicker, 2006: Effects of upper-level shear on the structure and maintenance of strong quasi-linear mesoscale convective systems. *J. Atmos. Sci.*, **63**, 1231-1252.
- D'Amato, N., and T. Lebel, 1998: On the characteristics of the rainfall events in the Sahel with a view to the analysis of climatic variability. *Int. J. Climatol.*, **18**, 955-974.
- DeLonge, M. S., J. D. Fuentes, S. Chan, P. A. Kucera, E. Joseph, A. T. Gaye, and B. Daouda, 2010: Attributes of mesoscale convective systems at the land-ocean transition in Senegal during NASA African Monsoon Multidisciplinary Analyses 2006. *J. Geophys. Res.*, **115**, 16 PP.

- DeMott, C. A., and S. A. Rutledge, 1998: The vertical structure of TOGA COARE convection. Part I: Radar echo distributions. *J. Atmos. Sci.*, **55**, 2730-2747.
- Diedhiou, A., S. Janicot, A. Viltard, P. de Felice, and H. Laurent, 1999: Easterly wave regimes and associated convection over West Africa and tropical Atlantic: results from the NCEP/NCAR and ECMWF reanalyses. *Climate Dyn.*, **15**, 795-822.
- Duvel, J. P., 1990: Convection over tropical Africa and the Atlantic Ocean during northern summer. Part II: Modulation by Easterly Waves. *Mon. Wea. Rev.*, **118**, 1855-1868.
- Eldridge, R. H., 1957: A synoptic study of West African disturbance lines. *Quart. J. Roy. Meteor. Soc.*, **84**, 468-469.
- Fink, A. H., and A. Reiner, 2003: Spatiotemporal variability of the relation between African easterly waves and West African squall lines in 1998 and 1999. *J. Geophys. Res.*, **108**, 17 PP.
- Fink, A. H., D. G. Vincent, and V. Ermert, 2006: Rainfall types in the West African Sudanian Zone during the Summer Monsoon 2002. *Mon. Wea. Rev.*, **134**, 2143-2164.
- Fortune, M., 1980: Properties of African squall lines inferred from time-lapse satellite imagery. *Mon. Wea. Rev.*, **108**, 153-168.
- Fuentes, J. D., B. Geerts, T. Dejene, P. D'Odorico, and E. Joseph, 2008: Vertical attributes of precipitation systems in West Africa and adjacent Atlantic Ocean. *Theor. Appl. Climatol.*, **92**, 181-193.
- Gamache, J. F., and R. A. Houze, Jr., 1982: Mesoscale air motions associated with a tropical squall line. *Mon. Wea. Rev.*, **110**, 118-135.
- Geerts, B., and T. Dejene, 2005: Regional and diurnal variability of the vertical structure of precipitation systems in Africa based on spaceborne radar data. *J. Climate*, **18**, 893-916.
- Gu, G., R. F. Adler, G. J. Huffman, and S. Curtis, 2004: African easterly waves and their association with precipitation. *J. Geophys. Res.*, **109**, 12 PP.
- Hamilton, R. A., J. W. Archbold, and C. K. M. Douglas, 1945: Meteorology of Nigeria and adjacent territory. *Quart. J. Roy. Meteor. Soc.*, **71**, 231-264.
- Hastenrath, S., 1991: *Climate Dynamics of the Tropics*. Kluwer Academic Publishers: Norwell, Mass.; pp 488

- Hodges, K. I., and C. D. Thorncroft, 1997: Distribution and statistics of African mesoscale convective weather systems based on the ISCCP Meteosat imagery. *Mon. Wea. Rev.*, **125**, 2821-2837.
- Hopper, L. J., and C. Schumacher, 2009: Baroclinicity influences on storm divergence and stratiform rain: subtropical upper-level disturbances. *Mon. Wea. Rev.*, **137**, 1338-1357.
- Houze, R. A., and C. Cheng, 1977: Radar characteristics of tropical convection observed during GATE: Mean properties and trends over the summer season. *Mon. Wea. Rev.*, **105**, 964-980.
- Houze, R. A., M. I. Biggerstaff, S. A. Rutledge, and B. F. Smull, 1989: Interpretation of Doppler weather radar displays of midlatitude mesoscale convective systems. *Bull. Amer. Meteor. Soc.*, **70**, 608-619.
- Hsieh, J., and K. H. Cook, 2005: A study of the energetics of African easterly waves using a regional climate model. *Mon. Wea. Rev.*, **133**, 1311-1327.
- Hudlow, M. D., 1979: Mean rainfall patterns for the three phases of GATE. *J. Appl. Meteor.*, **18**, 1656-1669.
- Kiladis, G. N., C. D. Thorncroft, and N. M. J. Hall, 2006: Three-dimensional structure and dynamics of African easterly waves. Part I: Observations. *J. Atmos. Sci.*, **63**, 2212-2230.
- Laing, A. G., and J. M. Fritsch, 1993: Mesoscale convective complexes in Africa. *Mon. Wea. Rev.*, **121**, 2254-2263.
- Laing, A. G., R. Carbone, V. Levizzani, and J. Tuttle, 2008: The propagation and diurnal cycles of deep convection in northern tropical Africa. *Quart. J. Roy. Meteor. Soc.*, **134**, 93-109.
- Lang, T. J., S. W. Nesbitt, and L. D. Carey, 2009: On the correction of partial beam blockage in polarimetric radar data. *J. Atmos. Oceanic Technol.*, **26**, 943-957.
- Laurent, H., N. D'Amato, and T. Lebel, 1998: How important is the contribution of the mesoscale convective complexes to the Sahelian rainfall? *Phys. Chem. Earth*, **23**, 629-633.
- Le Barbé, L., and T. Lebel, 1997: Rainfall climatology of the HAPEX-Sahel region during the years 1950-1990. *J. Hydrol.*, **188**, 43-73.
- Lebel, T., D. J. Parker, C. Flamant, B. Bourlès, B. Marticorena, E. Mougin, C. Peugeot, A. Diedhiou, J. M. Haywood, J. B. Ngamini, J. Polcher, J. Redelsperger, and C. D. Thorncroft, 2010: The AMMA field campaigns: multiscale and

- multidisciplinary observations in the West African region. *Quart. J. Roy. Meteor. Soc.*, **136**(S1), 8-33.
- Liu, C., E. J. Zipser, D. J. Cecil, S. W. Nesbitt, and S. Sherwood, 2008: A cloud and precipitation feature database from nine years of TRMM observations. *J. Appl. Meteor. Climatol.*, **47**, 2712-2728.
- Lucas, C., E. J. Zipser, and B. S. Ferrier, 2000: Sensitivity of tropical West Pacific oceanic squall lines to tropospheric wind moisture profiles. *J. Atmos. Sci.*, **57**, 2351-2373.
- Machado, L. A. T., J. Duvel, and M. Desbois, 1993: Diurnal variations and modulation by easterly waves of the size distribution of convective cloud clusters over West Africa and the Atlantic Ocean. *Mon. Wea. Rev.*, **121**, 37-49.
- Mapes, B. E., and R. A. Houze, 1993a: Cloud clusters and superclusters over the oceanic warm pool. *Mon. Wea. Rev.*, **121**, 1398-1416.
- Mapes, B., and R. A. Houze, 1993b: An integrated view of the 1987 Australian monsoon and its mesoscale convective systems. II: Vertical structure. *Q.J. Royal Met. Soc.*, **119**, 733-754.
- Mapes, B. E., and R. A. Houze, 1995: Diabatic divergence profiles in Western Pacific mesoscale convective systems. *J. Atmos. Sci.*, **52**, 1807-1828.
- Mapes, B. E., and J. Lin, 2005: Doppler radar observations of mesoscale wind divergence in regions of tropical convection. *Mon. Wea. Rev.*, **133**, 1808-1824.
- Mathon, V., and H. Laurent, 2001: Life cycle of Sahelian mesoscale convective cloud systems. *Quart. J. Roy. Meteor. Soc.*, **127**, 377-406.
- Mathon, V., H. Laurent, and T. Lebel, 2002: Mesoscale convective system rainfall in the Sahel. *J. Appl. Meteor. Climatol.*, **41**, 1081-1092.
- McGarry, M. M., and R. J. Reed, 1978: Diurnal variations in convective activity and precipitation during phases II and III of GATE. *Mon. Wea. Rev.*, **106**, 101-113.
- Mekonnen, A., C. D. Thorncroft, and A. R. Aiyyer, 2006: Analysis of convection and its association with African easterly waves. *J. Climate*, **19**, 5405-5421.
- Mohr, C. G., L. J. Miller, R. L. Vaughan, and H. W. Frank, 1986: The merger of mesoscale datasets into a common Cartesian format for efficient and systematic analyses. *J. Atmos. Oceanic Technol.*, **3**, 143-161.

- Mohr, K. I., J. S. Famiglietti, and E. J. Zipser, 1999: The contribution to tropical rainfall with respect to convective system type, size, and intensity estimated from the 85-GHz ice-scattering signature. *J. Appl. Meteor.*, **38**, 596-606.
- Mohr, K. I., 2004: Interannual, monthly, and regional variability in the wet season diurnal cycle of precipitation in sub-Saharan Africa. *J. Climate*, **17**, 2441-2453.
- Mohr, K. I., and C. D. Thorncroft, 2006: Intense convective systems in West Africa and their relationship to the African easterly jet. *Quart. J. Roy. Meteor. Soc.* **132**, 163-176.
- Mohr, K. I., J. Molinari, and C. D. Thorncroft, 2009: The interannual stability of cumulative frequency distributions for convective system size and intensity. *J. Climate*, **22**, 5218-5231.
- Nesbitt, S. W., E. J. Zipser, and D. J. Cecil, 2000: A census of precipitation features in the Tropics using TRMM: Radar, ice scattering, and lightning observations. *J. Climate*, **13**, 4087-4106.
- Nesbitt, S. W., R. Cifelli, and S. A. Rutledge, 2006: Storm morphology and rainfall characteristics of TRMM precipitation features. *Mon. Wea. Rev.*, **134**, 2702-2721.
- Nicholls, S. D., and K. I. Mohr, 2010: An analysis of the environments of intense convective systems in West Africa in 2003. *Mon. Wea. Rev.*, **138**, 3721-3739.
- Nieto Ferreira, R., T. Rickenbach, N. Guy, and E. Williams, 2009: Radar observations of convective system variability in relationship to African easterly waves during the 2006 AMMA Special Observing Period. *Mon. Wea. Rev.*, **137**, 4136-4150.
- Nuret, M., J. Lafore, F. Guichard, J. Redelsperger, O. Bock, A. Agusti-Panareda, and J. N'Gamini, 2008: Correction of humidity bias for Vaisala RS80-A sondes during the AMMA 2006 Observing Period. *J. Atmos. Oceanic Technol.*, **25**, 2152-2158.
- Nzeukou, A., H. Sauvageot, A. D. Ochou, and C. M. F. Kebe, 2004: Raindrop size distribution and radar parameters at Cape Verde. *J. Appl. Meteor. Climatol.*, **43**, 90-105.
- Patterson, V. L., M. D. Hudlow, P. J. Pytlowaney, F. P. Richards, and J. D. Hoff, 1979: *GATE radar rainfall processing system*. NOAA Technical Memo. NOAA: National Technical Information Service, Sills Building, 5285 Port Royal Rd., Springfield, VA 22161.
- Payne, S. W., and M. M. McGarry, 1977: The relationship of satellite inferred convective activity to easterly waves over West Africa and the adjacent ocean during phase III of GATE. *Mon. Wea. Rev.*, **105**, 413-420.

- Peters, M., and G. Tetzlaff, 1988: The structure of West African squall lines and their environmental moisture budget. *Meteor. Atmos. Phys.*, **39**, 74-84.
- Redelsperger, J., A. Diongue, A. Diedhiou, J. Ceron, M. Diop, J. Gueremy, and J. Lafore, 2002: Multi-scale description of a Sahelian synoptic weather system representative of the West African monsoon. *Quart. J. Roy. Meteor. Soc.*, **128**, 1229-1257.
- Redelsperger, J., C. D. Thorncroft, A. Diedhiou, T. Lebel, D. J. Parker, and J. Polcher, 2006: African Monsoon Multidisciplinary Analysis: An international research project and field campaign. *Bull. Amer. Meteor. Soc.*, **87**, 1739-1746.
- Reed, R. J., D. C. Norquist, and E. E. Recker, 1977: The structure and properties of African wave disturbances as observed during Phase III of GATE. *Mon. Wea. Rev.*, **105**, 317-333.
- Rickenbach, T., R. Nieto Ferreira, N. Guy, and E. Williams, 2009: Radar-observed squall line propagation and the diurnal cycle of convection in Niamey, Niger, during the 2006 African Monsoon and Multidisciplinary Analyses Intensive Observing Period. *J. Geophys. Res.*, **114**, 8 PP.
- Rienecker, M. M., M. J. Suarez, R. Todling, J. Bacmeister, L. Takacs, H. Liu, W. Gu, M. Sienkiewicz, R. D. Koster, R. Gelaro, I. Stajner, and J. E. Nielsen, 2008: *The GEOS-5 Data Assimilation System – Documentation of Versions 5.0.1 and 5.1.0*. NASA GSFC Technical Report Series on Global Modeling and Data Assimilation. NASA: Hanover, MD; [online] Available from: [http://gmao.gsfc.nasa.gov/pubs/docs/GEOS5\\_104606-Vol27.pdf](http://gmao.gsfc.nasa.gov/pubs/docs/GEOS5_104606-Vol27.pdf)
- Roux, F., 1988: The West African squall line observed on 23 June 1981 during COPT 81: kinematics and thermodynamics of the convective region. *J. Atmos. Sci.*, **45**, 406-426.
- Roux, F., and S. Ju, 1990: Single-Doppler observations of a West African squall line on 27-28 May 1981 during COPT 81: Kinematics, thermodynamics and water budget. *Mon. Wea. Rev.*, **118**, 1826-1854.
- Sall, S. M., and H. Sauvageot, 2005: Cyclogenesis off the African coast: The case of Cindy in August 1999. *Mon. Wea. Rev.*, **133**, 2803-2813.
- Sauvageot, H., and J. Lacaux, 1995: The shape of averaged drop size distributions. *J. Atmos. Sci.*, **52**, 1070-1083.
- Schumacher, C., and R. A. Houze, 2003: Stratiform rain in the Tropics as seen by the TRMM precipitation radar. *J. Climate*, **16**, 1739-1756.

- Schumacher, C., and R. A. Houze, 2006: Stratiform precipitation production over sub-Saharan Africa and the tropical East Atlantic as observed by TRMM. *Quart. J. Roy. Meteor. Soc.*, **132**, 2235-2255.
- Shinoda, M., T. Okatani, and M. Saloum, 1999: Diurnal variations of rainfall over Niger in the West African Sahel: a comparison between wet and drought years. *Int. J. Climatol.*, **19**, 81-94.
- Steiner, M., R. A. Houze, and S. E. Yuter, 1995: Climatological characterization of three-dimensional storm structure from operational radar and rain gauge data. *J. Appl. Meteor.*, **34**, 1978-2007.
- Taleb, E. H., and L. M. Druyan, 2003: Relationships between rainfall and West African wave disturbances in station observations. *Int. J. Climatol.*, **23**, 305-313.
- Thorncroft, C. D., N. M. J. Hall, and G. N. Kiladis, 2008: Three-dimensional structure and dynamics of African easterly waves. Part III: Genesis. *J. Atmos. Sci.*, **65**, 3596-3607.
- Weisman, M. L., and J. B. Klemp, 1982: The dependence of numerically simulated convective storms on vertical wind shear and buoyancy. *Mon. Wea. Rev.*, **110**, 504-520.
- Weisman, M. L., J. B. Klemp, and R. Rotunno, 1988: Structure and evolution of numerically simulated squall lines. *J. Atmos. Sci.*, **45**, 1990-2013.
- Zipser, E.J., C. H. Twohy, S. Tsay, N. C. Hsu, G. M. Heymsfield, K. L. Thornhill, S. Tanelli, R. Ross, T. N. Krishnamurti, Q. Ji, G. Jenkins, S. Ismail, R. Ferrare, G. Chen, E. V. Browell, B. Anderson, R. Hood, H. M. Goodman, A. Heymsfield, J. Halverson, J. P. Dunion, M. Douglas, and R. Cifelli, 2009: The Saharan air layer and the fate of African easterly waves—NASA's AMMA field study of tropical cyclogenesis. *Bull. Amer. Meteor. Soc.*, **90**, 1137-1156.

**PART III: REGIONAL COMPARISON OF WEST AFRICAN CONVECTIVE  
CHARACTERISTICS: A TRMM-BASED CLIMATOLOGY**

## CHAPTER 1

### INTRODUCTION

The West African monsoon (WAM) is characterized by the northward migration of low-level (Gulf of Guinea) moisture to continental regions, and encompasses a complex interaction of multi-scale phenomena yet to be fully understood, in part due to limited long-term observations. The northward shift of the precipitation maximum supplies a majority of precipitation (Laurent et al. 1998; Mathon et al. 2002) to normally arid continental African regions, such as the Sahel, where mesoscale convective systems (MCSs) are responsible for the majority (> 80%) of rainfall totals (Le Barbé and Lebel 1997; D'Amato and Lebel 1998; Laurent et al. 1998; Redelsperger et al. 2002; Fink et al. 2006).

The Saharan heat low in northern Africa results in the convergence of dry northerly and moist southwesterly low-level flows, known as the intertropical discontinuity (ITD), which leads to strong baroclinicity across this boundary. These energetics along with the moist and dry convective contrasts lead to the development of the African easterly jet (AEJ), a strong, relatively dry mid-level jet with core centered around 600–700 hPa. Surface westerly winds are overlaid by the AEJ, with potentially unstable conditions at low-levels. This instability leads to the formation and

maintenance of (often intense) MCSs (Aspliden et al. 1976; Payne and McGarry 1977; Houze and Betts 1981; Barnes and Sieckman 1984; Rowell and Milford 1993; Hodges and Thorncroft 1997; Mohr and Thorncroft 2006; Nicholls and Mohr 2010). These westward moving systems generally exhibit a linear (squall line) morphology over the continent (Hamilton et al. 1945; Eldridge 1957; Bolton 1984), a non-squall (amorphous) morphology over the eastern Atlantic (Schumacher and Houze 2003 2006; Fuentes et al. 2008), and a transition stage upon exiting the coast (Sall and Sauvageot 2005; DeLonge et al. 2010).

Modulation of precipitation (and deep convective events) with synoptic disturbances in the form of African easterly waves (AEWs) has been suggested by many previous studies (Carlson 1969; Burpee 1974; Duvel 1990; Diedhiou et al. 1999; Fink and Reiner 2003; Gu et al. 2004; Petersen and Boccippio 2004; Mekonnen et al. 2006, Guy et al. 2011). The wave disturbances, which may be initiated east of 20°E (Berry et al. 2005; Thorncroft et al. 2008), are maximized near the AEJ level and progress westward at  $\sim 8 \text{ m s}^{-1}$ , with a wavelength of 2000–4000 km. Deep convection has been observed behind (to the east of) AEW troughs inland and in the eastern Atlantic and ahead (to the west) of and within AEW troughs near the coast (Payne and McGarry 1977; Reed et al. 1977; Duvel 1990; Machado et al. 1993; Diedhiou et al. 1999; Kiladis et al. 2006). Westward-propagating MCSs in West Africa often move faster than AEW troughs (Aspliden et al. 1976; Fortune 1980; Fink et al. 2006), and interact with the larger scale environment through the transport of momentum (Moncrieff 1992) and moisture (Lafore et al. 1988) and can reinforce cyclonic rotation when embedded in an AEW trough (Barthe et al. 2010).

A number of field campaigns have provided observational data for limited time periods, including the Global Atmospheric Research Program Atlantic Tropical Experiment (GATE; Houze and Betts 1981) and the Convection Profonde Tropicale (COPT-81; Sommeria and Testud 1984) experiment, providing important information regarding AEWs and MCS structure. More recently, the African Monsoon Multidisciplinary Analyses (AMMA; Redelsperger et al. 2006) campaign was organized to ‘improve our knowledge and understanding of the West African monsoon’. The release of the International Science Plan for the second phase of AMMA (2010–2020; [http://www.amma-international.org/IMG/pdf/ISP2\\_v2.pdf](http://www.amma-international.org/IMG/pdf/ISP2_v2.pdf)) summarized results from the first phase and stated the need to understand not only the meridional, but zonal characteristics of the WAM along the spectrum of phenomena that make up the WAM system. The characterization of regional convective characteristics encompasses mesoscale portions of the WAM and is useful in the validation of numerical simulations using explicit and parameterized formulations in cloud-resolving and general circulation models.

Satellite-based studies of convective characteristics in various meteorological regimes have been used to look at the broad-scale aspects of convection and their coupling to large-scale forcing (Petersen and Rutledge 2001; Toracinta et al. 2002; Fink and Reiner 2003; Nesbitt and Zipser 2003; Petersen and Boccippio 2004; Xu et al. 2009; Leppert and Petersen 2010). Additionally, regional characteristics have also been compared (Nesbitt et al. 2000; Geerts and Dejene 2005; Schumacher and Houze 2006; Zipser et al. 2006; Liu et al. 2008; Fuentes et al. 2008; Nicholls and Mohr 2010). Within Africa, latitudinal (e.g. Geerts and Dejene 2005) and longitudinal (e.g. Schumacher and

Houze 2006; Fuentes et al. 2008) convective characteristics have been explored, though the regions in these studies generally encompassed at least one large horizontal domain, essentially smoothing out variability in one dimension. Ground-based radar has been used to study smaller mesoscale regions (Petersen et al. 2003; Cifelli et al. 2007; Guy et al. 2011), though these studies encompassed short time periods and far smaller areas compared to satellite studies. Increased awareness of zonal and meridional inhomogeneity of precipitation and convective characteristics resulting from the AMMA project underscores the need for more detailed analysis of convective structures within a smaller regional domain, highlighting meso- $\alpha$  and - $\beta$  scale systems.

Increasing attention has been paid to cloud properties (and microphysics) of West African convective systems (Cetrone and Houze 2009,2011; Bouniol et al. 2010; Evaristo et al. 2010; Penide et al. 2010). Cloud properties, such as particle size and concentration, have been shown to vary by region (e.g. Protat et al. 2010), which are important in model simulations due to factors such as radiation feedbacks and mass transport. Analyzing these differences between distinct West African regions may provide useful information for model simulations.

This study reports on “climatological” convective characteristics of precipitation features identified by the Tropical Rainfall Measurement Mission (TRMM) satellite in seven distinct regions, at a scale smaller than previous studies in an attempt to illuminate the inherent geographical differences that are present in West Africa. Characteristics were partitioned into AEW phase (trough, northerly, ridge, and southerly) and when no AEW wave was present to examine differences associated with synoptic-scale regimes. This study intends to provide a climatological context in which to compare future

regional model simulations of single MCSs and simulations of mesoscale and synoptic-scale domains where cloud resolving model output may be compared. Additionally, relating results attained from ground-based radar observations to climatological spaceborne observations can help put differences in these observations into perspective.

## CHAPTER 2

### DATA AND METHODOLOGY

Seven regions, each encompassing a  $6^\circ \times 6^\circ$  box, in West Africa were chosen (Fig. 2.1) for analysis. The zonal distributions of northern (ConNE, ConNW, Cos, MarN) and southern (ConSE, ConSW, MarS) regions correspond to two commonly identified AEW latitude tracks (Reed et al. 1977; Nitta et al. 1985; Pytharoulis and Thorncroft 1999; Diedhiou et al. 1999; Thorncroft and Hodges 2001; Fink and Reiner 2003). The ConNE, Cos, and MarN regions were contrasted for zonal variations and were chosen to correspond to ground-based radar locations used in Guy et al. (2011). Adjacent southern regions allowed the examination of meridional variability. Region size was chosen to restrict comparisons to meso- $\alpha$  size and smaller, while capturing a large enough sample size to produce a meaningful “climatological” study. The ConNE region was centered north of the Niamey, Niger ground-based radar location used in Guy et al. (2011). This offset was necessary to ensure the ConSE region sampled mostly continental convective systems and minimized extension into the Gulf of Guinea. The MarS region roughly encompassed the GATE domain corresponding to ship-board radar observations.

The primary sources of data in this study are TRMM precipitation radar (PR) and microwave imager (TMI) observations and retrievals (Kummerow et al. 1998, 2000). The University of Utah TRMM precipitation feature (PF) database (Nesbitt et al. 2000; Liu et al. 2008) was employed to assess convective characteristics in each region from May–October (period of AEW activity) during 1998–2010. The PF database incorporates many standard product outputs (i.e. 2A25; TRMM PR 3–D reflectivity) along with calculated statistics (i.e. minimum 85–GHz microwave brightness temperatures); see Liu et al. (2008) and references therein for a complete discussion. Three–dimensional PR, 85– and 37–GHz polarization corrected temperatures (PCTs), and stratiform fraction were used in this study. Contiguous pixels of PR reflectivity with near surface rain defined the PFs. Stratiform fraction was calculated for each PF by dividing the number of pixels identified as stratiform by the total number of pixels associated with the PF, which was also used in area calculations. The footprint of a PR pixel increased following the August 2001 TRMM satellite orbit boost to extend lifetime (approximately 18.5 km<sup>2</sup> pre-boost and 25.0 km<sup>2</sup> post-boost), which also increased the minimum detectable reflectivity threshold from 17 to 18 dBZ. Only PFs with area greater than 75 km<sup>2</sup> and at least one pixel of reflectivity greater than 30 dBZ were retained (Tables 2.1–2.2).

Calculation of ice water mass and liquid water mass using three–dimensional PR data followed the methodology of Petersen et al. (2005). Briefly, vertical profiles (250 m spacing) of radar reflectivity (Z) for every PF were processed. Ice water content (IWC, from the –5°C level to echo top) was calculated for each vertical PR gate using an

exponential size (mass,  $M$ ) distribution in the form of an  $M$ – $Z$  relationship (Carey and Rutledge 2000):

$$IWC = 1000\pi\rho_i N_0^{3/7} \left( \frac{5.28 \times 10^{-18}}{720} Z \right)^{4/7} \quad (\text{g m}^{-3}), \quad (2.1)$$

where  $IWC$  is mass per volume,  $Z$  is in  $\text{mm}^6 \text{m}^{-3}$ ,  $N_0$  is the constant intercept parameter ( $4 \times 10^6 \text{m}^{-4}$ ), and bulk ice density ( $\rho_i$ ) varies between 100 and 800  $\text{g m}^{-3}$  as a function of  $Z$  and precipitation type (stratiform or convective). Similarly liquid water content ( $LWC$ ; from near surface to the  $0^\circ\text{C}$  level) was calculated for points over ocean (Tokay and Short 1996) via:

$$LWC = 5.338 \times 10^{-4} Z^{0.813} \quad (\text{g m}^{-3}), \quad (2.2)$$

and for coastal and land points (Tokay et al. 2002) via:

$$LWC = 3.5 \times 10^{-3} Z^{0.536} \quad (\text{g m}^{-3}). \quad (2.3)$$

The  $0^\circ\text{C}$  and  $-5^\circ\text{C}$  levels were climatological heights (approximately 4 and 5 km, respectively) found as a function of location using NCEP reanalysis data (Petersen et al. 2005). Because of difficulties in calculating mass contents in mixed–phase conditions, no attempt was made to estimate  $IWC$  or  $LWC$  between the  $0^\circ\text{C}$  and  $-5^\circ\text{C}$  levels. The  $IWC$  and  $LWC$  calculations are approximate as a number of assumptions are used to develop these relationships. Because this study will focus on comparing the relative trends and magnitude, any errors in relationships should not impact study results. It is also important to note that echo top corresponds to  $\sim 17$ – $18$  dBZ (depending on pre– or post–boost), the minimum detectable signal for the PR, which obviously does not correspond to actual storm top height. Similar fractions of PFs occurred before the orbital boost in each region; therefore no bias was applied to any one region.  $LWC$  and

IWC were vertically integrated to attain liquid water path (LWP) and ice water path (IWP) estimates and averaged for each PF. The bulk of IWC resides at reflectivity values above 17 dBZ, therefore the estimation of IWC should not be greatly impacted by the PR threshold.

All native and calculated data were partitioned according to AEW phase (trough, southerly, ridge, and northerly) and no-wave regimes. European Centre for medium-range weather forecasts interim reanalysis (ERA-Interim; Simmons et al. 2007) zonal and meridional winds (fixed 1.5° gridded) were employed to diagnose AEW vorticity centers (via streamfunction calculation, essentially eliminating divergent flow) at 700 hPa for West Africa (0–30°N, 30°E–30°W). Berry et al. (2007) developed a method to decompose the calculated streamfunction vorticity into shear and curvature components; and use the westward advection of curvature vorticity to identify AEW trough and ridge regions. In this methodology, trough or ridge axes were identified where westward advection of curvature vorticity is equal to zero. The same curvature vorticity threshold ( $0.5 \times 10^{-5} \text{ s}^{-1}$ ) suggested in Berry et al. (2007), was used to distinguish between ridge and trough classifications (following manual inspection of multiple individual time steps, not shown). Removal of pseudo-troughs (–ridges) resultant from local minima (maxima) of non-divergent wind curvature was accomplished via a second thresholding mask. Points retaining trough or ridge classification following the masking procedures were identified as such. An example of a trough-classified system is shown in Fig. 2.2.

Mean meridional winds at each longitude were calculated for each year to establish background flow. Criteria for southerly (northerly) phase designation followed the reasoning that negative (positive) curvature vorticity advection occurred east (west)

of a trough, along with meridional wind components greater (less) than the calculated mean. Points that did not meet any of the criteria above were designated as being not associated with an AEW phase (no-wave). Bain et al. (2011) discussed limitations of the composite view of AEWs, noting that there is a spectrum of wave structures possible over West Africa. With this in mind, a specific distance from trough or ridge axes was not used as a classification criterion in this study. Instead, the algorithm employed can be used to identify regions consistent with dynamics of each wave phase. Analysis of these maps (not shown) revealed that the identified regions were slightly smaller than the 500 km distance associated with triggering and maintenance of convection (Berry 2009; Nicholls and Mohr 2010). Since regions are compared against one another, the large PF sample size should smooth out any natural variability of convective location within an AEW phase region; this should not impact the results of this study.

Table 2.1. Number of precipitation features identified using TRMM precipitation radar and associated with objectively analyzed African easterly wave phase in northern regions in this study.

	Maritime North	Coastal	Continental Northwest	Continental Northeast
<b>Trough</b>	1372	1293	1021	443
<b>Southerly</b>	292	576	1066	1809
<b>Ridge</b>	649	940	1557	1354
<b>Northerly</b>	551	754	247	84
<b>No AEW</b>	1157	1735	1349	914
<b>Total</b>	4021	5298	5235	4607

Table 2.2. Number of precipitation features identified using TRMM precipitation radar and associated with objectively analyzed African easterly wave phase in southern regions in this study.

	Maritime South	Continental Southwest	Continental Southeast
<b>Trough</b>	3093	2896	1634
<b>Southerly</b>	4893	2377	2023
<b>Ridge</b>	5827	3992	3001
<b>Northerly</b>	2403	1487	1155
<b>No AEW</b>	5873	3587	2548
<b>Total</b>	22089	14339	10361

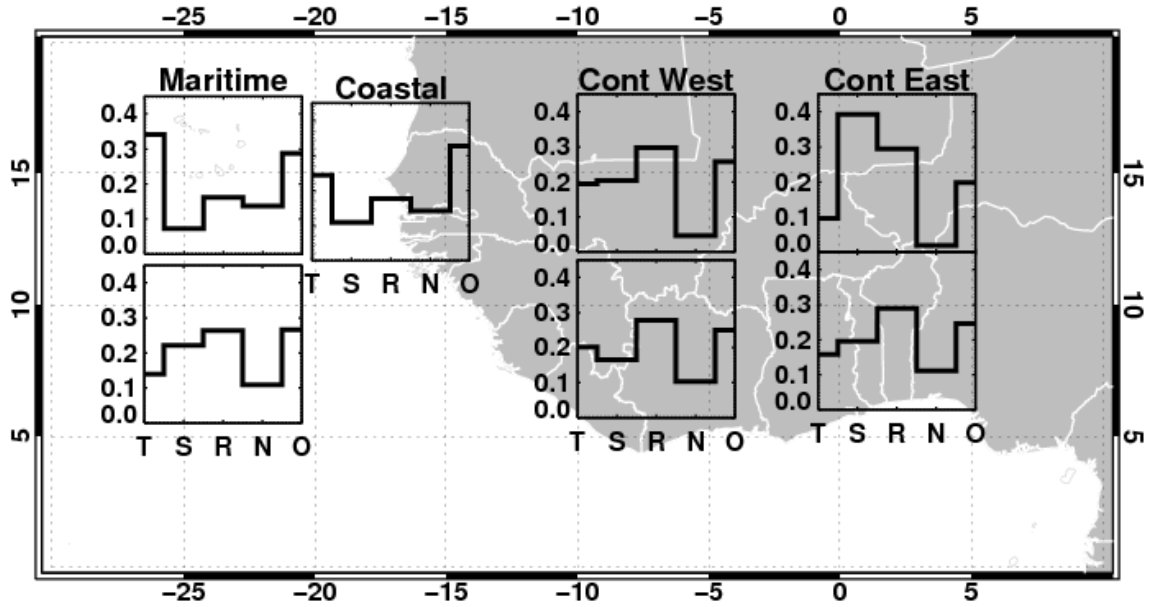


Fig. 2.1. West African and Atlantic Ocean regions ( $6^\circ \times 6^\circ$ ) chosen for climatological analysis. Plots inside each regional domain indicate the relative proportion of precipitation features (using contiguous precipitation radar reflectivity) occurring in the trough ('T'), southerly ('S'), ridge ('R'), and northerly ('N') African easterly wave phases; and when no wave was identified ('O'). Fractions are calculated by using the number of features in each phase divided by the total number of features in that region.

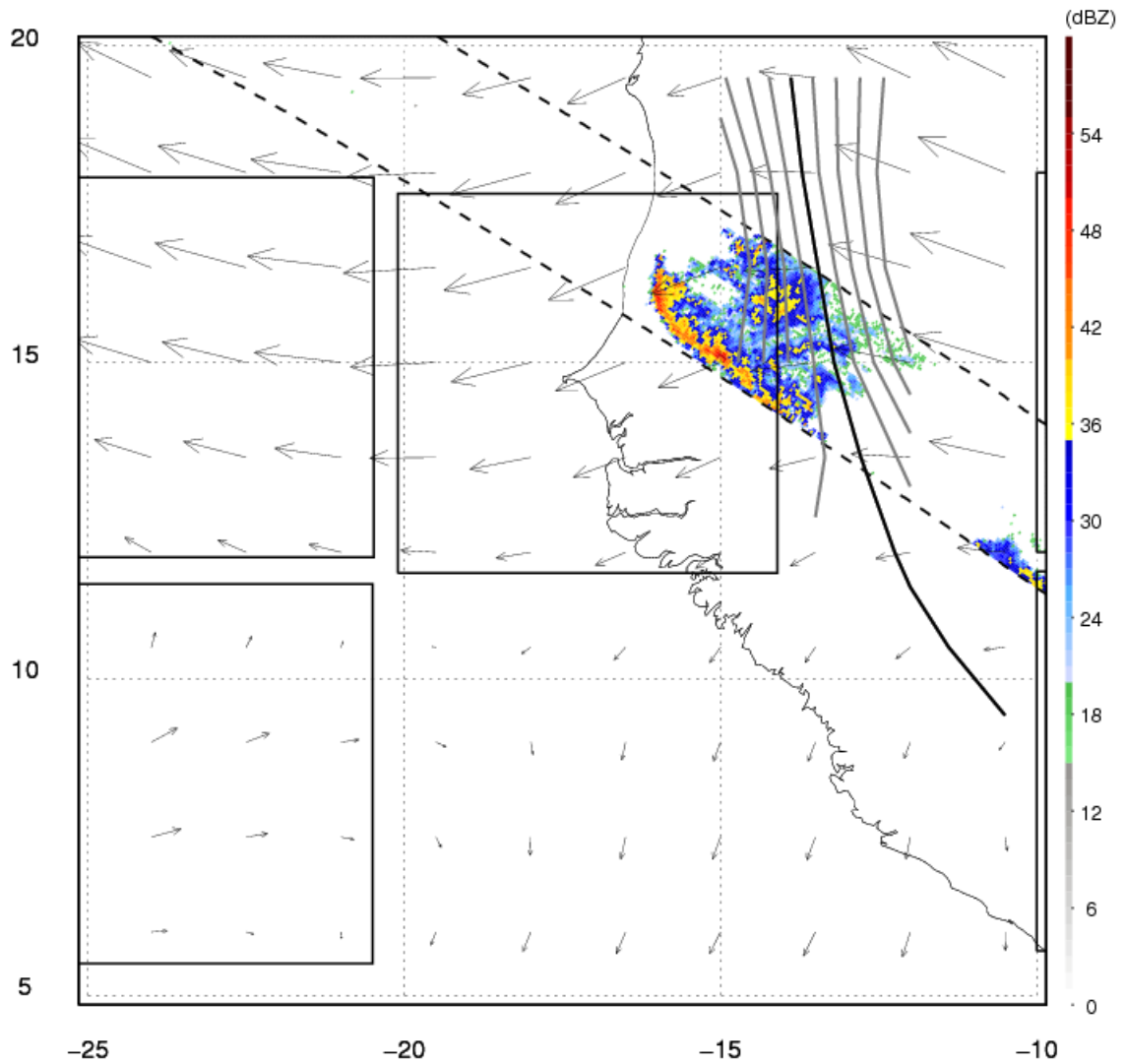


Fig. 2.2. TRMM overpass 50098 on 0530 UTC 31 August 2006 showing precipitation radar reflectivity swath. Boxes are regions discussed in this study, with the swath passing through the coastal region. Arrows indicate 700 hPa wind vectors. The solid black line is the objectively-identified African easterly wave trough axis for 0600 UTC on the same day. The gray contours show the identified trough region retained after thresholding procedure. Precipitation features within the coastal domain were identified as trough-associated for this case.

## CHAPTER 3

### RESULTS

#### *3.1. Precipitation feature characteristics*

Monthly frequency distributions for each region as a function of AEW phase (Fig. 3.1) showed lower frequency of occurrence for PFs in northern regions compared to southern regions, where a more favorable thermodynamic environment (e.g. low-level moisture, vertical wind shear) exists during May–October. Nicholls and Mohr (2010) showed that intense convective systems, identified as the top 10<sup>th</sup> percentile of minimum 85–GHz PCTs, clustered near the baroclinic zone produced by the WAM system, while weaker systems showed no clustering (but obviously more dense toward southern regions, see their Fig. 5). A seasonal peak in the drier northern regions was evident, consistent with the migration of the monsoon moisture and enhanced AEW activity. A greater number of PFs in northern continental regions associated with AEWs during May and June were related to the domain size which extended southward of the nominal location of the ITCZ capturing more consistent convective activity to the south during those months.

The highest AEW phase–associated PF frequencies (Fig. 2.1) occur in the southerly phase in the ConNE region, trough phase in the coastal and MarN regions, and

the ridge phase in ConNW, ConSW, ConSE and MarS regions. It is important to note that PFs represented snapshots of convective systems and genesis/lysis information may not be reliably extracted from this data alone. As mentioned previously, MCSs often travel faster than AEWs, and therefore life cycle characteristics could be aliased to wave regimes other than the formative and decay stages. Despite this limitation, occurrence frequency results were consistent with previous studies (most of which concentrated on genesis/lysis of MCS with respect to AEW phase) that have found that deep convection occurs east of AEW troughs near the continental sites and west of and in the trough near the coast and Atlantic (Carlson 1969; Reed et al. 1977; Payne and McGarry 1977; Diedhiou et al. 1999; Kiladis et al. 2006; Fink et al. 2006; Laing et al. 2008). Fink and Reiner (2003) and Laing et al. (2008), primarily using microwave and infrared observations for squall line and deep convective tracking, respectively; found a large fraction of systems were not associated with any AEW phase. Nearly equivalent or greater occurrence fraction associated with the No-Wave regime was found in every region except ConNE (where the least PFs were observed in the No-Wave phase).

Maximum storm height (MSH), corresponding to the highest detected pixel identified in raining columns (TRMM 2A23 product; rain characteristics), within a PF was used to compare vertical development between regions. Mean MSH over the continent was greater in the northern region (8.1–8.4 km vs. 7.3–7.5 km mean values for southern regions), while the maritime regions were the same (6.0 km). Mean values of MSH can obscure outliers (e.g. top 10 percentile) in the data; therefore it is of interest to examine the frequency distribution of observed heights. Cumulative frequency distributions (CFDs) of MSH for each region (Fig. 3.2) indicated greater variability

between AEW regimes over land, especially in ConSE. Frequency of PFs with MSH greater than 10 km increased from the Atlantic inland, with roughly 6–8% over the ocean, 10% at the coast, and 18–22% over land. Southern regions generally produced a higher frequency of taller convective systems (except ConNW); though mean values decreased due to the greater number of PFs with lower MSH values identified.

While the MSH is an indirect measure of the convective nature of systems, the majority of PFs in this study also contained multiple pixels identified as stratiform. Approximately 95% (90%) of PFs over land (ocean) had at least one pixel identified as stratiform. Not only does the stratiform component contribute to precipitation totals, but also plays an important role in the vertical heating profile of convective systems (Tao et al. 1993, 2010), making it of keen interest to analyze stratiform fractions (Fig. 3.3) for each region. Mean stratiform fractions were nearly the same (Table 3.1) between regions, with a slight decrease eastward from the Atlantic and coastal regions (~67%) to continental regions (~61%). The shape of the CFD regional curves in Fig. 3.3 showed that maritime regions experienced a higher occurrence of larger stratiform fraction. The separation of CFD curves for each AEW regime showed that large variability existed for stratiform fraction, as much as 20% in the case of ConSE. This result suggests different heating structures between AEW regimes, indicating the possibility of variable feedbacks onto both small- and large-scale atmospheric circulations.

As in Liu et al. (2008), mean PF area calculations showed larger systems over land than their oceanic counterparts (Table 3.1). Over the continent, the northern regions produced larger mean PF area than southern regions, discernible in Fig. 3.4 by the lower frequency of smaller events in ConNE and ConNW. In agreement with Guy et al. (2011),

AEW regimes produced an increased occurrence of larger systems in the ConNE, ConNW and coastal regions. Environmental factors such as strong low-level vertical wind shear aid the organization of intense convective systems (Frank 1978; Rowell and Milford 1993; Johnson et al. 2005; Mohr and Thorncroft 2006; Nicholls and Mohr 2010) over land. Stratiform precipitation is formed through the decay of convective regions and broad mesoscale ascent in the associated stratiform region (Zipser 1969; Houze 1977; Houze et al. 1989). A global climatology of convective inhibition (CIN) using the ECMWF ERA-40 reanalysis product (Riemann-Campe et al. 2009) showed higher mean CINs inland and in northern locations which may act as a cap, leading eventually to stronger convective development. Analyzing the number of PFs in each overpass (not shown) showed a higher percentage of the occurrence of a single PF in the ConNE domain (~35%) compared to the other regions (~26%). Along with larger mean PF size (Table 3.1), this supports the notion of suppression of small convective systems at the continental site.

Mean values of PF characteristics as a function of AEW regime are summarized in Fig. 3.5 for each region. These results indicated changes in convective characteristics as a function of phase in each region. Trough and ridge AEW regimes exhibited similar characteristics in a mean sense. While the trough phase displayed a more widespread convective signature (higher stratiform fraction, larger area), ridge phase convection was slightly more intense (lower 85-GHz PCTs, higher MSH and 30-dBZ heights). The southerly phase generally indicated more isolated, intense convection (relatively lower stratiform fractions, higher MSH and 30-dBZ heights, higher 85-GHz PCTs); while a decrease in convective strength was observed at all sites during the northerly AEW phase

(reduced MSH and 30–dBZ heights, lower 85–GHz PCTs, and larger stratiform fraction). Convection occurring when no AEW was identified was similar to that in the southerly AEW regimes, though an increased stratiform signature was evident. These differences suggested analysis of vertical convective characteristics, along with associated precipitation processes, may result in differences between AEW regime and region.

### *3.2. Vertical structure*

Mean vertical profiles of convective (Fig. 3.6) and stratiform (Fig. 3.7) radar reflectivity were produced for each region and separated by AEW regime. Results above 17 km were noisy and contained a much smaller number of points as only the deepest convective systems reached those levels. Intra–region AEW regime profiles were similar in Figs. 3.6–3.7, though convective profiles were stronger throughout in more eastward regions, that is, more interior to the continent. Coastal and continental convective profiles showed the largest deviations by AEW phase, where the southerly regime exhibited larger reflectivity values throughout the profile, which suggests stronger convective components associated with the southerly regime over land. Only the coastal location displayed a no–wave regime profile distinctive from AEW phases, in agreement with ground-based radar results in Guy et al. (2011), which examined the peak monsoon period (19 Aug–16 Sep) for 2006.

Each region exhibited a prominent brightband signature (enhanced reflectivity) in the stratiform profiles (Fig. 3.7) near 4.5 km, well–established as the tropical melting level, with rapid decrease in reflectivity above. The brightband is primarily due to aggregates of ice particles descending through the 0°C isotherm, which begin to melt

resulting in a stronger radar reflectivity due to differences in the dielectric constant between ice and water. Continental locations displayed more variability between AEW regimes above the brightband, while maritime regions showed almost no differences.

A comparison of regional vertical reflectivity profiles (Fig. 3.8) closely resembled results from Fuentes et al. (2008), where convective profiles (Fig. 3.8a) were more intense over land and in the coastal region than over the ocean. More intense convective components were confirmed by two separate proxies for convective intensity, listed in Table 3.1. First, mean maximum 30–dBZ heights (DeMott and Rutledge 1998) varied zonally, with continental north (~6.1 km) and south (~5.3 km) regions displaying the greatest 30–dBZ heights, decreasing westward in the coastal (4.7 km) and maritime (3.8 km) regions. Continental convection has been shown to contain stronger updrafts (e.g. Zipser and LeMone 1980; Lucas et al. 1994) allowing greater hydrometeor lofting, resulting in increased ice and graupel (i.e. mixed–phase) production aloft. The presence of ice hydrometeors aloft result in decreased mean minimum 85–GHz PCT values (Heymsfield and Fulton 1988; Mohr and Zipser 1996), or increased ice scattering signature, inland (shown later).

Near the surface, maritime convective reflectivity profiles continued to increase toward low levels, suggesting droplet growth mechanisms via warm rain (coalescence) processes. Continental and coastal regions were often associated with decreasing reflectivity towards the surface, indicating drop evaporation or drop breakup. Northern and southern domains exhibited similar convective reflectivity profiles below 6 km, with more variability aloft. Mean MSHs and 85–GHz PCTs (Table 3.1) were nearly identical,

suggesting that vertical growth and ice water path were also similar in a mean sense (discussed below).

Brightband signatures in stratiform profiles (Fig. 3.8b) were similar in magnitude in all regions except MarS, which was up to 2 dB weaker. Strong evaporative processes were observed in the ConNE region and to a lesser degree ConSE; inferred from the decrease of reflectivity below the brightband to low levels. The linear organization of continental MCSs would often lead to the presence of a rear inflow jet which may aid in the evaporative process. Reflectivity profiles for oceanic and coastal regions continued to increase toward the surface, an indication of moist lower levels. Unlike convective profiles, which exhibited distinct separations for each region, stratiform profiles were tightly grouped, except the MarS profile which displayed lower reflectivity values below 5 km. Maritime reflectivity profiles decreased more rapidly above the brightband than the coastal and continental regions, resulting in two distinct groupings from 5 km and upwards; maritime and continental. These differences in reflectivity profiles suggested varying ice and liquid water vertical distributions in each region and by AEW regime.

The non-parametric Spearman's rho correlation coefficient (which is less sensitive to outlier data than Pearson's rho) was calculated using the convective profiles as the independent variable and the stratiform profiles as the dependent variable. Results showed significant high positive correlations for all regions (0.53–0.93; only MarN exhibiting values less than 0.63), indicating that stratiform profile strength increased with convective profile strength. Comparing these results by AEW regime to the characteristics expressed at the end of Chapter 3.1, suggested that when stronger convective regions were present, the stratiform vertical reflectivity profiles exhibited

stronger characteristics, possibly due to larger ice mass fluxes from the intense convective regions. Additionally, organized systems tend to establish broader mesoscale ascent due to the increased stratiform portion. In leading–convective, trailing–stratiform type systems (as found frequently over the continent), ascending front–to–rear flow from convective cells to the stratiform region transports convective ice particles into the upper stratiform regions. Growth via vapor deposition during transport (Rutledge and Houze 1987), along with aggregation during particle descent in the stratiform region results in larger particles. These processes result in larger particles throughout much of the vertical extent of the convective systems, which yields stronger stratiform reflectivity profiles.

Mean vertical profiles of IWC and LWC were calculated using both convective and stratiform points. Large differences in the vertical distributions of IWC (Fig. 3.9) were revealed between regions. The continental regions contained the most ice water, with the coastal region containing less. Maritime regions contained the smallest ice mass contents. This suggested stronger updrafts inland, allowing ice microphysics to play a more important role in precipitation production at those locations. Contributions to total ice mass were found to be largely from the convective portion of storms (67–95%). As expected (due to the use of an M–Z relationship) this followed the distribution of the vertical profiles of convective reflectivity. The fact that the AEW southerly and ridge regimes contained larger amounts of ice water than other AEW regimes over land suggested the presence of significant updrafts, capable of producing large graupel, and probably even hail, particles that possess large fall speeds. This is consistent with lower stratiform fractions observed in these regions.

As suggested above, northern and southern region profiles were similar, though northern continental regions contained greater ice water throughout the profile than the southern regions. Mean minimum 37–GHz PCT was lower in ConSW than other continental regions (Table 3.1); which might indicate that ice hydrometeors aloft were larger in the ConSW region as the 37–GHz channel is more sensitive to larger ice particles.

Over MarS, a larger mean 37–GHz PCT depression was observed compared to MarN. The explanation of large ice particles seems unlikely given the similarities in both reflectivity and IWC profiles. Another possible explanation may be present in the vertical distributions of LWC (Fig. 3.10). You et al. (2011) suggested that in the presence of large amounts of ice and liquid hydrometeors and surface rainfall (required for LWC to be calculated), the 37–GHz channel shows a stronger response than other microwave channels. More liquid water in MarS low–levels than MarN, along with similar IWC distributions would support the larger 37–GHz depression in MarS. An increase in LWC was observed moving eastward; however, the relative profile shapes were quite different, with liquid water increasing to near–surface at each location except for the northern continental regions (where sub–cloud evaporation dominated). The contribution of the convective portion of systems to total liquid water mass was 40–68%, showing that stratiform contribution to liquid water mass was greater than for ice mass for all regions. Again variability was observed between AEW phases, with the southerly phase producing the largest amounts of liquid water in coastal and continental regions. Despite indications of more strong, isolated convective events (Fig. 3.5), the southerly AEW phase produces larger ice and water mass than the other AEW regimes.

### 3.3. *Microphysical characteristics*

Due to the variability of horizontal and vertical characteristics it was of interest to try to explore microphysical characteristics in a limited way, based upon radar reflectivity. The previous section suggested how microphysical processes in the regions varied as a function of AEW regime. These processes contribute to determining the characteristics associated with the population of PFs in each region. Minimum 85–GHz PCT distributions (Fig. 3.11) indicated a higher frequency of larger 85–GHz depressions (lower 85–GHz PCTs) over the continent, decreasing in occurrence westward into the Atlantic. Greater variability between AEW regimes was observed in the coastal and continental regions, but supported regional distributions of MSH (Fig. 3.2), where taller storms corresponded to greater ice scattering signatures, and more intense convective systems by other metrics (i.e. 30–dBZ heights and vertical reflectivity profiles). While the same zonal trend was observed in the southern regions; all southern regions exhibited a smaller frequency of larger 85–GHz depressions than northern counterpart regions. Minimum 37–GHz PCT distributions (not shown) resulted in the same conclusions, albeit with less variability between AEW phases, suggesting a robust relationship between the convective metrics used in this study in each region.

Low values of 85–GHz PCT are indicative of a large IWP (e.g. Xu et al. 2010), while low values of 37–GHz PCT are indicative of large ice particles or large amounts of mixed–phase particles. Therefore to determine both liquid and ice water contributions, IWP (Fig. 3.12) and LWP (Fig. 3.13) fractions (IWP or LWP divided by the sum of IWP and LWP, respectively) were calculated for every PF in each region as a function of AEW regime. All non–raining pixels were disregarded in the calculation of IWC and

LWC. Following separation into convective and stratiform components, IWP and LWP fractions allow a basic interpretation of precipitation processes. High IWP fractions along with low LWP fractions suggest a strong dependence on ice-based microphysics. On the other hand, low IWP and high LWP fractions suggest strong warm-rain processes.

The difference in stratiform and convective frequency distributions is evident in each region. Higher (lower) frequencies of high IWP (LWP) fractions were observed in convective portions, with the reverse true for the stratiform portion. Despite these similarities, large variability was observed both between regions and across AEW regimes for IWP and LWP fractions (Figs. 3.12–3.13). Maritime regions exhibited characteristics suggestive of warm-rain processes. The increased contribution of ice microphysics is apparent moving inland. Southern continental regions exhibited a more apparent warm-rain signature, whereas the northern continental regions exhibited a signature more dependent upon ice-based microphysics.

Tighter grouping of AEW phase distributions was observed over oceanic regions, suggesting system structure displayed greater homogeneity than observed inland. Convective distributions showed looser groupings across AEW phases than stratiform distributions in every continental (and coastal) region. This suggests that greater variability in convective microphysical structure was present. As mentioned previously, convective contributions dominated IWC, and to a lesser extent LWC, profiles. Additionally, steeper slopes in the oceanic and coastal distributions indicate a narrower range of ice and water mass fractions in these regions, whereas over the continent a greater spectrum of ice and water fractions were possible.

The southerly and ridge AEW phase systems produced more frequent higher IWP fractions in continental regions. This suggests that stronger updrafts existed during this phase, confirmed by higher MSH and 30-dBZ heights. Stratiform fractions shown in Fig. 3.3 indicate a lower occurrence of large stratiform fraction in the continental regions during the southerly and ridge AEW regimes, while the trough phase displayed opposite characteristics; lower IWP fraction, higher LWP fraction, and higher occurrence of larger stratiform fractions. Fundamental differences in convective system morphology and microphysical processes seem to exist between regions and AEW regime.

Table 3.1. Mean values of properties associated with precipitation features in the seven study regions – maritime north (MarN) and south (MarS), coastal, continental northwest (ConNW), northeast (ConNE), southwest (ConSW) and southeast (ConSE) – during May–October, 1998–2010.

	Feature Area (km <sup>2</sup> )	Maximum Storm Height (km)	Maximum 30–dBZ echo Height (km)	Minimum 85–GHz PCT (K)	Minimum 37–GHz PCT (K)	Stratiform Fraction (%)
MarN	1004	6.0	3.8	260	279	66.5
MarS	1279	6.0	3.8	262	264	67.5
Coastal	1654	7.0	4.7	248	271	67.5
ConNW	1752	8.4	6.2	239	276	60.6
ConNE	1831	8.1	6.0	240	275	61.1
ConSW	1253	7.3	5.2	245	265	63.7
ConSE	1511	7.5	5.4	240	277	61.1

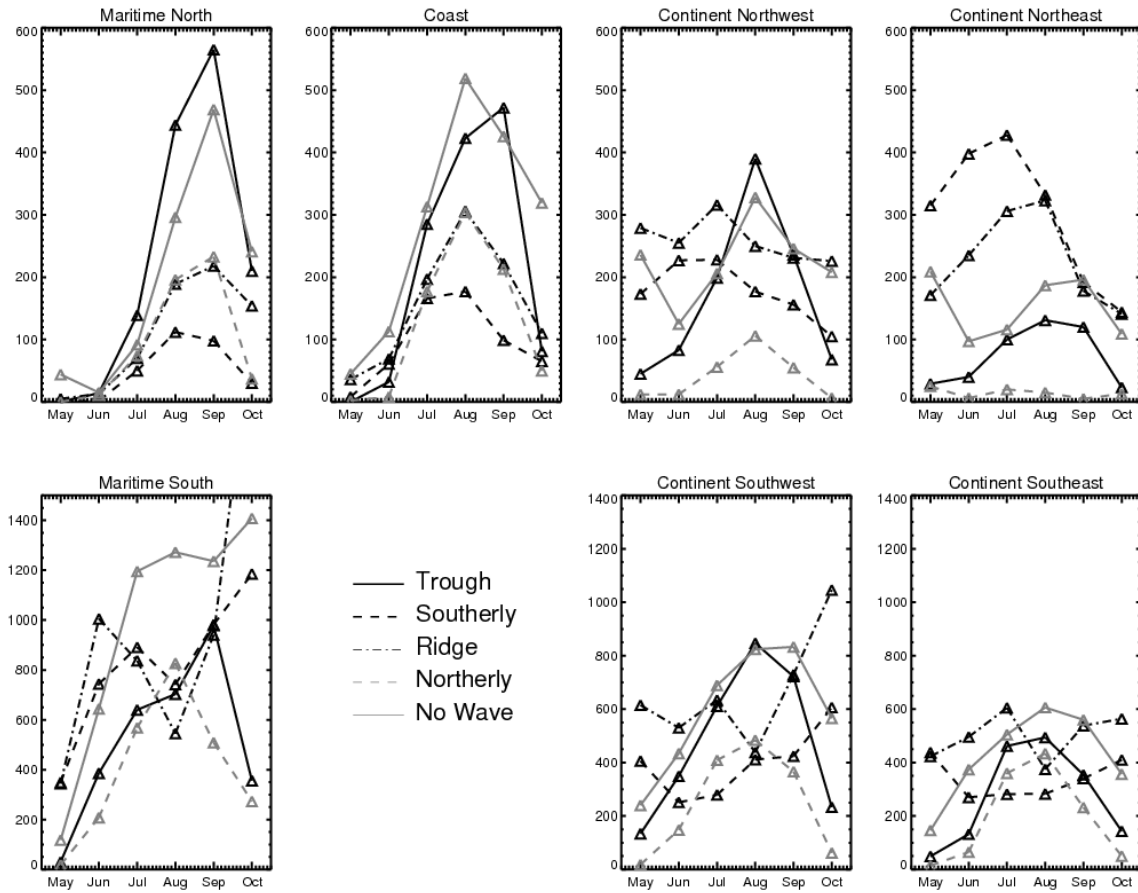


Fig. 3.1. Precipitation feature frequency distribution in each study region during May–October. Each month is partitioned by objectively identified AEW trough (solid black), southerly (dashed black), ridge (dotted black), and northerly (dashed gray) phase along with when no AEW phase (solid gray). Note the different ordinate axis scale between regions.

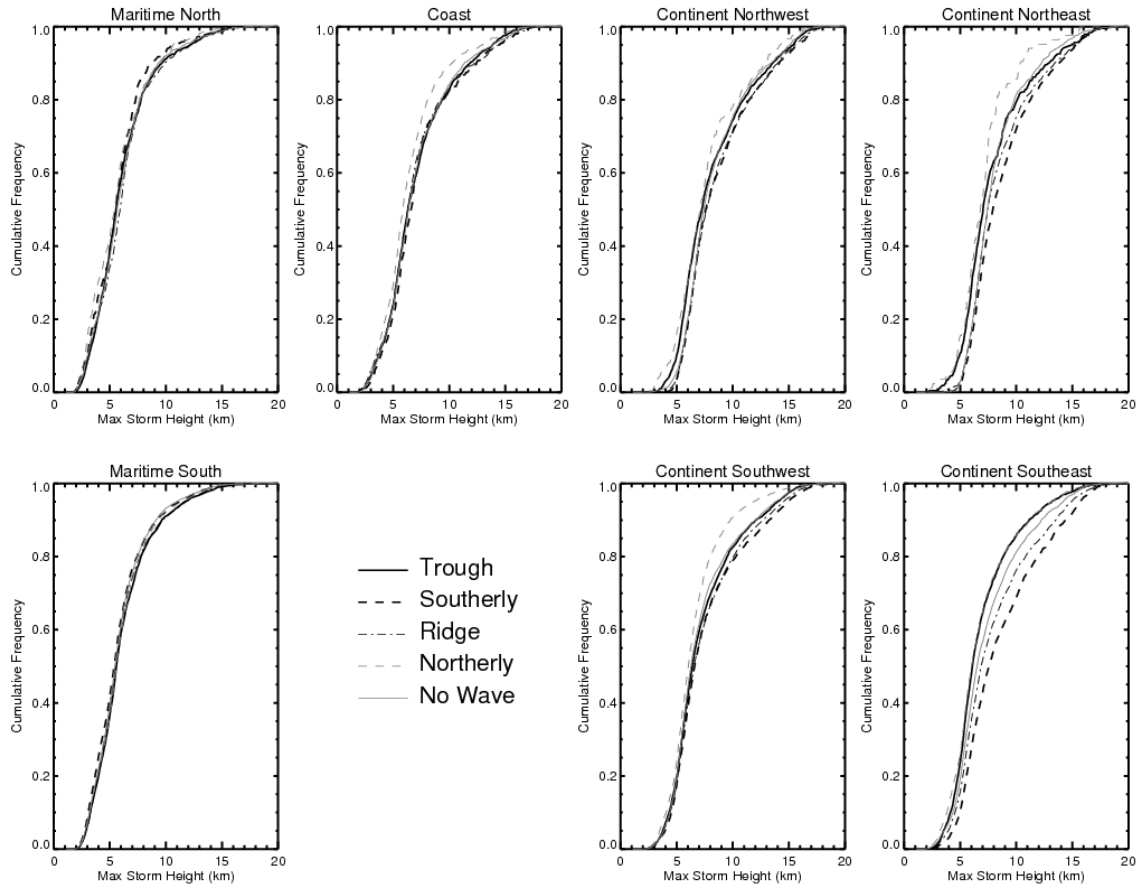


Fig. 3.2. Cumulative frequency distributions of precipitation feature maximum storm height for each study region. Objectively identified AEW phases along with no identified AEW are displayed as in Fig. 3.1.

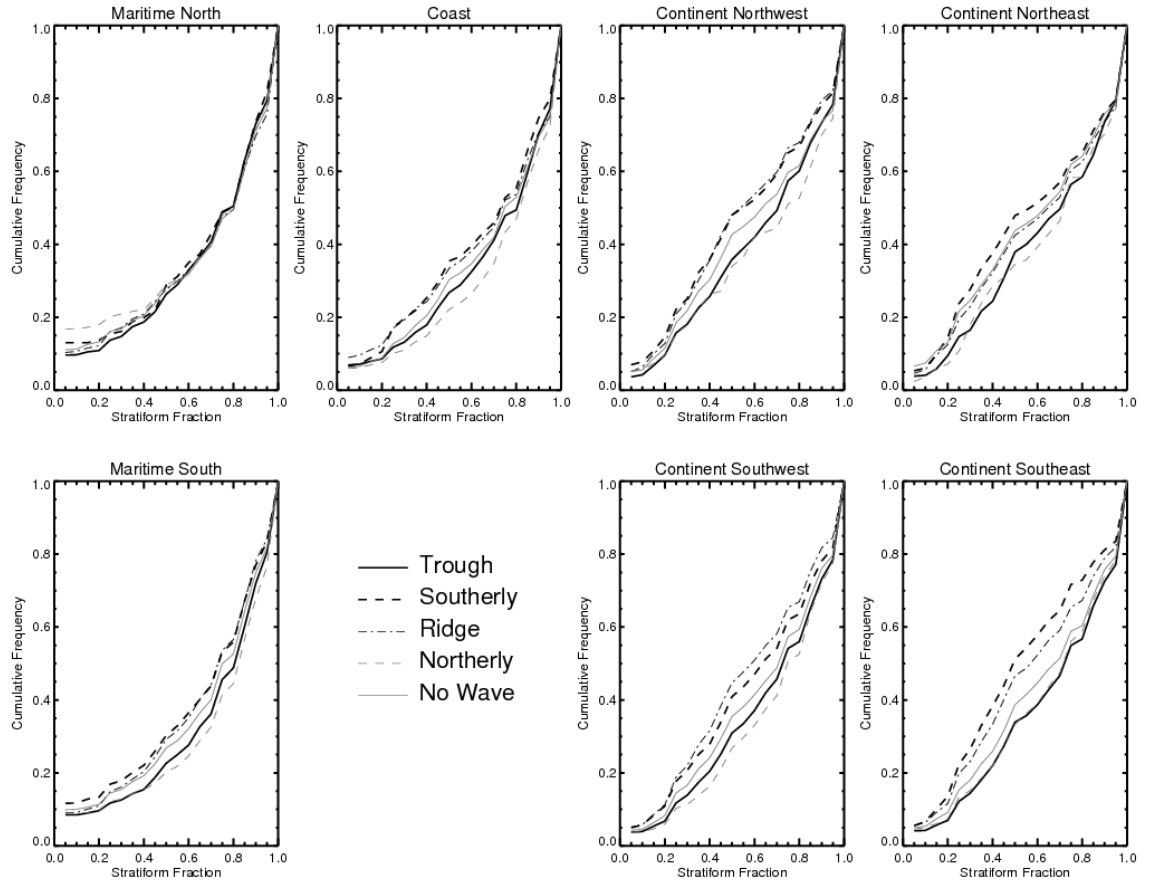


Fig. 3.3. As in Fig. 3.2, except for stratiform fraction.

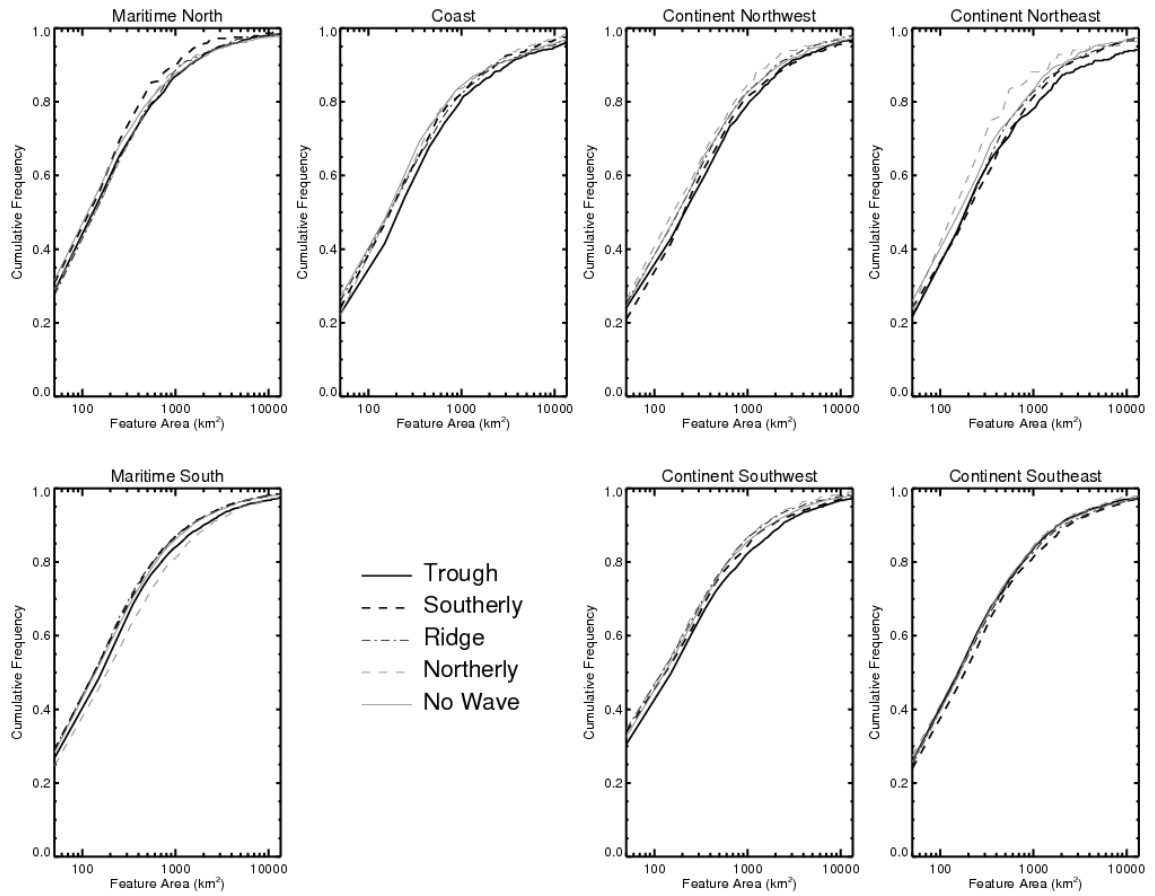


Fig. 3.4. As in Fig. 3.2, except for precipitation feature area.

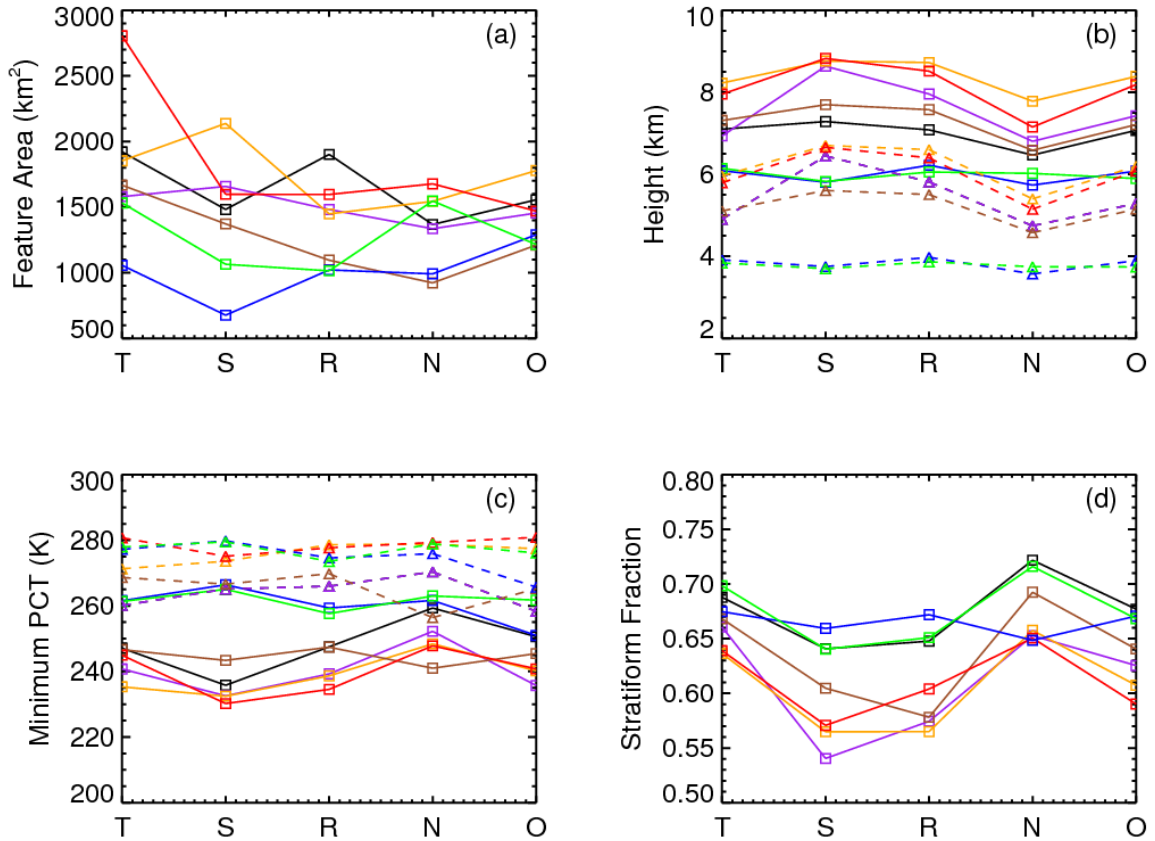


Fig. 3.5. Mean values of (a) feature area, (b) maximum storm height (solid lines with open squares) and 30-dBZ height (dashed lines with open triangles), minimum (c) 37-GHz (dashed lines with open triangles) and 85-GHz (solid lines with open squares) PCTs, and (d) stratiform fraction during trough ('T'), southerly ('S'), ridge ('R'), and northerly ('N') AEW phase and when no AEW phase is identified ('O'). Continental northeast (red), continental northwest (orange), continental southeast (purple), continental southwest (brown), coastal (black), maritime north (green), and maritime south (blue) regions are displayed.

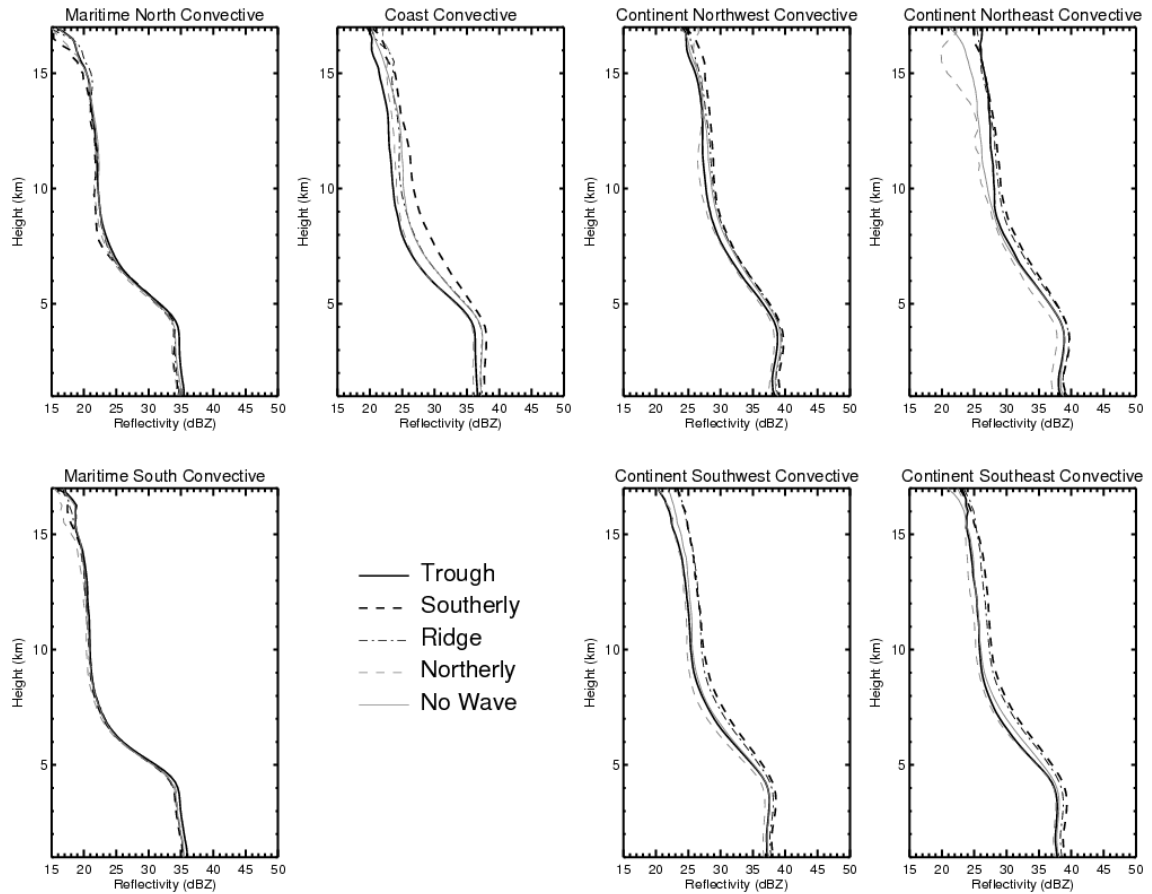


Fig. 3.6. Mean convective vertical reflectivity profiles of TRMM precipitation radar observations for each study region. Trough (solid black), southerly (dashed black), ridge (dotted black), and northerly (dashed gray) AEW phase along with no identified AEW (solid gray) are shown.

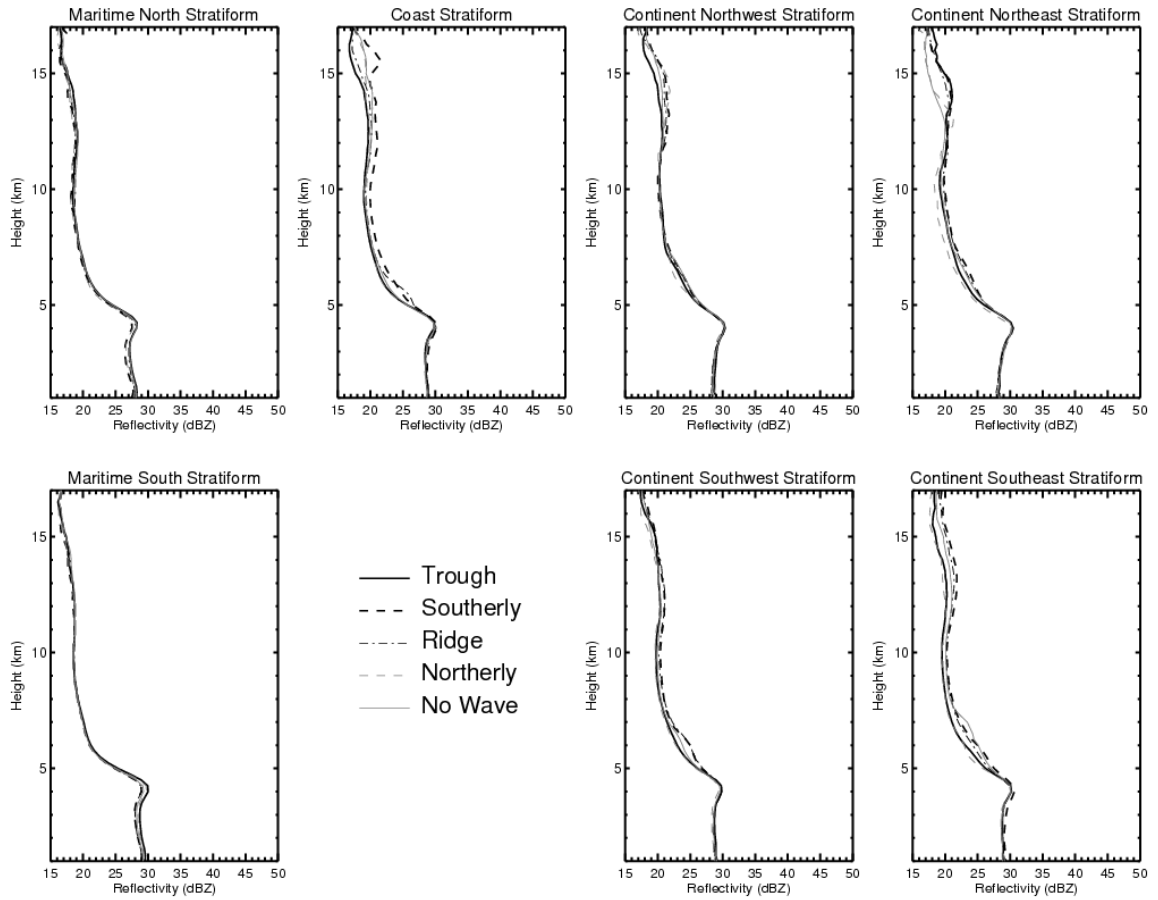


Fig. 3.7. Same as Fig. 3.6, except for stratiform component.

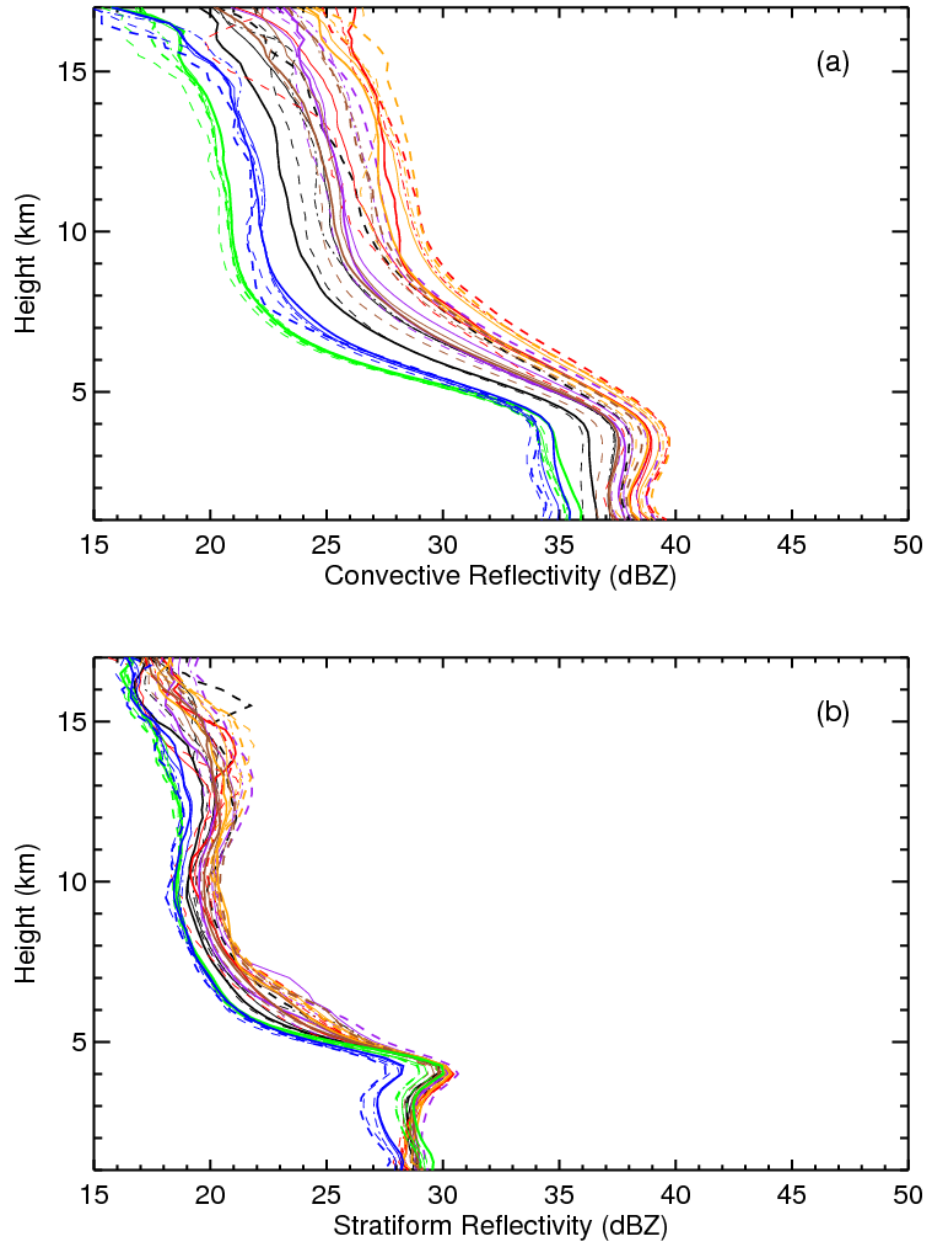


Fig. 3.8. Mean (a) convective and (b) stratiform vertical reflectivity profiles for continental northeast (red), continental northwest (orange), continental southeast (purple), continental southwest (brown), coastal (black), maritime north (green), and maritime south (blue) regions. Line styles as in Figs. 3.6–3.7, designating AEW phase.

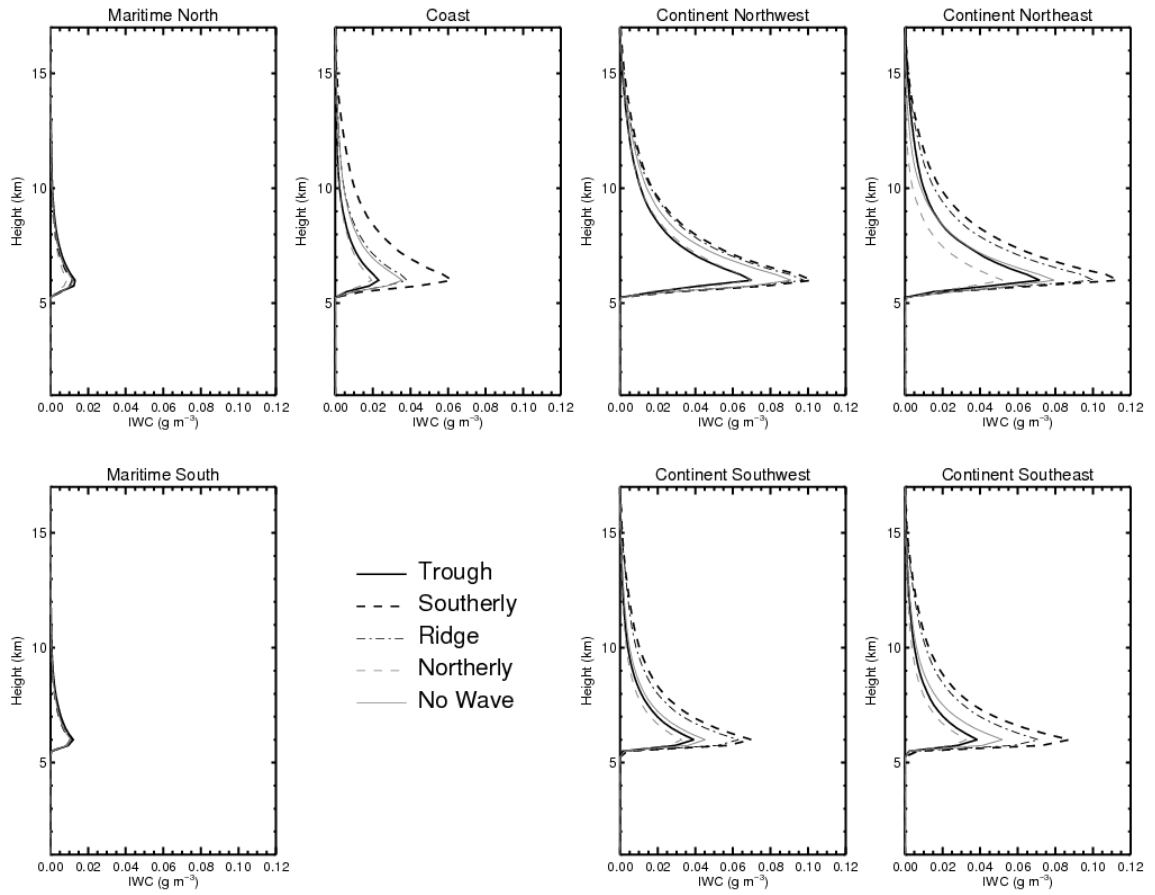


Fig. 3.9. Same as Fig. 3.6, except for ice water content.

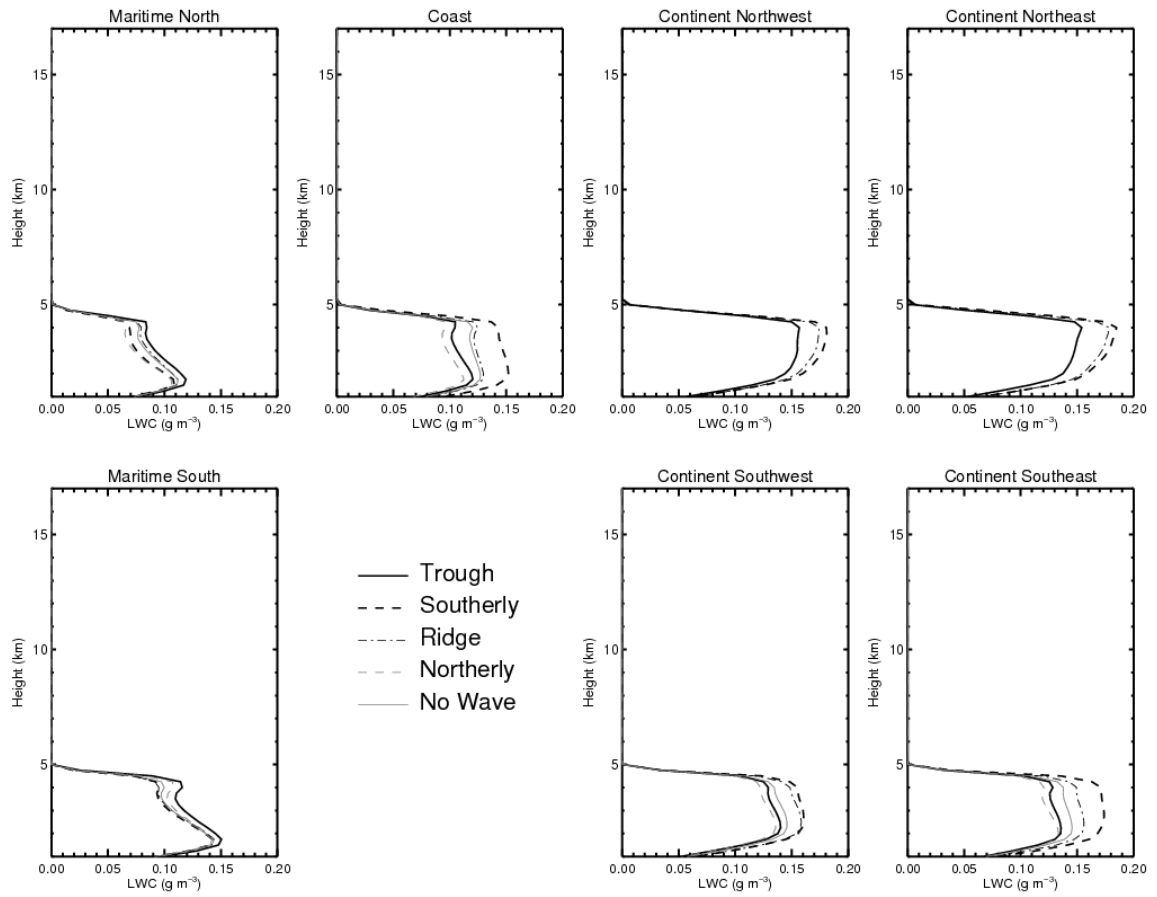


Fig. 3.10. Same as Fig. 3.6, except for liquid water content.

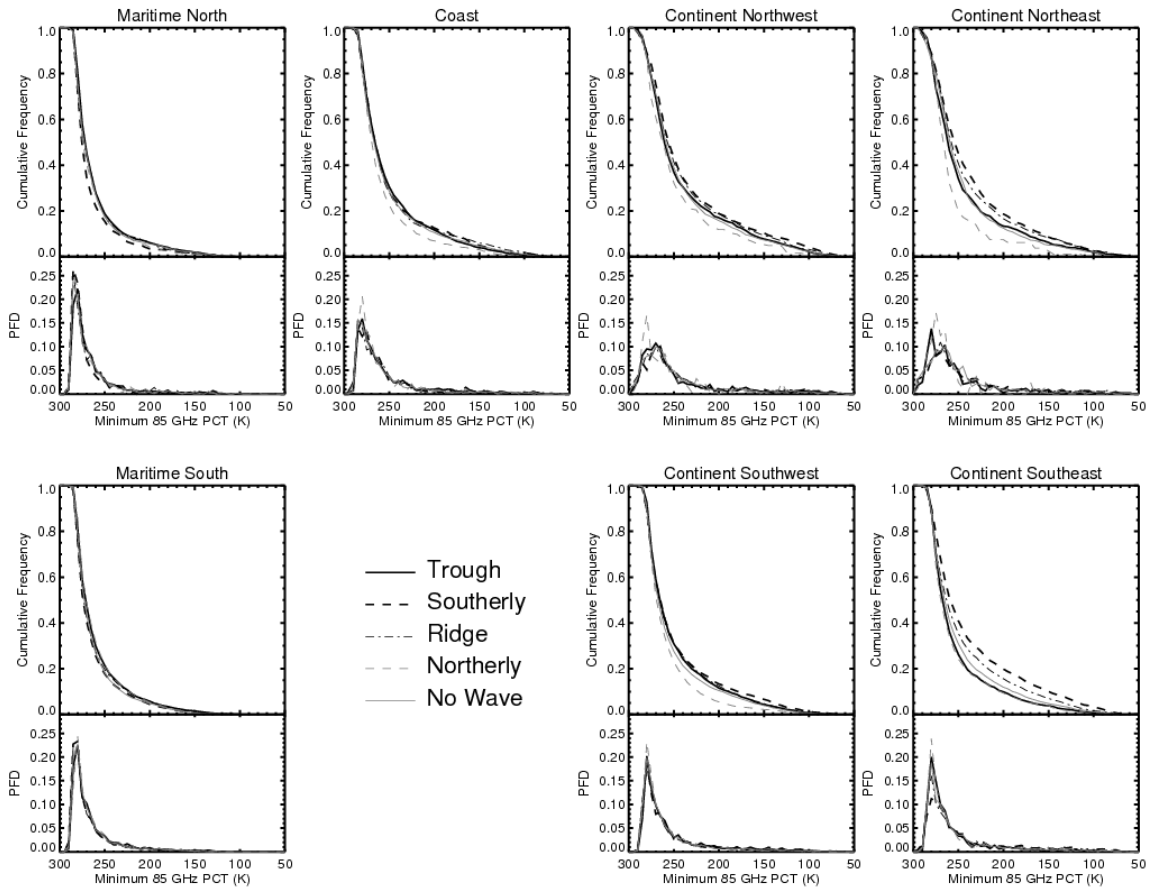


Fig. 3.11. Cumulative (top) and probability (bottom) frequency distributions, for each study region, of minimum 85-GHz polarization corrected temperature. Line styles as in Fig. 3.6.

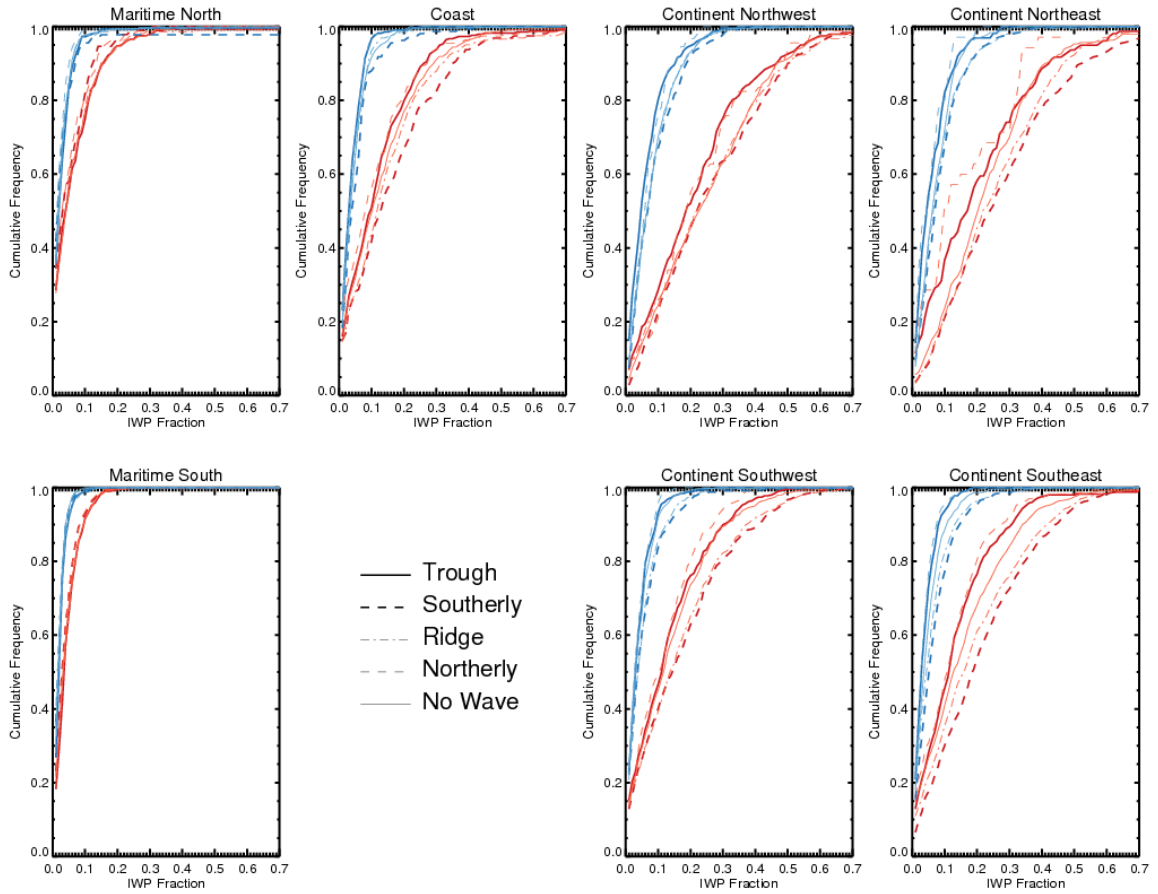


Fig. 3.12. As in Fig. 3.2, except for ice water path fraction, defined as ice water path divided by the sum of ice and liquid water path. Distributions are additionally separated by convective (red) and stratiform (blue) classification.

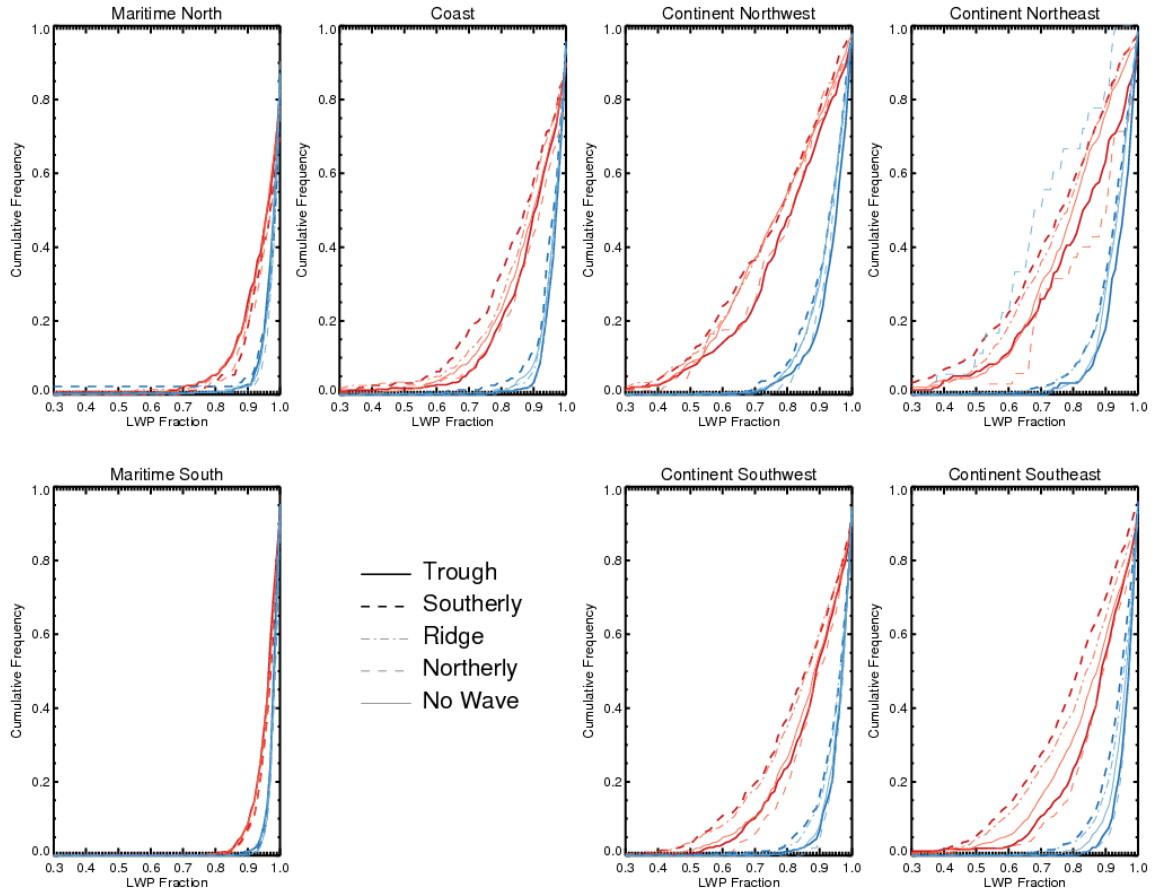


Fig. 3.13. As in Fig. 3.12, except for liquid water path fraction, defined as liquid water path divided by the sum of ice and liquid water path.

## CHAPTER 4

### CONCLUSION

A comparison of convective characteristics in seven distinct mesoscale regions influenced by the WAM was presented. Continental, coastal, and maritime regions were defined based upon ground–radar observations during the 2006 AMMA field experiment examined in Guy et al. (2011), along with an additional continental region between the coastal and continental regions mentioned to provide semi–continuous zonal coverage. Adjacent continental and maritime regions were included to the south to allow investigation of meridional variability. A 13–year “climatology” using precipitation features, based upon contiguous TRMM satellite PR pixels was developed using PR and TMI (37– and 85–GHz) observations. These data were subset by AEW phase (trough, southerly, ridge, and northerly) and when no AEW phase was identified using ERA–Interim winds and applying the Berry et al. (2007) AEW trough tracking algorithm, with additional phase identification.

Frequency distributions showed that PF populations in southern regions far outnumbered their northern counterparts. Southern regions experience a seasonal cycle of PFs more varied than the northern regions. For example, Fink et al. (2006) in a study of a subset of the ConSE region revealed that Sahelian–type SLMCSs were common

outside the peak WAM season, while organized MCS convection exhibited different precipitation characteristics (Sudano–Guinean; slower–moving, shorter–lived, and smaller areal coverage) during the monsoon season. Vertical extent and associated characteristics (e.g. 85–GHz depressions) may also be affected by this cycle. Northern regions primarily experienced fast–moving SLMCSs throughout the study, which may help to explain some latitudinal variability between regions. Feature association with AEW regime was in general agreement with previous studies, despite the fact that those studies focused largely on the generation and lysis of MCSs with respect to AEWs. Preferential occurrence east of AEW troughs near the continental sites and west of and in the trough near the coast and Atlantic was observed. All regions, except continental north, had a substantial number of PFs not associated with an AEW regime.

Magnitudes of regional differences were larger than AEW regime variability for convective characteristics, in agreement with the findings of Guy et al. (2011). Mean storm top and maximum 30–dBZ heights were lowest over maritime regions and increased moving eastward. The occurrence of tall (>10 km) storm top heights also increased over land. Though feature area increased from ocean to land, stratiform fraction trended slightly opposite, decreasing from the Atlantic over land. Schumacher and Houze (2003, 2006) observed a similar trend in stratiform fraction, though the differences between ocean and continent were larger than observed in this study. Enhanced mean 85–GHz depressions were observed over land, in agreement with previous studies.

Mean values during AEW phases and when no AEW was present indicated variability of convective characteristics as a function of synoptic regime. Characteristics

as a function of easterly phase differed from those found by Petersen and Boccippio (2004). The trough phase displayed a widespread convective signature, while the southerly phase generally indicated more isolated, intense convection. Convective characteristics during the ridge phase were slightly more intense than during the trough phase. A decrease in convective strength was observed during the northerly AEW phase. Convection occurring when no AEW was identified was similar to that in the southerly AEW regimes, with an increased stratiform signature.

The separation of convective reflectivity profiles by region was evident; while stratiform reflectivity profiles displayed similar features. The most notable differences appeared near the surface, likely due to environmental characteristics (moist over ocean and coast, drier inland; especially in northern regions). Influence of AEW regimes was more apparent in frequency distributions and vertical reflectivity profiles in the coastal and continental regions than the maritime regions. Generally, the southerly, and to a lesser degree the ridge regime, resulted in strengthened convective intensity metrics over land, revealing enhancement of the convective portion of MCSs. Of interest, the distribution of stratiform fraction showed large variability between AEW regimes despite less variability in area distributions between AEW regimes. This result is important given the implications of differences of latent heating interaction with the larger environment. Characteristics of PFs that occurred during the no-wave regime displayed convective characteristics similar to those during AEW regimes, suggesting that while AEWs can act to enhance certain features of convective systems, regional variability of thermodynamic environments play a crucial role in system organization.

Microphysical characteristics displayed large variability both regionally and between AEW regimes. Vertical profiles of IWC revealed values up to an order of magnitude greater over the continent compared to maritime regions, with peak values differing by a factor of three between AEW regimes. Profiles of LWC also indicated variability between AEW regimes, though less difference in regional LWC profiles was observed. The convective portion of systems dominated contribution to IWC and contributed approximately half of LWC, where the stratiform portion provided a much larger contribution. Analysis of IWP and LWP fractions suggested that ice precipitation processes played a greater role in northern regions than adjacent southern regions over land. Indications of warm–rain processes were stronger in the maritime and southwest continental regions.

As this study uses “snapshots” of convective events via TRMM satellite overpasses, detailed information regarding life cycle phasing with AEW regime cannot be implied reliably through these data. Unique kinematic and microphysical structures exist as a function of the life cycle of MCSs. Because many MCSs moved faster than AEWs, and therefore interaction with more than one phase of an AEW was possible, aliasing of life cycle characteristics was also possible. Despite this constraint, many useful details have been learned regarding the difference in characteristics of convection as a function of AEW phase and when no wave is present.

The extent of the free tropospheric moisture conditions have been suggested to play an important role in the variability of convection at synoptic scales (e.g. Roca et al. 2005; Lafore et al. 2011). Future work characterizing the changes in thermodynamic and

dynamic environmental structure on a regional scale similar to this study could help to illuminate scale interactions before, when, and after convection is present.

Analysis of the variability involved in the zonal and meridional convective and microphysical characteristics may help to improve West African model simulations and precipitation retrieval algorithms, especially over continental Africa where observations are sparse. Combined observations and simulations of convective systems in the different regions studied here would help the understanding of microphysical processes involved in precipitation production and convective maintenance in each region.

Analysis of the melting layer, where both ice and liquid water exist, is important in understanding convective system mass distribution. This information could help our understanding of feedback mechanisms between spatial scales and intra-storm, allowing greater understanding of WAM processes.

## REFERENCES

- Aspliden, C., Y. Tourre, and J. Sabine, 1976: Some climatological aspects of West African disturbance lines during GATE. *Mon. Wea. Rev.*, **104**, 1029-1035.
- Bain, C. L., D. J. Parker, N. Dixon, A. H. Fink, C. M. Taylor, B. Brooks, S. F. Milton, 2011: Anatomy of an observed African easterly wave in July 2006. *Quart. J. Roy. Meteorol. Soc.*, **137**, 923–933.
- Barnes, G. M., and K. Sieckman, 1984: The environment of fast- and slow-moving tropical mesoscale convective cloud lines. *Mon. Wea. Rev.*, **112**, 1782-1794.
- Barthe, C., N. Asencio, J. Lafore, M. Chong, B. Campistron, and F. Cazenave, 2010: Multi-scale analysis of the 25-27 July 2006 convective period over Niamey: Comparison between Doppler radar observations and simulations. *Quart. J. Roy. Meteor. Soc.*, **136**(S1), 190-208.
- Berry, G. J., C. Thorncroft, and T. Hewson, 2005: Case study of an intense African easterly wave. *Mon. Wea. Rev.*, **133**, 752-766.
- Berry, G., C., Thorncroft, and T. Hewson, 2007: African easterly waves during 2004—Analysis using objective techniques. *Mon. Wea. Rev.*, **135**, 1251-1267.
- Berry, G., 2009: *African Easterly Waves and Convection*, Ph.D. Dissertation, 209 pp. Department of Atmospheric and Environmental Sciences, University at Albany, SUNY: Albany, New York: Albany, New York.
- Bolton, D., 1984: Generation and propagation of African squall lines. *Quart. J. Roy. Meteor. Soc.*, **110**, 695-721.
- Bouniol, D., J. Delanoë, C. Duroure, A. Protat, V. Giraud, and G. Penide, 2010: Microphysical characterisation of West African MCS anvils. *Quart. J. Roy. Meteor. Soc.*, **136**, 323-344.
- Burpee, R. W., 1974: Characteristics of North African easterly waves during the summers of 1968 and 1969. *J. Atmos. Sci.*, **31**, 1556-1570.

- Carey, L. D., and S. A. Rutledge, 2000: The relationship between precipitation and lightning in tropical island convection: A C-band polarimetric radar study. *Mon. Wea. Rev.*, **28**, 2687-2710.
- Carlson, T. N., 1969: Some remarks on African disturbances and their progress over the tropical Atlantic. *Mon. Wea. Rev.*, **97**(10), 716-726.
- Cetrone, J., and R. A. Houze, 2009: Anvil clouds of tropical mesoscale convective systems in monsoon regions. *Quart. J. Roy. Meteor. Soc.*, **135**, 305-317.
- Cetrone, J., and R. A. Houze, 2011: Leading and trailing anvil clouds of West African squall lines. *J. Atmos. Sci.*, **68**, 1114-1123.
- Cifelli, R., S. W. Nesbitt, S. A. Rutledge, W. A. Petersen, and S. Yuter, 2007: Radar Characteristics of precipitation features in the EPIC and TEPPS regions of the East Pacific. *Mon. Wea. Rev.*, **135**, 1576-1595.
- D'Amato, N., and T. Lebel, 1998: On the characteristics of the rainfall events in the Sahel with a view to the analysis of climatic variability. *Int. J. Climatol.*, **18**, 955-974.
- DeLonge, M. S., J. D. Fuentes, S. Chan, P. A. Kucera, E. Joseph, A. T. Gaye, and B. Daouda, 2010: Attributes of mesoscale convective systems at the land-ocean transition in Senegal during NASA African Monsoon Multidisciplinary Analyses 2006. *J. Geophys. Res.*, **115**, 16 PP.
- DeMott, C. A., and S. A. Rutledge, 1998: The vertical structure of TOGA COARE convection. Part I: Radar echo distributions. *J. Atmos. Sci.*, **55**, 2730-2747.
- Diedhiou, A., S. Janicot, A. Viltard, P. de Felice, and H. Laurent, 1999: Easterly wave regimes and associated convection over West Africa and tropical Atlantic: Results from the NCEP/NCAR and ECMWF reanalyses. *Climate Dyn.*, **15**, 795-822.
- Duvel, J. P., 1990: Convection over tropical Africa and the Atlantic Ocean during northern summer. Part II: Modulation by Easterly Waves. *Mon. Wea. Rev.*, **118**, 1855-1868.
- Eldridge, R. H., 1957: A synoptic study of West African disturbance lines. *Quart. J. Roy. Meteor. Soc.*, **84**, 468-469.
- Evaristo, R., G. Scialom, N. Viltard, and Y. Lemaître, 2010: Polarimetric signatures and hydrometeor classification of West African squall lines. *Quart. J. Roy. Meteor. Soc.*, **136**, 272-288.
- Fink, A. H., and A. Reiner, 2003: Spatiotemporal variability of the relation between African easterly waves and West African squall lines in 1998 and 1999. *J. Geophys. Res.*, **108**, 17 PP.

- Fink, A. H., D. G. Vincent, and V. Ermert, 2006: Rainfall types in the West African Sudanian Zone during the Summer Monsoon 2002. *Mon. Wea. Rev.*, **134**, 2143-2164.
- Fortune, M., 1980: Properties of African squall lines inferred from time-lapse satellite imagery. *Mon. Wea. Rev.*, **108**, 153-168.
- Frank, W. M., 1978: The life cycles of GATE convective systems. *J. Atmos. Sci.*, **35**, 1256-1264.
- Fuentes, J. D., B. Geerts, T. Dejene, P. D'Odorico, and E. Joseph, 2008: Vertical attributes of precipitation systems in West Africa and adjacent Atlantic Ocean. *Theor. Appl. Climatol.*, **92**, 181-193.
- Geerts, B., and T. Dejene, 2005: Regional and diurnal variability of the vertical structure of precipitation systems in Africa based on spaceborne radar data. *J. Climate*, **18**, 893-916.
- Gu, G., R. F. Adler, G. J. Huffman, and S. Curtis, 2004: African easterly waves and their association with precipitation. *J. Geophys. Res.*, **109**, 12 PP.
- Guy, N., S. A. Rutledge, and R. Cifelli, 2011: Radar characteristics of continental, coastal and maritime convection observed during AMMA/NAMMA. *Quart. J. Roy. Meteor. Soc.*, **137**, 1241-1256.
- Hamilton, R. A., J. W. Archbold, and C. K. M. Douglas, 1945: Meteorology of Nigeria and adjacent territory. *Quart. J. Roy. Meteor. Soc.*, **71**, 231-264.
- Heymsfield, GM, and Fulton R, 1988: Comparison of high-altitude remote aircraft measurements with the radar structure of an Oklahoma thunderstorm: Implications for precipitation estimation from space. *Mon. Wea. Rev.*, **116**, 1157-1174.
- Hodges, K. I., and C. D. Thorncroft, 1997: Distribution and statistics of African mesoscale convective weather systems based on the ISCCP Meteosat imagery. *Mon. Wea. Rev.* **125**, 2821-2837.
- Houze, R. A., 1977: Structure and dynamics of a tropical squall-line system. *Mon. Wea. Rev.*, **105**, 1540-1567.
- Houze, R. A., and A. K. Betts, 1981: Convection in GATE. *Rev. Geophys.*, **19**, 541-576.
- Houze, R. A., M. I. Biggerstaff, S. A. Rutledge, and B. F. Smull, 1989: Interpretation of Doppler weather radar displays of midlatitude mesoscale convective systems. *Bull. Amer. Meteor. Soc.*, **70**, 608-619.

- Johnson, R. H., S. L. Aves, P. E. Ciesielski, and T. D. Keenan, 2005: Organization of oceanic convection during the onset of the 1998 East Asian Summer Monsoon. *Mon. Wea. Rev.*, **133**, 131-148.
- Kiladis, G. N., C. D. Thorncroft, and N. M. J. Hall, 2006: Three-dimensional structure and dynamics of African easterly waves. Part I: Observations. *J. Atmos. Sci.*, **63**, 2212-2230.
- Kummerow, C., W. Barnes, T. Kozu, J. Shiue, and J. Simpson, 1998: The tropical rainfall measuring mission (TRMM) sensor package. *J. Atmos. Oceanic Technol.*, **15**, 809-817.
- Kummerow, C., J. Simpson, O. Thiele, W. Barnes, A. T. C. Chang, E. Stocker, R. F. Adler, A. Hou, R. Kakar, F. Wentz, P. Ashcroft, T. Kozu, Y. Hong, K. Okamoto, T. Iguchi, H. Kuroiwa, E. Im, Z. Haddad, G. Huffman, B. Ferrier, W. S. Olson, E. Zipser, E. A. Smith, T. T. Wilheit, G. North, T. Krishnamurti, and K. Nakamura, 2000: The status of the tropical rainfall measuring mission (TRMM) after two years in orbit. *J. Appl. Meteor.*, **39**, 1965-1982.
- Lafore, J. -P., J. L. Redelsperger, and G. Jaubert, 1988: Comparison between a three-dimensional simulation and Doppler radar data of a tropical squall line: Transports of mass, momentum, heat, and moisture. *J. Atmos. Sci.*, **45**, 3483-3500.
- Lafore, J. -P., C. Flamant, C. Guichard, D. J. Parker, D. Bouniol, A. H. Fink, V. Giraud, M. Gosset, N. Hall, H. Höller, S. C. Jones, A. Protat, R. Roca, F. Roux, F. Saïd, and C. Thorncroft, 2011: Progress in understanding of weather systems in West Africa. *Quart. J. Roy. Meteor. Soc.*, **12**, 7-12.
- Laing, A. G., R. Carbone, V. Levizzani, and J. Tuttle, 2008: The propagation and diurnal cycles of deep convection in northern tropical Africa. *Quart. J. Roy. Meteor. Soc.*, **134**, 93-109.
- Laurent, H., N. D'Amato, and T. Lebel, 1998: How important is the contribution of the mesoscale convective complexes to the Sahelian rainfall? *Phys. Chem. Earth*, **23**, 629-633.
- Le Barbé, L., and T. Lebel, 1997: Rainfall climatology of the HAPEX-Sahel region during the years 1950-1990. *J. Hydrol.*, **188**, 43-73.
- Leppert, K. D., and W. A. Petersen, 2010: Electrically active hot towers in African easterly waves prior to tropical cyclogenesis. *Mon. Wea. Rev.*, **138**, 663-687.
- Liu, C., E. J. Zipser, D. J. Cecil, S. W. Nesbitt, and S. Sherwood, 2008: A cloud and precipitation feature database from nine years of TRMM observations. *J. Appl. Meteor. Climatol.*, **47**, 2712-2728.

- Lucas, C., E. J. Zipser, and M. A. Lemone, 1994: Vertical velocity in oceanic convection off tropical Australia. *J. Atmos. Sci.*, **51**, 3183-3193.
- Machado, L. A. T., J. Duvel, and M. Desbois, 1993: Diurnal variations and modulation by easterly waves of the size distribution of convective cloud clusters over West Africa and the Atlantic Ocean. *Mon. Wea. Rev.*, **121**, 37-49.
- Mathon, V., H. Laurent, and T. Lebel, 2002: Mesoscale convective system rainfall in the Sahel. *J. Appl. Meteor. Climatol.*, **41**, 1081-1092.
- Mekonnen, A., C. D. Thorncroft, and A. R. Aiyyer, 2006: Analysis of convection and its association with African easterly waves. *J. Climate*, **19**, 5405-5421.
- Mohr, K. I., and E. J. Zipser, 1996: Mesoscale convective systems defined by their 85-GHz ice scattering signature: Size and intensity comparison over Tropical oceans and continents. *Mon. Wea. Rev.*, **124**, 2417-2437.
- Mohr, K. I., and C. D. Thorncroft, 2006: Intense convective systems in West Africa and their relationship to the African easterly jet. *Quart. J. Roy. Meteor. Soc.*, **132**, 163-176.
- Moncrieff, M. W., 1992: Organized convective systems: Archetypal dynamical models, mass and momentum flux theory, and parameterization. *Quart. J. Roy. Meteor. Soc.*, **118**, 819-850.
- Nesbitt, S. W., E. J. Zipser, and D. J. Cecil, 2000: A census of precipitation features in the Tropics using TRMM: Radar, ice scattering, and lightning observations. *J. Climate*, **13**, 4087-4106.
- Nesbitt, S. W., and E. J. Zipser, 2003: The diurnal cycle of rainfall and convective intensity according to three years of TRMM measurements. *J. Climate*, **16**, 1456-1475.
- Nicholls, S. D., and K. I. Mohr, 2010: An analysis of the environments of intense convective systems in West Africa in 2003. *Mon. Wea. Rev.*, **138**, 3721-3739.
- Nitta, T., Y. Nakagomi, Y. Suzuki, N. Hasegawa, and A. Kadokura, 1985: Global analysis of the lower tropospheric disturbances in the tropics during the northern summer of the FGGE year. I. Global features of the disturbances. *J. Meteor. Soc. Japan*, **63**, 1-19.
- Payne, S. W., and M. M. McGarry, 1977: The relationship of satellite inferred convective activity to easterly waves over West Africa and the adjacent ocean during phase III of GATE. *Mon. Wea. Rev.*, **105**, 413-420.

- Penide, G., V. Giraud, D. Bouniol, P. Dubuisson, C. Duroure, A. Protat, and S. Cautenet, 2010: Numerical simulation of the 7 to 9 September 2006 AMMA mesoscale convective system: Evaluation of the dynamics and cloud microphysics using synthetic observations. *Quart. J. Roy. Meteor. Soc.*, **136**, 304-322.
- Petersen, W. A., and S. A. Rutledge, 2001: Regional variability in tropical convection: Observations from TRMM. *J. Climate*, **14**, 3566–3586.
- Petersen, W. A., R. Cifelli, D. J. Bocippio, S. A. Rutledge, and C. Fairall, 2003: Convection and easterly wave structures observed in the Eastern Pacific warm pool during EPIC-2001. *J. Atmos. Sci.*, **60**, 1754-1773.
- Petersen, W. A., and D. J. Bocippio, 2004: ‘Variability of convective structure and lightning activity in tropical easterly waves.’ Preprints, *26<sup>th</sup> Conf. on Hurricanes and Tropical Meteorology*, Miami Beach, FL, Amer. Meteor. Soc., 5B.1.
- Petersen, W. A., H. J. Christian, and S. A. Rutledge, 2005: TRMM observations of the global relationship between ice water content and lightning. *Geophys. Res. Lett.*, **32**, L14819.
- Protat, A., J. Delanoë, A. Plana-Fattori, P. T. May, and E. J. O’Connor, 2010: The statistical properties of tropical ice clouds generated by the West African and Australian monsoons, from ground-based radar–lidar observations. *Quart. J. Roy. Meteor. Soc.*, **136**, 345-363.
- Pytharoulis, I., and C. Thorncroft, 1999: The low-level structure of African easterly waves in 1995. *Mon. Wea. Rev.*, **127**, 2266-2280.
- Redelsperger, J., A. Diongue, A. Diedhiou, J. Ceron, M. Diop, J. Gueremy, and J. Lafore, 2002: Multi-scale description of a Sahelian synoptic weather system representative of the West African monsoon. *Quart. J. Roy. Meteor. Soc.*, **128**, 1229-1257.
- Redelsperger, J., C. D. Thorncroft, A. Diedhiou, T. Lebel, D. J. Parker, and J. Polcher, 2006: African Monsoon Multidisciplinary Analysis: An international research project and field campaign. *Bull. Amer. Meteor. Soc.*, **87**, 1739-1746.
- Reed, R. J., D. C. Norquist, and E. E. Recker, 1977: The structure and properties of African wave disturbances as observed during Phase III of GATE. *Mon. Wea. Rev.*, **105**, 317-333.
- Riemann-Campe, K., K. Fraedrich, and F. Lunkeit, 2009: Global climatology of Convective Available Potential Energy (CAPE) and Convective Inhibition (CIN) in ERA-40 reanalysis. *Atmos. Res.*, **93**, 534-545.

- Roca, R., J. -P. Lafore, C. Piriou, and J. Redelsperger, 2005: Extratropical dry-air intrusions into the West African monsoon midtroposphere: An important factor for the convective activity over the Sahel. *J. Atmos. Sci.*, **62**, 390-407.
- Rowell, D. P., and J. R. Milford, 1993: On the generation of African squall lines. *J. Climate*, **6**, 1181-1193.
- Rutledge, S. A., and R. A. Houze, Jr., 1987: A diagnostic modeling study of the trailing stratiform region of a midlatitude squall line. *J. Atmos. Sci.*, **44**, 2640-2656.
- Sall, S. M., and H. Sauvageot, 2005: Cyclogenesis off the African coast: The case of Cindy in August 1999. *Mon. Wea. Rev.*, **133**, 2803-2813.
- Schumacher, C., and R. A. Houze, 2003: Stratiform rain in the Tropics as seen by the TRMM precipitation radar. *J. Climate*, **16**, 1739-1756.
- Schumacher, C., and R. A. Houze, 2006: Stratiform precipitation production over sub-Saharan Africa and the tropical East Atlantic as observed by TRMM. *Quart. J. Roy. Meteor. Soc.*, **132**, 2235-2255.
- Simmons, A., S. Uppala, D. Dee, and S. Kobayashi, 2007: *ERA-Interim: New ECMWF reanalysis products from 1989 onwards*. ECMWF.
- Sommeria, G., and J. Testud, 1984: COPT 81: A field experiment designed for the study of dynamics and electrical activity of deep convection in continental tropical regions. *Bull. Amer. Meteor. Soc.*, **65**, 4-10.
- Tao, W. -K., S. Lang, J. Simpson, and R. Adler, 1993: Retrieval algorithms for estimating the vertical profiles of latent heat release: Their applications for TRMM. *J. Meteor. Soc. Japan*, **71**, 685-700.
- Tao, W. -K., S. Lang, X. Zeng, S. Shige, and Y. Takayabu, 2010: Relating convective and stratiform rain to latent heating. *J. Climate*, **23**, 1874-1893.
- Thorncroft, C., and K. Hodges, 2001: African easterly wave variability and its relationship to Atlantic tropical cyclone activity. *J. Climate*, **14**, 1166-1179.
- Thorncroft, C. D., N. M. J. Hal, and G. N. Kiladis, 2008: Three-dimensional structure and dynamics of African easterly waves. Part III: Genesis. *J. Atmos. Sci.*, **65**, 3596-3607.
- Tokay, A., and D. A. Short, 1996: Evidence from tropical raindrop spectra of the origin of rain from stratiform versus convective clouds. *J. Appl. Meteor.*, **35**, 355-371.

- Tokay, A., A. Kruger, W. F. Krajewski, P. A. Kucera, and A. J. P. Filho, 2002: Measurements of drop size distribution in the southwestern Amazon basin. *J. Geophys. Res.*, **107**, 15 PP.
- Toracinta, E. R., D. J. Cecil, E. J. Zipser, and S. W. Nesbitt, 2002: Radar, passive microwave, and lightning characteristics of precipitating systems in the Tropics. *Mon. Wea. Rev.*, **130**, 802-824.
- Xu, W., E. J. Zipser, and C. Liu, 2009: Rainfall characteristics and convective properties of Mei-Yu precipitation systems over South China, Taiwan, and the South China Sea. Part I: TRMM observations. *Mon. Wea. Rev.*, **137**, 4261-4275.
- Xu, W., E. J. Zipser, C. Liu, and H. Jiang, 2010: On the relationships between lightning frequency and thundercloud parameters of regional precipitation systems. *J. Geophys. Res.*, **115**, D12203.
- You, Y., G. Liu, Y. Wang, and J. Cao, 2011: On the sensitivity of Tropical Rainfall Measuring Mission (TRMM) Microwave Imager channels to overland rainfall. *J. Geophys. Res.*, **116**, D12203.
- Zipser, E. J., 1969: The role of organized unsaturated convective downdrafts in the structure and rapid decay of an equatorial disturbance. *J. Appl. Meteor.*, **8**, 799-814.
- Zipser, E. J., and M. A. LeMone, 1980: Cumulonimbus vertical velocity events in GATE. Part II: Synthesis and model core structure. *J. Atmos. Sci.*, **37**, 2458-2469.
- Zipser, E. J., C. Liu, D. J. Cecil, S. W. Nesbitt, and D. P. Yorty, 2006: Where are the most intense thunderstorms on earth? *Bull. Amer. Meteor. Soc.*, **87**, 1057-1071.

**PART IV: GODDARD CUMULUS ENSEMBLE MODEL PERFORMANCE ON  
SAHELIAN MESOSCALE CONVECTIVE SYSTEMS**

## CHAPTER 1

### INTRODUCTION

During the West African monsoon (June–September) mesoscale convective systems (MCSs) provide the majority of precipitation in West Africa (Le Barbé and Lebel 1997; D’Amato and Lebel 1998; Laurent et al. 1998; Mathon et al. 2002; Redelsperger et al. 2002; Fink et al. 2006), often taking the form of squall lines (Hamilton et al. 1945; Eldridge 1957; Bolton 1984; Houze et al. 1989), a highly organized system that primarily exhibits a leading convective line with cirriform anvil preceding and extensive trailing, precipitating stratiform cloud. Two–way interactions with the major synoptic feature, African easterly waves (AEWs), have been shown. Modulation of the evolution (Payne and McGarry 1977; Machado et al. 1993) and generation (Fink et al. 2006) of MCSs may occur in the presences of AEWs, along with the modification of the large–scale environment through moisture (Lafore et al. 1988) and momentum (Moncrieff 1992) transport or reinforcement of cyclonic rotation (Barthe et al. 2010).

A few studies note the existence of MCSs with no association to AEWs (Fink et al. 2006; Laing et al. 2008). Analysis of ground–based radar data at continental, coastal, and maritime locations revealed that regional differences in convective characteristics were more apparent than differences between AEW and no–wave events (Guy et al.

2011); however, system structure and duration exhibited variations according to synoptic dynamic and local thermodynamic forcing. A climatological analysis using 13 years of TRMM data (precipitation radar and microwave) showed differences in stratiform fractions, microphysics, and ice and liquid water mass when subdivided by AEW phase and when no wave was present (Guy and Rutledge 2012).

Numerical weather prediction models have historically performed poorly in representing characteristics of the West African monsoon (WAM); see Ruti et al. (2011) for an overview of key results to date. Recent studies have indicated improved forecasts and simulations were obtained with the ingestion of additional observational data (Tompkins et al. 2005; Faccani et al. 2009; Agustí-Panareda et al. 2010), though the impact of the additional information disappeared within one day (Agustí-Panareda et al. 2010). Despite better intraseasonal representations of AEWs in the latest generation of global climate models (GCMs), challenges still exist to understand the mechanisms driving the discrepancies (Ruti et al. 2011). Even with improvements to the representation of AEWs and other synoptic features, shorter time scale (smaller spatial scale) variability (e.g. precipitation) is less reproducible in simulations (e.g. Vanvyve et al. 2008).

Multi-scale model frameworks, such as the Goddard finite volume model (Tao et al. 2009) rely upon embedded cloud-resolving models (CRMs) to simulate convective events within and between grid points. A CRM employing an ensemble approach, such as that used in the Goddard Cumulus Ensemble (GCE) model (Tao and Simpson 1993; Tao et al. 2003) allows the development of clouds at multiple vertical levels. This is accomplished by representing convection as a statistical occurrence of cloud and

precipitation properties. These CRMs may also be used in a stand-alone respect in order to study specific events (see Tao (2007) for an overview of CRMs and their uses).

Previous research in West Africa has focused primarily on large-scale features and precipitation. Case studies have been undertaken to illuminate mesoscale and synoptic processes (e.g. Penide et al. 2010; Schwendike and Jones 2010), though little work has been done to explore the degree to which convective characteristics are represented in CRMs in West Africa. It is unclear if convective events produced by CRMs embedded in GCMs accurately represent differences observed in convective characteristics during the WAM season.

The grid spacing employed here corresponds to state-of-the-art GCMs which are now utilizing grid spacings down to 1 km. This study explores the representation of convective characteristics by a CRM used by the Goddard finite volume GCM system. Two distinct events during the 2006 WAM in the Sahel region are simulated using the GCE model: one associated with an AEW trough (8 September 2006) and another with no AEW influence (14 July 2006). Results discuss the performance of the CRM microphysical and parameterization packages in application to intense, tropical convection. This study establishes model performance of the GCE following recent updates in parameterization schemes that improve ice microphysics representation.

## CHAPTER 2

### SIMULATION SETUP

The CRM used to simulate MCSs that occurred when an AEW was present (8 September 2006) and when no AEW was present (14 July 2006) in this study was a 3D version of the GCE model. Model setup was extensively described in Zeng et al. (2009, 2011), though a parameterization to increase ice crystal concentrations as a function of latitude was employed to better represent West African MCSs (Powell et al. 2011; Tao et al. 2011). Briefly, the equations used were non-hydrostatic and anelastic. The GCE accounted for both solar radiation absorption and scattering, and infrared radiation emission and absorption. Turbulent processes (sub-gridscale) were parameterized based upon Klemp and Wilhelmson (1978) and Soong and Ogura (1980) schemes, with both dry and moist processes used in the generation of sub-gridscale kinetic energy.

A one-moment, three-category ice (cloud ice, snow, graupel) scheme (Rutledge and Hobbs 1984) with modified cloud microphysics (Lang et al. 2007; Zeng et al. 2008), along with two water categories (cloud and rain water) was used. Prognostic hydrometeor variables (expressed as mixing ratios) were produced for each category. Cloud ice and snow were represented by small ( $< 50 \mu\text{m}$ ) and large ( $\geq 50 \mu\text{m}$ ) diameter crystals. Different densities were used for graupel ( $0.4 \text{ g cm}^{-3}$ ) and snow ( $0.1 \text{ g cm}^{-3}$ ). Convective and stratiform partitioning was performed using the GCE method described

in (Lang et al. 2003), which showed that resultant reflectivity statistics were comparable to statistics created from various simulation and observational partitioning techniques.

Simulations were performed using 1024 x 1024 x 63 grid points with 1 km horizontal spacing and stretched vertical spacing ranging from 42.5 m near the surface to 1 km at the top. Large-scale forcing was employed to drive simulations, provided by a quadrilateral rawinsonde network that was part of the African Monsoon Multidisciplinary Analyses (AMMA; Redelsperger et al. 2006; Lebel et al. 2010) field campaign (see Fig. 2.1 for simulation domain, further discussion in Chapter 3). To ensure that the large-scale forcing was responsible for heat, moisture, and momentum within the simulation domain, cyclic boundary conditions were used. The domain size was chosen to encompass the forcing network data and provide a large enough area to represent the MCSs. Simulation vertical data were degraded to 1 km spacing to match observational data discussed in Chapter 3.

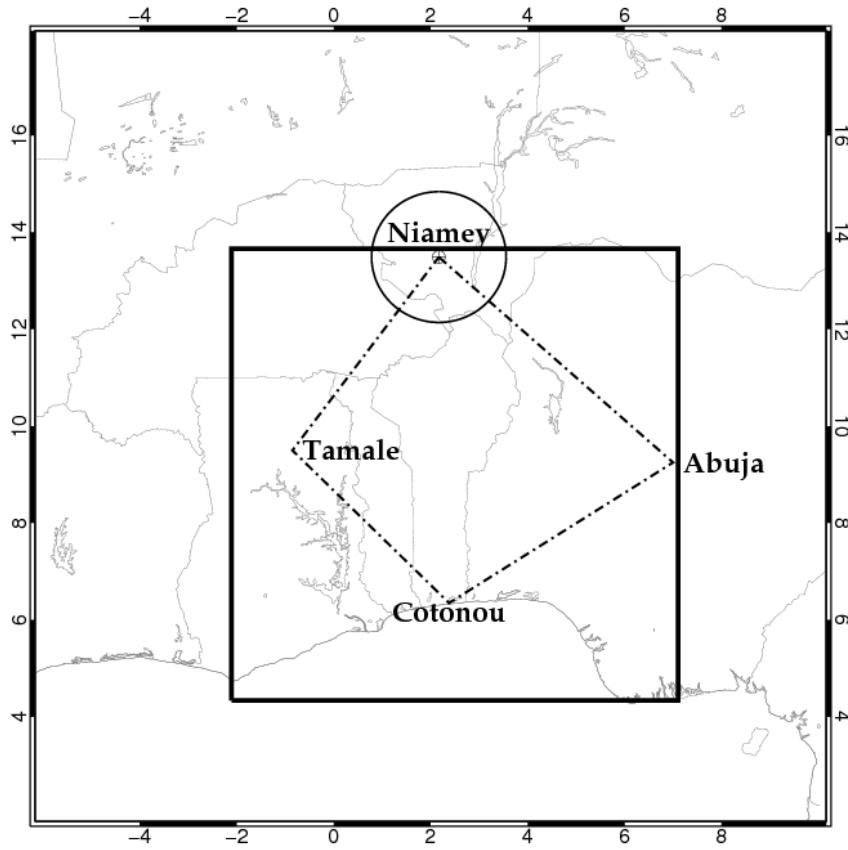


Fig. 2.1. Map of the simulated region (solid-lined box) in West Africa. The sounding domain (dash-dot lines) used to calculate the large-scale forcing data for the simulations is shown, with radiosonde sites labeled. The circle indicates the 150 km radius MIT ground-radar observed domain.

## CHAPTER 3

### OBSERVATIONAL DATA

Reflectivity and Doppler velocity data were collected with the C-band, single polarization Massachusetts Institute of Technology (MIT) Doppler radar and vertically-pointing W-band Atmospheric Radiation Measurement (ARM) program Cloud Radar (WACR; Miller and Slingo 2007; Slingo et al. 2008) located in Niamey, Niger (13.49°N, 2.17°E) during the 2006 AMMA experiment. The MIT radar was operated from 5 July – 27 September acquiring both 360° volume plan position indicator (PPI) and range height indicator (RHI) scans (when convection was present) during a 10-minute repeat cycle [see Guy et al. (2011) for further details]. The WACR radar was operated throughout the AMMA experiment, acquiring semi-continuous observations with approximately 45 m vertical and 2.5 s temporal sampling. Detectable signal thresholding as a function of height was applied as in Penide et al. (2010). While WACR observations for the 8 September case covered the entire observed time period of the system near Niamey, only the forward anvil was sampled during the 14 July case. Cloud radar data were degraded to 1 km spacing to match the MIT radar Cartesian grid data discussed below.

Scanning radar polar coordinate data were interpolated to a 1 km vertical and horizontal resolution Cartesian grid using the National Center for Atmospheric Research REORDER software (Mohr et al. 1986), corresponding to the GCE simulation output

horizontal grid spacing. Radar reflectivity ( $Z$ ) volume scans were partitioned into convective and stratiform components using the Steiner et al. (1995) algorithm, which uses a convective threshold value (40 dBZ) to identify convective cores, along with a convective peakedness criterion which evaluates surrounding pixels for convective classification. Further details regarding MIT radar data and processing can be found in Guy et al. (2011).

Ground-based radar observations were used as the primary data source for comparison to GCE simulations. Rainfall ( $R$ ) estimates were obtained using separate convective and stratiform  $Z$ - $R$  power-based relationships from Russell et al. (2010) for each case, where  $Z$  is in  $\text{mm}^6 \text{m}^{-3}$  and  $R$  in  $\text{mm h}^{-1}$ . The 8 September case used  $Z = 143R^{1.36}$  (convective) and  $Z = 256R^{1.22}$  (stratiform), while  $Z = 186R^{1.35}$  (convective) and  $Z = 299R^{1.46}$  (stratiform) were applied for the 14 July case.

Ice and liquid water mass were calculated using three-dimensional reflectivity data, following a modified methodology of Petersen et al. (2005). Ice water content (IWC, from the  $-5^\circ\text{C}$  level to echo top) was calculated for each grid point using an exponential size (mass,  $M$ ) distribution in the form of an  $M$ - $Z$  relationship (Carey and Rutledge 2000):

$$IWC = 1000\pi\rho_i N_0^{3/7} \left( \frac{5.28 \times 10^{-18}}{720} Z \right)^{4/7} \quad (\text{g m}^{-3}), \quad (3.1)$$

where IWC is mass per volume,  $Z$  is in  $\text{mm}^6 \text{m}^{-3}$ ,  $N_0$  is the constant intercept parameter ( $4 \times 10^6 \text{m}^{-4}$ ), and bulk ice density ( $\rho_i$ ) varies between 100 and  $800 \text{g m}^{-3}$  as a function of  $Z$  and precipitation type (stratiform or convective). Similarly liquid water content (LWC;

from near surface to the 0°C level) was calculated using the relationship from Tokay et al. (2002):

$$LWC = 3.5 \times 10^{-3} Z^{0.536} \text{ (g m}^{-3}\text{)}. \quad (3.2)$$

Temperature (T) data from the Niamey sounding site were used to find the 0°C and –5°C levels. To approximate the IWC of the associated anvil cloud, WACR radar data were employed using the M–Z–T relationship for 95–GHz observations in the Tropics given by Eq. 16 in Protat et al. (2007):

$$\log_{10}(IWC) = 4.57 \times 10^{-4} Z_{dB} T + 9.69 \times 10^{-2} Z_{dB} - 2 \times 10^{-4} T - 0.61 \text{ (g m}^{-3}\text{)}, \quad (3.3)$$

where  $Z_{dB}$  is in decibel units and T is in °C. All IWC and LWC calculations are approximate as a number of assumptions were used to develop the relationships. Because this study will focus on comparing the relative trends and not absolute magnitudes between simulations and observations, any errors in relationships should not impact study results. Integrating IWC and LWC vertically yields ice (IWP) and liquid water path (LWP), respectively.

Hydrometeor identification (HID) is normally derived from dual–polarimetric radar data, which uses information from vertically and horizontally polarized signals to estimate hydrometeor species. Some alternative techniques utilizing horizontal polarization data only have been developed. Lerach et al. (2010) developed a method to perform HID analyses using reflectivity and environmental temperature data only. In their study, an HID analysis using a fuzzy logic–based method (Liu and Chandrasekar 2000) was applied to reflectivity observations from an S–band profiler. The methodology was verified using dual–polarization data obtained by the NCAR S–polKa radar which was operating near the profiler. This information was then employed to tune

a lookup table method in which HID analysis was a function of only reflectivity and environmental temperature data. This methodology was applied to MIT radar reflectivity and sounding data to produce a three-dimensional volume HID analysis.

The radar brightband (a layer in which descending aggregates of ice particles begin to melt and form an outer sheath of liquid water, which results in enhanced reflectivity returns due to differences in the dielectric constant between ice and water) can often corrupt HID analysis. In the original methodology of Lerach et al. (2010), vertical velocity measurements from were used to detect the brightband layer and consequently removed with a linear interpolation of reflectivity data from above and below the layer. Because the MIT radar was not vertically pointing, Doppler velocity information in the vertical was not directly available and therefore an alternative brightband detection algorithm was employed.

In this study the following brightband layer detection was used. The 0°C isotherm was found from the nearest environmental sounding for points identified as stratiform by the convective-stratiform separation algorithm. The brightband was assumed to extend below this level by 300 m. The top boundary was identified through analysis of the vertical gradient of reflectivity (Fabry and Zawadzki 1995), which required a decrease between 5–10 dBZ km<sup>-1</sup>. Finally, 62.5% of surrounding points (5 of 8 neighboring points in the horizontal) must be identified as stratiform, which helped to alleviate spurious results in the proximity of a convective core, yet not fully exclude smaller brightband regions. Though these brightband-identified regions should be nearly equivalent to the wet snow category, an additional category of melting ice was introduced to indicate the unique identification and determine the performance of the algorithm.

Specific temperature and reflectivity criteria can be found in Fig. 4 in Lerach et al. (2010). Categories identified by the algorithm were drizzle, rain, dry and wet snow, dry and wet graupel, hail, melting ice, and unclassified (no classification criteria met).

The GCE variables represented instantaneous values at each hour. Radar observations, initially in 10-minute time steps, were degraded to one-hourly temporal resolution to match the GCE data. The closest radar volume time step was chosen, as long as these occurred within 15 minutes of the GCE time step.

Six-hourly (0, 6, 12, 18 UTC) radiosonde data was collected in Niamey during the operational period of the MIT radar. Thermodynamic parameters were calculated using sounding data to characterize the environment before, during, and after the time period of the cases. Pseudoadiabatic parcel ascent from a mixed layer (bottom 50 hPa of sounding) was used in convective available potential energy (CAPE) and convective inhibition CIN calculations. Low-level shear (surface to low-level maximum zonal wind) was calculated as in (Lucas et al. 2000).

The sounding network (Agustí-Panareda et al. 2010) shown in Fig. 2.1 used to calculate large-scale forcing included the aforementioned Niamey station, along with radiosonde sites at Tamale, Ghana (9.50°N, 0.85°E), Cotonou, Benin (6.35°N, 2.38°E), and Abuja, Nigeria (9.25°N, 7.00°E). Domain averaged large-scale forcing (e.g. zonal, meridional, and vertical motion vectors) and apparent heat source and moisture sink (Johnson and Ciesielski 2000) was computed using the quadrilateral network, though only the large-scale forcing was used in this study.

## CHAPTER 4

### SYNOPTIC AND MESOSCALE DESCRIPTION

#### *4.1. 8 September 2006 case*

As documented by Penide et al. (2010), a highly organized squall line MCS (SLMCS; with extensive cloud shield of ~600 km diameter in IR imagery) approached Niamey from the southeast and was sampled by the MIT radar on 8 September at 0200 UTC. This SLMCS was associated with an AEW that was generated near or eastward of 20°E (Janicot et al. 2008; Schwendike and Jones 2010; Zawislak and Zipser 2010) and later was responsible for the genesis of Hurricane Helene in the Atlantic. Analysis of infrared (IR) brightness temperature maps over West Africa (not shown) revealed that the associated MCS was generated 7 September at 0430 UTC near 11.5°E and moved westward until dissipating in Burkina Faso (~200 km west of Niamey) at approximately 1200 UTC. The AEJ was located north of Niamey (Fig. 4.1), with a northwest-to-southeast oriented AEW trough axis (with a speed of  $6.5 \text{ m s}^{-1}$ ) situated to the north and east of the study domain. The SLMCS was ahead to within the trough near Niamey, with a small northerly component evident in the 700 hPa wind field.

Radar data showed two distinct convective lines formed the SLMCS, which began to decay near and within the radar domain. The initial convective line observed moved southeast to northwest with an average speed of  $10.5 \text{ m s}^{-1}$  and reached the radar location

at 0551 UTC where it became quasi-stationary for approximately one hour. A westward propagating secondary convective line, with a speed of  $14.8 \text{ m s}^{-1}$ , approached the MIT radar before decaying and becoming less organized. This second surge resulted in the system passing directly over the radar at 0701 UTC and maintained an estimated average system speed of  $13 \text{ m s}^{-1}$  while in the observed radar domain. Plane view and vertical cross-sections (Fig. 4.2) clearly showed a leading convective line structure with prominent front and rear stratiform anvils and the performance of the HID algorithm. The distribution of HID categories was similar to those shown in Evaristo et al. (2010), which used dual-polarimetric information of a squall line sampled in Benin.

Time series of environmental properties (Fig. 4.3) revealed extremely large values of CAPE (Fig. 4.3a) at the Niamey sounding site in excess of  $6000 \text{ J kg}^{-1}$  preceded the system, and remained near  $3500 \text{ J kg}^{-1}$  when the SLMCS entered the radar observational domain (0201 UTC). Westerlies up to 800 hPa were overlaid by deep easterlies until about 1800 UTC on 7 September (Fig. 4.3b), providing moderate low-level vertical wind shear ( $2.5 \times 10^{-3} \text{ s}^{-1}$  easterly; Fig. 4.3c). Figure 4.3d revealed large positive equivalent potential temperature ( $\theta_e$ ) anomalies leading up to convection entering the MIT radar domain, consistent with the extreme buildup of CAPE (Parker 2002). A positive anomaly in the 800–500 hPa layer, as well as cold  $\theta_e$  low-level anomalies following MCS passage was indicative of the vertical moisture transport (Scialom and Lemaître 2011) and downdraft drying and evaporative cooling observed in this region (Parker et al. 2005), respectively. These characteristics follow the intense convective category of Nicholls and Mohr (2010), except for the shear, which is weaker than reported in their study ( $4.4 \times 10^{-3} \text{ s}^{-1}$  easterly; their Table 3).

#### 4.2. 14 July 2006 case

In contrast to the 8 September case, the 14 July SLMCS was not associated with an AEW event. An AEW trough was located more than  $7^\circ$  west of Niamey, with the AEW to the south and nearly zonal easterly flow at 700 hPa (Fig. 4.4). Smaller areal coverage of the system was observed ( $\sim 400$  km in diameter via IR imagery) due to a smaller stratiform area. Two distinct westward-propagating MCSs, arriving in the Niamey region simultaneously (0211 UTC), were observed in radar imagery (not shown). A similar life cycle to the 8 September case was observed.

The northern SLMCS (a well-developed bow echo moving westward at a speed of  $20 \text{ m s}^{-1}$ ) was generated near  $7^\circ\text{E}$  on 13 July at 1630 UTC, while the southern MCS (northwestward movement at  $13 \text{ m s}^{-1}$ ) was generated near  $5^\circ\text{E}$  on 13 July at 2230 UTC. The two MCSs merged over the radar location at 0511 UTC, at which time the system began to disorganize and became less linear in nature, moving westward at an average speed of  $17 \text{ m s}^{-1}$ . Dissipation again occurred in Burkina Faso, apparently generating two new MCSs afterward. Horizontal and vertical structure of the system (as seen in Fig. 4.5) revealed differences in comparison to the 8 September case. A shorter life span was observed in the radar domain, resulting in different temporal characteristics. This is discussed further in Chapter 5.

Moderate CAPE ( $\sim 1500 \text{ J kg}^{-1}$ ) and very little CIN ( $\sim 100 \text{ J kg}^{-1}$ ; Fig. 4.6a) values characterized the environment before the arrival of the MCSs. A moist mixed-layer ( $\sim 15 \text{ g kg}^{-1}$ ; not shown), along with strong low-level vertical wind shear ( $5\text{--}20 \times 10^{-3} \text{ s}^{-1}$  easterly shear; Fig. 4.6c) provided a favorable environment for organized convection. Bowing curvature evidenced a strong rear-inflow jet associated with the system.

Analysis of IR imagery loops (not shown) indicated that both systems were in a mature life cycle phase when entering the radar domain, and both systems decayed in the western region of the radar domain. Similar life cycle phase and system morphology allowed direct comparison of the two events, though size difference (greater horizontal coverage of the 8 September case) and temporal extent within the radar domain (8 and 11 hours for the 14 July and 8 September cases, respectively) should be noted.

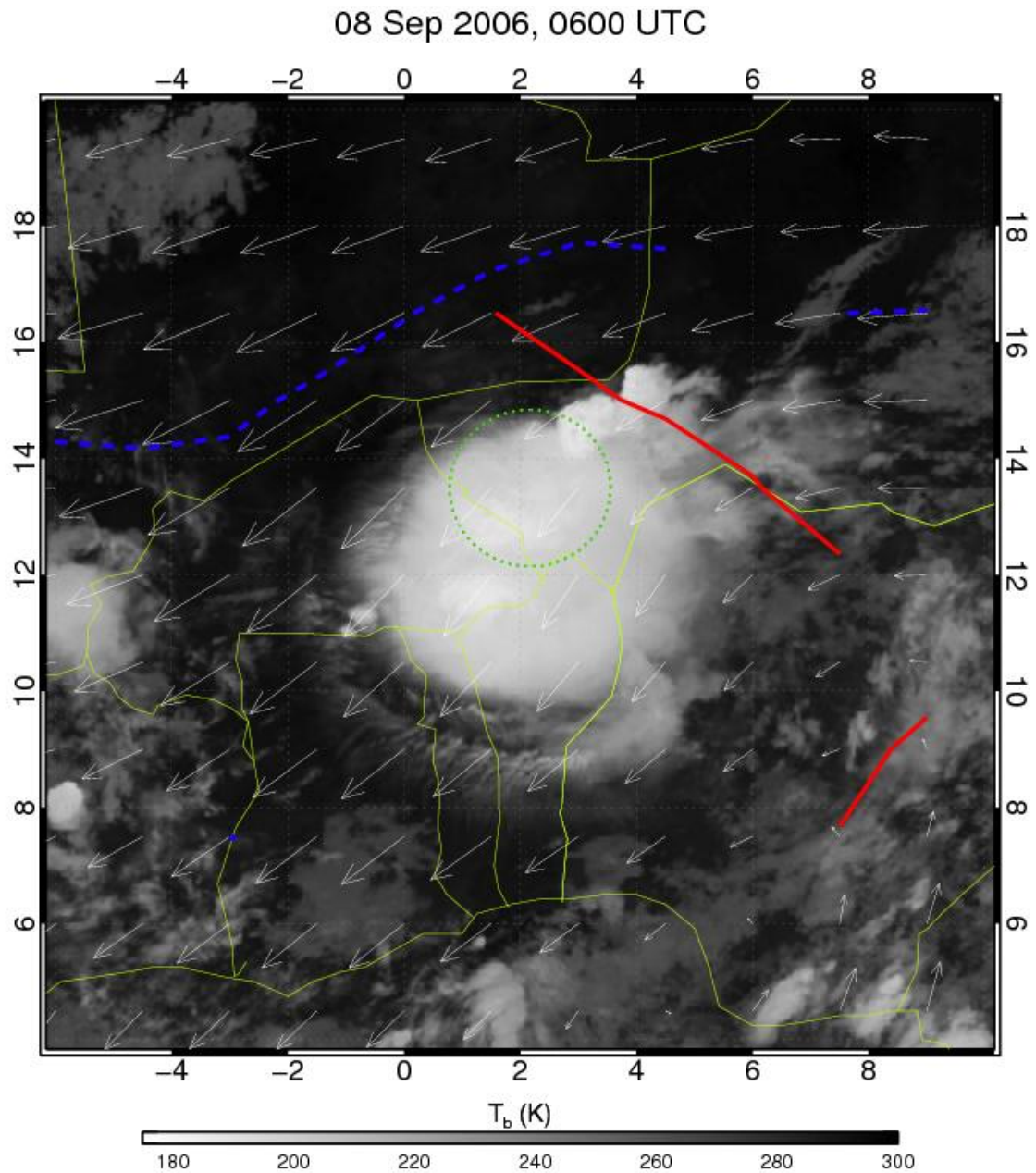


Fig. 4.1. Observed infrared brightness temperatures at 0600 UTC on 8 September 2006. Objectively identified African easterly wave trough axis (red solid line) and African easterly jet axis (blue dashed line) are shown along with 700 hPa wind vectors (arrows).

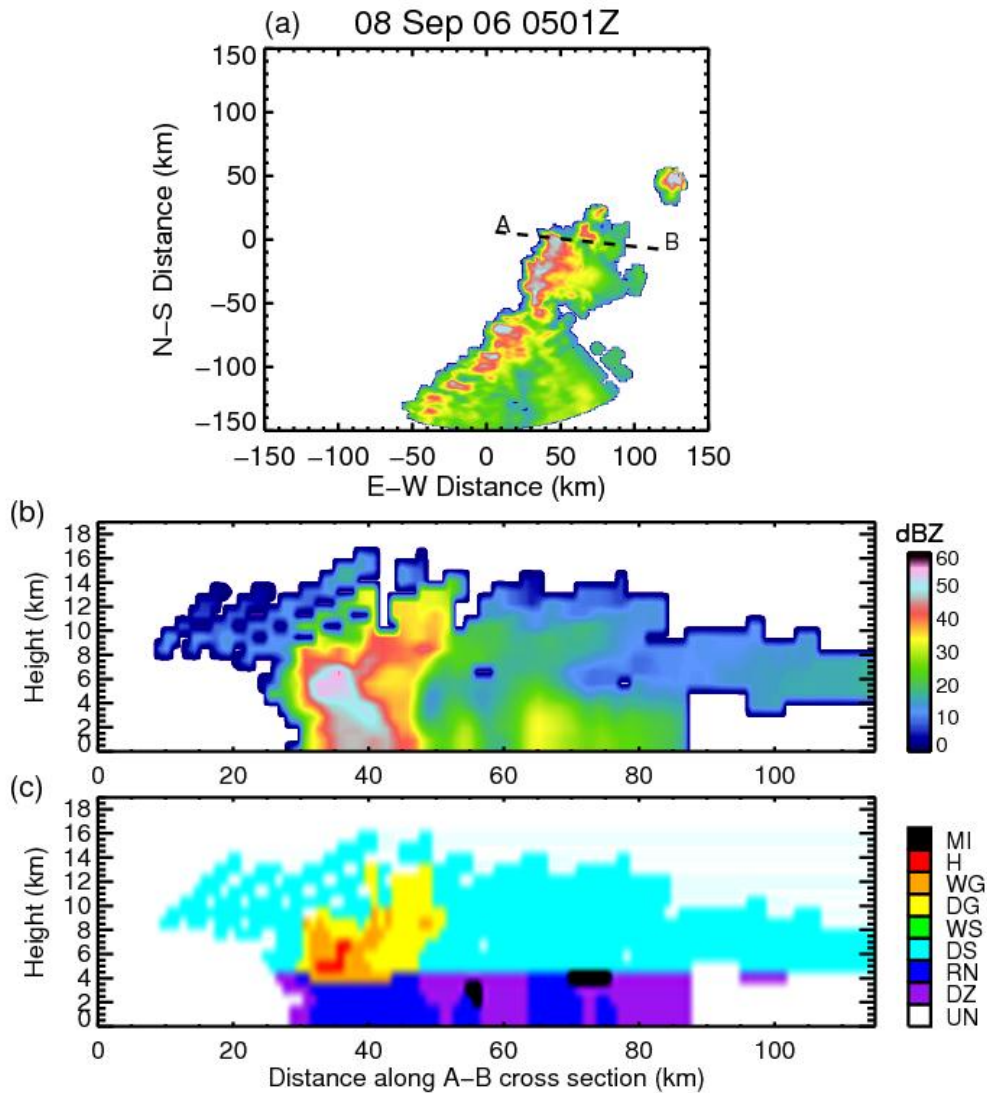


Fig. 4.2. An example of MIT radar reflectivity (a) 2 km CAPPI at 0501 UTC on 8 September 2006. Vertical structure of the squall line mesoscale convective system is indicated by a cross-section of (b) reflectivity, and (c) HID analysis results. Distances in (a) are relative to radar location and the dashed, black A-B line represents cross-sections displayed in (b) and (c). Hydrometeors identified in (c) are melting ice (MI), hail (H), wet graupel (WG), dry graupel (DG), wet snow (WS), and dry snow (DS), rain (RN), drizzle (DZ), and unclassified (UN).

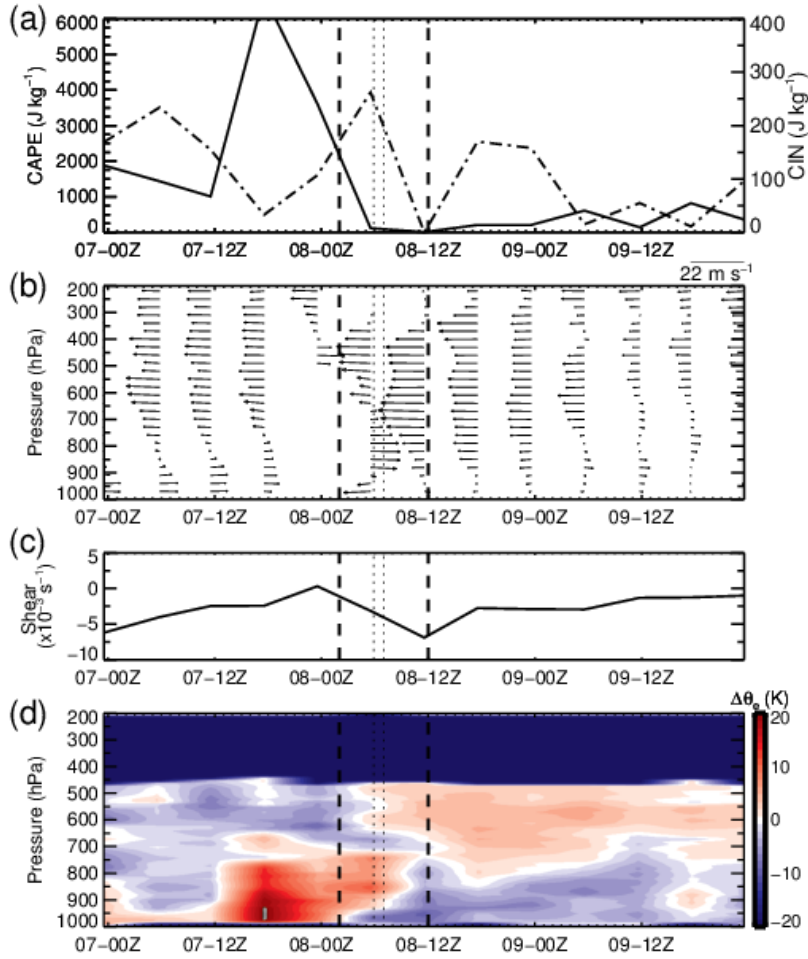


Fig. 4.3. Time series of a) CAPE (solid line) and CIN (dash-dot line), b) wind magnitude and direction (toward arrow head), c) low-level vertical wind shear, and d) equivalent potential temperature anomaly for the 8 September 2006 case. Heavy vertical, dashed lines represent the time period corresponding to ground-based radar observations in Niamey, Niger. Thin, dotted lines show the times when MCS was directly over the radar. The abscissa axis format is day-UTC time.

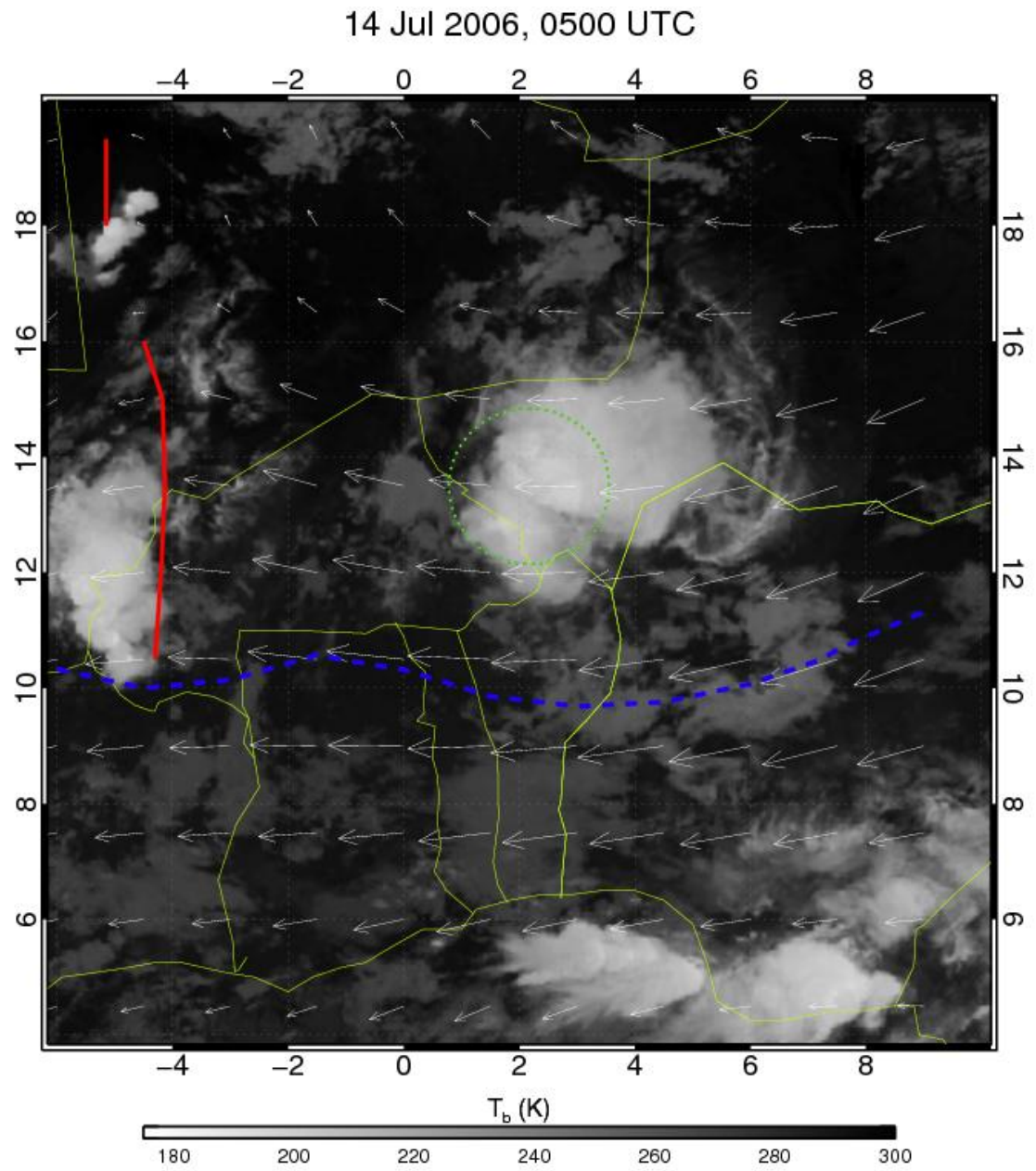


Fig. 4.4. As in Fig. 4.1, except for 0500 UTC on 14 July 2006.

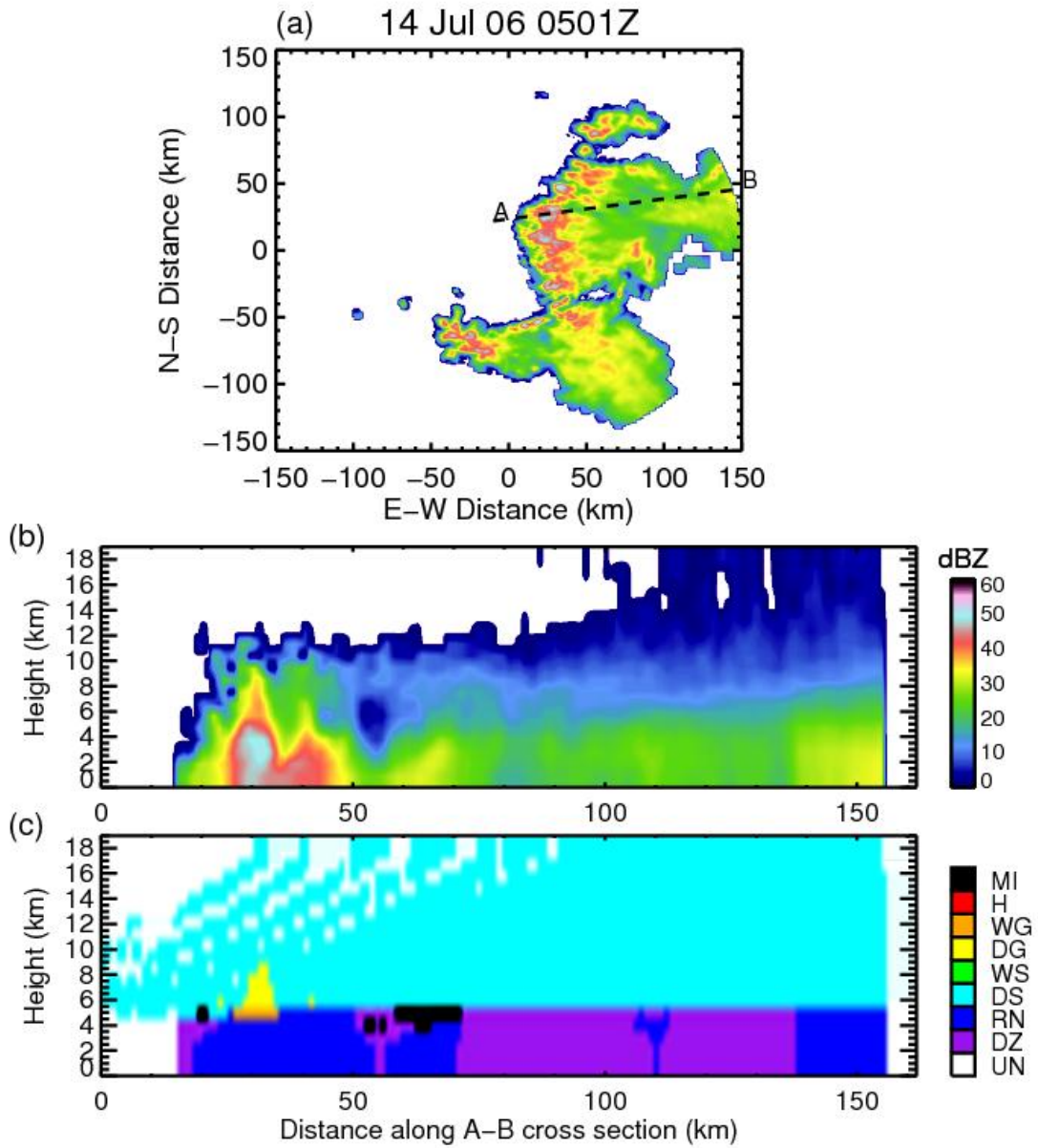


Fig. 4.5. As in Fig. 4.2, except for 0501 UTC on 14 July 2006. Note that some beam filling issues were present at upper levels at distances greater than 100 km.

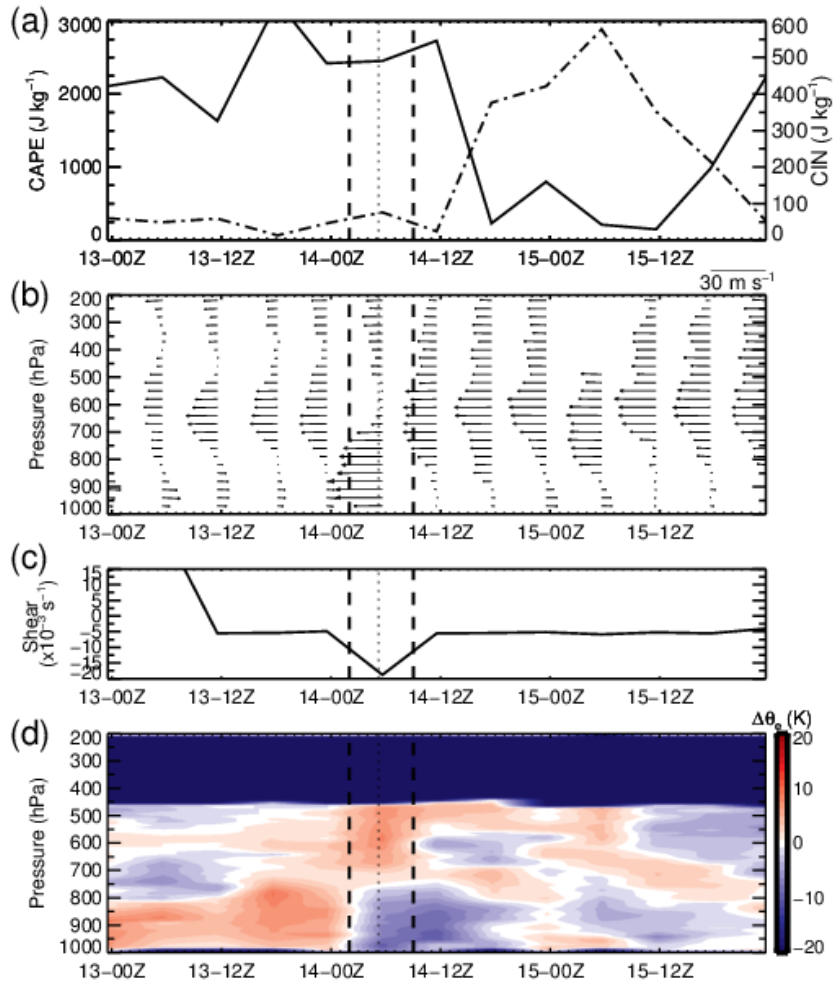


Fig. 4.6. As in Fig. 4.3, except for the 14 July 2006 case.

## CHAPTER 5

### OBSERVATIONAL DISCUSSION

Time series presented in Fig. 5.1 indicated the temporal evolution of characteristics of both cases using MIT radar data. Analysis of volumetric rain (Fig. 5.1a; total rain rates normalized by echo area) indicated the importance of both the convective and stratiform components in both cases. Larger values represent either an increased rain rate and/or decreased area, essentially normalizing precipitation by precipitating area. During the 8 September case, precipitation was dominated by the convective component during the first half of observations. During the second half, stratiform precipitation contributed slightly more total rain. Stratiform precipitation contributed less in the 14 July case, where only the last two hours showed slightly greater precipitation from the stratiform component. The secondary peak noticeable in each case resulted from secondary convective lines previously discussed.

Strong updrafts result in increased lofting of hydrometeors, so consequently the vertical structure of radar reflectivity is useful for studying convective strength. The maximum height of the 30-dBZ echo (30ETH; DeMott and Rutledge 1998) is a common intensity metric. Figure 5.1b showed higher 30ETH values for the 8 September case, with a peak near 19 km, while only about 15 km for the 14 July case. Heights decreased throughout the observed time periods. The existence of 30ETH well above the

environmental freezing level indicates the presence of mixed-phase processes accompanied by significant lightning. Peaks in frequent lightning flashes (not shown) coincided with maximum convective activity. Additionally, 0ETHs indicated stratiform shields at high altitudes; with the 14 July case extending to the top of the analysis domain. Lower 30ETHs associated with the second convective portion suggested that updrafts were weaker in the second convective portion than the first with a likely reduction in mixed-phase particle production (also indicated by a decrease in lightning flashes).

Decreased lofting of hydrometeors also affects ice production as evidenced by the evolution of IWP (Fig. 5.1c) and LWP (Fig. 5.1d). Trends were similar to volumetric rain, not surprising given both were a function of radar reflectivity (see Chapter 3). The double peaks of the stratiform IWP and LWP in the 8 September case lagged the convective portion by one to three hours, with a slight difference in slope. A single peak was observed during the 14 July case. During increased convective periods, ice particle transport occurs from convective cores into the stratiform region. These ice particles then fall out of the stratiform region resulting in higher water contents. This was manifested as an increasing separation of the IWP and LWP curves following each convective activity peak.

Analysis of IWC and LWC showed varying vertical structure between the cases, despite similar IWP and LWP magnitude and trends. Time-height plots in Fig. 5.2a showed increased mean IWC (contoured), followed by increased mean LWC (shaded) for the 8 September case, in agreement with the discussion above. The more vigorous convection associated with the initial convective line was evident in maximum

distributions (Fig. 5.2b). The distribution in Fig. 5.2 indicated that maximum values did not necessarily follow mean distributions and were dependent upon convective morphology and intensity of individual features. Mean IWC evolution (Fig. 5.3a) appeared more homogeneous for the 14 July case, though mean LWC (Fig. 5.3a) was similar. Contours of high IWC resided at lower heights than the AEW case, while lower value contours remained at consistent heights, indicating a different distribution of ice mass throughout the entire no-wave MCS case. Time series plots of HID types confirm that graupel distributions were confined to lower altitudes as well as a consistently deeper (and more temporally homogeneous) identification of snow (shown later) in the 14 July case.

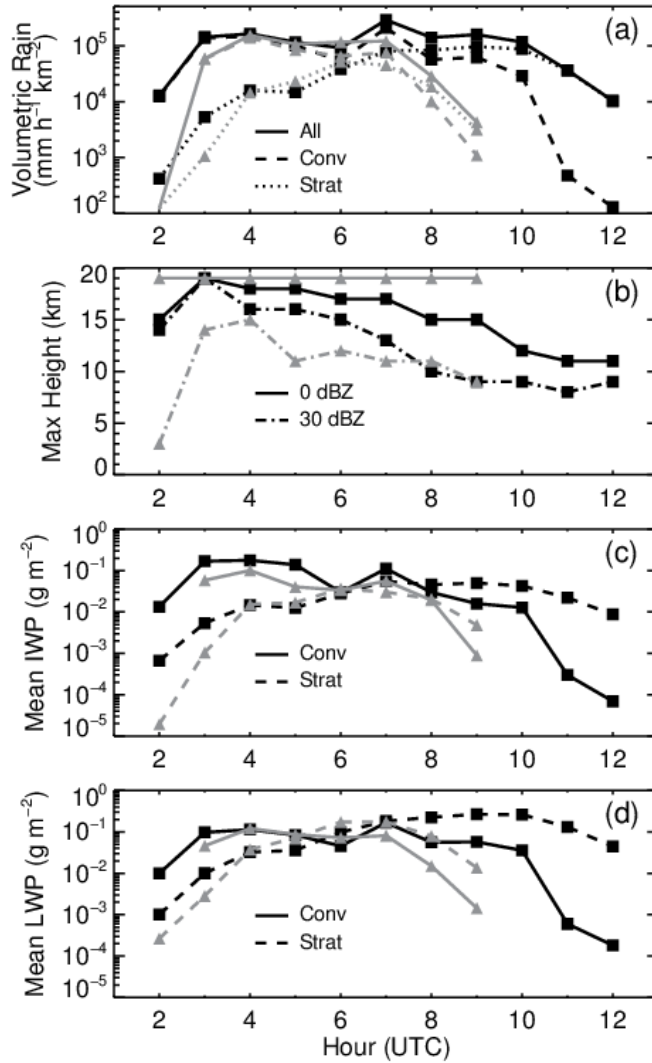


Fig. 5.1. Time series of the (a) total (solid line), convective (dashed line), and stratiform (dotted line) volumetric rain, (b) maximum height of 0- and 30-dBZ (solid and dashed lines, respectively), and mean (c) ice and (d) liquid water path fractions for convective (solid line) and stratiform (dashed line) regions derived using MIT radar data from 8 September (black with squares) and 14 July (gray with triangles) 2006. Note that (a) and (c, d) are displayed with logarithmic ordinate axes.

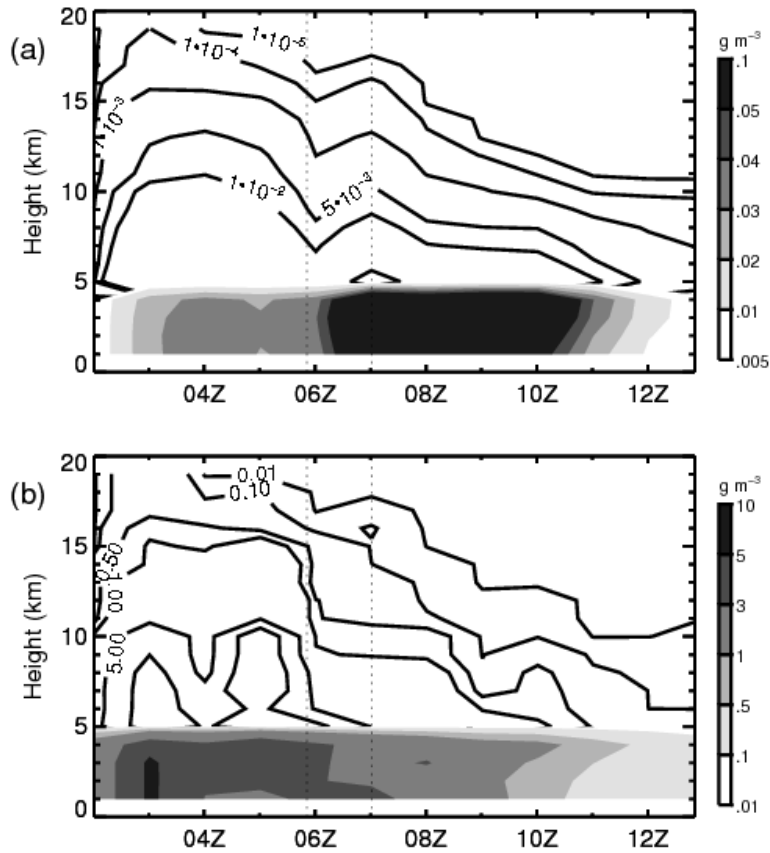


Fig. 5.2. (a) Mean and (b) maximum radar-derived water content during the 8 September 2006 case. Ice water content is open-contoured with intervals of 0.00001, 0.0001, 0.001, 0.005, and 0.01 in (a) and 0.01, 0.1, 0.5, 1.0, 5.0, and 10.0 in (b), while shading corresponds to liquid water content in both. Thin vertical, dotted lines show the approximate time of passage of the system over the radar.

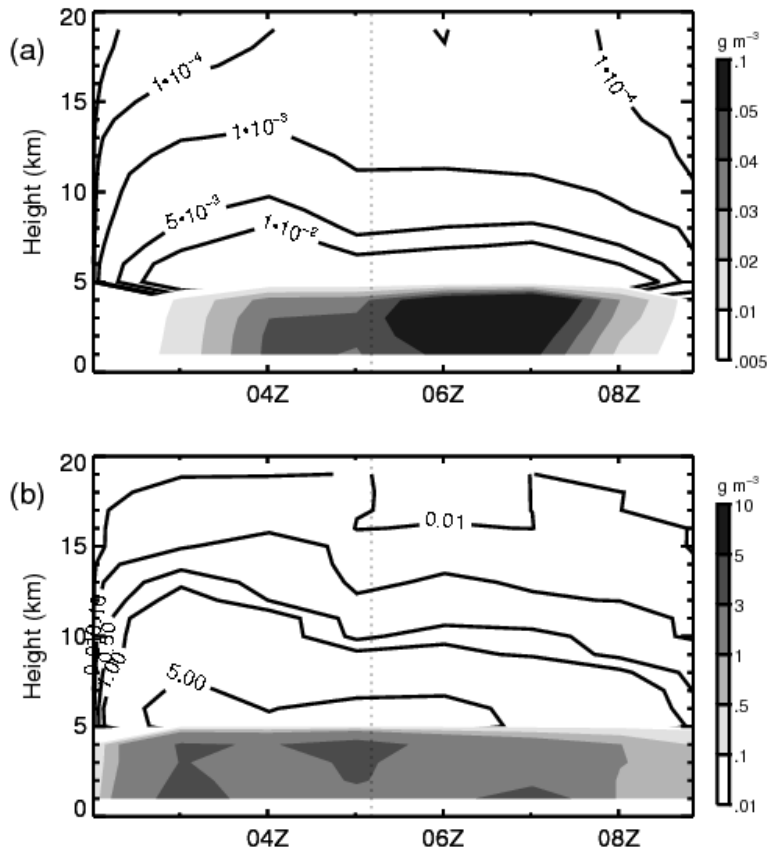


Fig. 5.3. As in Fig. 5.2, except for 14 July 2006.

## CHAPTER 6

### SIMULATION DISCUSSION

Characteristics of the entire model domain were used in the analysis of simulation data. To quantitatively assess simulation performance in comparison to observations a variation of Brier skill score, fractions skill score (FSS), was calculated (Roberts and Lean 2008; May and Lane 2009). Simulation fractions were compared to observed fractions (using reflectivity probability distributions), where the FSS ranged from 0 (no match) to 1 (complete match). Lag analysis of FSS values exhibited better matches when simulations were offset to earlier time periods than observations. A shift of 4 hours was required for the 8 September case, while 6 hours was needed for the 14 July case (Table 6.1).

While some variables were available for both sets of observations and simulations (e.g. reflectivity), analogous variables (e.g. observed IWC and simulated ice hydrometeor mixing ratios) were used to analyze relative trends and distributions between characteristics of observations and simulations. Comparison statistics were derived from smaller domains than the model simulations themselves. Given differences in domain sizes, magnitudes were not expected to correspond directly. However, due to the large size of the sampled MCSs and the fact that MCSs are a conglomerate of many smaller

features (as indicated in Chapter 5), a sub-sample of the most salient features (in this case forward anvil, leading convective line, and trailing stratiform cloud) provided a reasonable basis for comparison of radar observations to the GCE model data.

The probability distribution of rain rate (Fig. 6.1) showed that bulk precipitation intensity was well-simulated for both cases, though with too large a population of rain rates over  $10 \text{ mm h}^{-1}$  and too few small rain rates. Total precipitation was a function of lower stratiform and higher convective rain rates compared to observations (not shown). Time series of maximum reflectivity values (Fig. 6.2) showed general agreement, though high reflectivity values persisted at low-levels within the simulations for a longer time period than observed. This suggested that convective decay may have occurred more slowly in simulations. High reflectivity values ( $\text{dBZ} > 50$ ) were limited to heights near and below the freezing level in the model, similar to Lang et al. (2011). Cases analyzed here were more intense (e.g. higher reflectivity aloft) and larger than those considered in Lang et al. (2011) and displayed a larger relative graupel signature aloft (discussed later). Moderate-to-high reflectivity values ( $20 \leq \text{dBZ} \leq 50$ ) were well represented, though more persistent and less variable (especially vertically) than in observations. Observed echo top heights were higher than simulated, a common occurrence with this model (S. Lang, personal communication), though changes in echo top height were found. While only results for 8 September are shown, the 14 July case displayed similar characteristics. With the temporal adjustments applied from the analysis of FSS values, the simulations provided a successful forecast of important properties of each case.

Contoured frequency-by-altitude diagrams (CFADs; Yuter and Houze 1995) were constructed to explore vertical structure and frequency distributions of reflectivity.

A broader distribution was evident for both simulated cases compared to observations (Figs. 6.3–6.4), especially at low–levels. The shape of observed CFADs exhibited a sharp decrease in reflectivity above the 0°C layer (~ 4.5 km). Brightband signatures (enhanced reflectivity near the melting level) were also evident in both stratiform distributions (Figs. 6.3,6.4c), along with a strong evaporative process below the melting level (shown by the large decrease in reflectivity toward the surface). Simulated convective components (Figs. 6.3,6.4e) produced comparable maxima near the surface and diagonalization (decreasing reflectivity with increasing height) as observed (Figs. 6.3,6.4b). The stratiform component of the 8 September case (Fig. 6.3c) captured the low–level evaporative signature. The most noticeable difference between observations and simulations is the displacement toward lower reflectivity values in the simulations.

Another utility of CFAD plots is their ability to suggest system morphology and microphysical characteristics of convective events. Greater diagonalization, along with the occurrence of a wider spectrum of reflectivity values during the 14 July case were indicative of a system with a greater population of cells in the mature phase than the 8 September case. This corroborated temporal observations discussed in Chapter 4 of the longer–lasting 8 September system. Broader reflectivity distributions aloft for the convective components (Fig. 6.3b) of the 8 September case indicated the presence of larger particles aloft (by continued strong convective cores and associated updrafts) compared to the 14 July case (Fig. 6.4b). The offset of maximum probabilities to lower reflectivity values in the 14 July case for both convective and stratiform CFADs was at least partly due to a larger population of snow in the upper–levels (shown later).

Reflectivity values between 35–40 dBZ occurred at higher elevations (up to 14 km compared to below 8 km) for the 8 September case, suggesting a larger graupel population was present.

To provide further analysis, height–probability frequencies were plotted for HID species (Fig. 6.5) identified using the algorithm described in Chapter 3. In agreement with the above analysis, 14 July showed a larger snow occurrence at upper–levels, though all other ice species (except dry graupel) occurred with higher frequency above 7 km during the 8 September case. Both wet and dry graupel and hail distributions extended further aloft during the 8 September case, contributing to the higher occurrence of reflectivity values aloft noted earlier. Extensive brightband occurrence (melting ice) was present in both cases.

The vertical distribution of these different hydrometeors resulted in unique ice and liquid water mass distributions for each case. Using IWC and LWC calculations, observed vertical distributions may be compared to simulations by way of hydrometeor mixing ratios produced in the model (Fig. 6.6). Modeled cloud water distributions have no observational counterpart for comparison since C–band radar is insensitive to these quantities. Simulated graupel can be compared with MIT radar derived IWC, while simulated snow was compared to IWCs derived from both MIT and WACR data. The cloud radar data sampled both leading anvil and trailing stratiform portions of the convective systems (only leading anvil in the 14 July case) and only reflectivity values up to 10 dBZ were retained. This corresponds to detection of small drizzle droplets, snow, and cloud ice. Therefore there is some overlap when comparing observed IWCs and simulated mixing ratios.

Liquid water was well represented in both distribution and position, located mostly below the melting level ( $\sim 4.5$  km). Simulated graupel for the 8 September case (Fig. 6.6a) exhibited a slower decrease with height than observations, suggesting that too much graupel aloft was produced. Observed IWCs derived from WACR exhibited a bimodal peak, a result of the leading anvil occurring at higher altitudes followed by the trailing stratiform region (Cetrone and Houze 2011). Simulated snow and possibly a small component of drizzle distributions agreed well with the lower peak, which stretched from near 5–10 km. Modeled cloud ice was offset to a lower elevation than observations suggested. Reduced echo top heights were noted in the simulations which would directly affect the height of the cloud ice distribution.

Distributions during the 14 July case (Fig. 6.6b) were somewhat different. Rain was well represented, and graupel distributions corresponded more closely to MIT radar-derived IWC shape. Simulated snow and cloud ice exhibited a stronger bimodal distribution, but unfortunately because only the forward anvil was sampled for this case, observations showed only a distribution aloft. Simulated ice hydrometeors were confined to lower elevations and did not extend to upper levels as seen in observations, suggesting that ice transport to upper-levels was not well represented for this case.

Differences observed in the mean vertical distributions of ice and water mass revealed strengths and weaknesses of the simulations in comparison to observations. It was of interest to analyze the temporal evolution of these variables to determine how well the observed morphology of the systems was represented by the simulations. A frequency of occurrence by height was obtained by combining dry and wet snow, dry and wet graupel and rain and drizzle into three categories (snow, graupel, and rain categories,

respectively) at each time step. The vertical probability of occurrence for each category was calculated. Corresponding simulated mixing ratios were overlaid on the observed probabilities (Fig. 6.7). It was clear that the evolution of snow and graupel corresponded to observations. Simulations for the 14 July case produce more realistic hydrometeor distributions over the time period shown, while 8 September simulations resulted in distributions that ended more abruptly than observed (except for snow).

Simulated rain for the 14 July case was similar to observations, while the 8 September simulation appeared to place the majority of rain water early in the time period with tightly contoured lines. Observations also exhibited a later and broader distribution of liquid water. Simulated graupel occurred at lower elevations during both simulations than indicated by observations. Despite the quickly diminishing simulated graupel during the 8 September period, distribution was well represented for both cases. Simulated snow was better represented during the 8 September case than the 14 July period. In general, the deep vertical extent of the 14 July case was not represented in the model. Because the simulations were driven by large-scale forcing, dependence upon synoptic vertical motion strongly influenced the model. In both cases, there was deep subsidence present between 850–450 hPa, indicative of an environment with decaying deep convection present. Synoptic subsidence became quite strong midway through the 8 September case, which led to the abrupt decline in hydrometeor mixing ratios discussed previously. Simulations used the large-scale forcing without nudging at each sounding time step (6-hourly) and therefore simulations were limited by environmental characteristics associated with mature and decaying convection.

Table 6.1. Mean fraction skills score (FSS) of reflectivity distributions coinciding with observational time period and with model shifted for best agreement. Scores were calculated at each corresponding grid height of MIT radar observations and degraded GCE simulations.

Case	Data points	FSS value with no adjustment	FSS value after optimal time adjustment
8 September	All points	0.44	0.47
	Convective	0.38	0.49
	Stratiform	0.56	0.60
14 July	All points	0.74	0.73
	Convective	0.77	0.90
	Stratiform	0.73	0.72

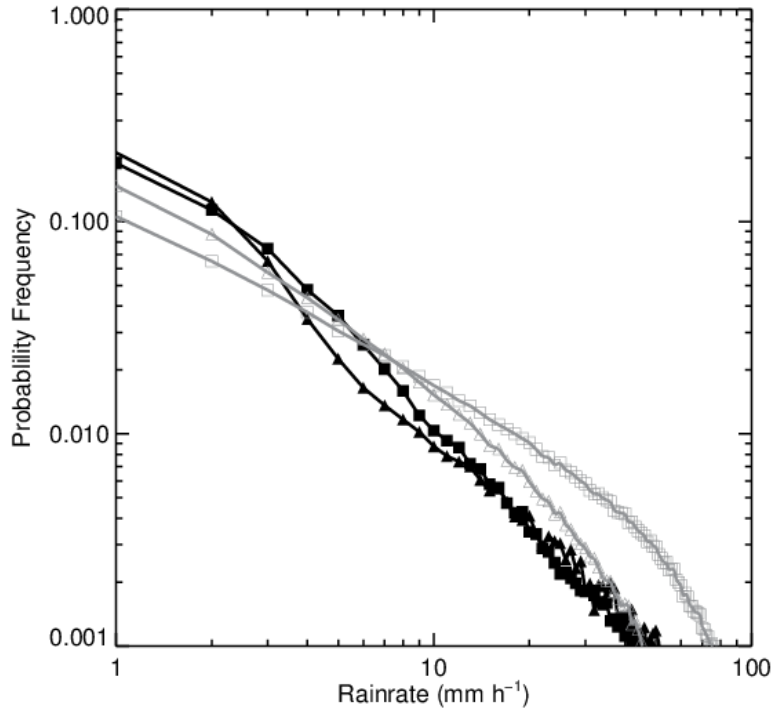


Fig. 6.1. Frequency of occurrence of rain rates estimated by the MIT radar (black) and produced by GCE simulations (gray) for 8 September (square) and 14 July (triangle) 2006.

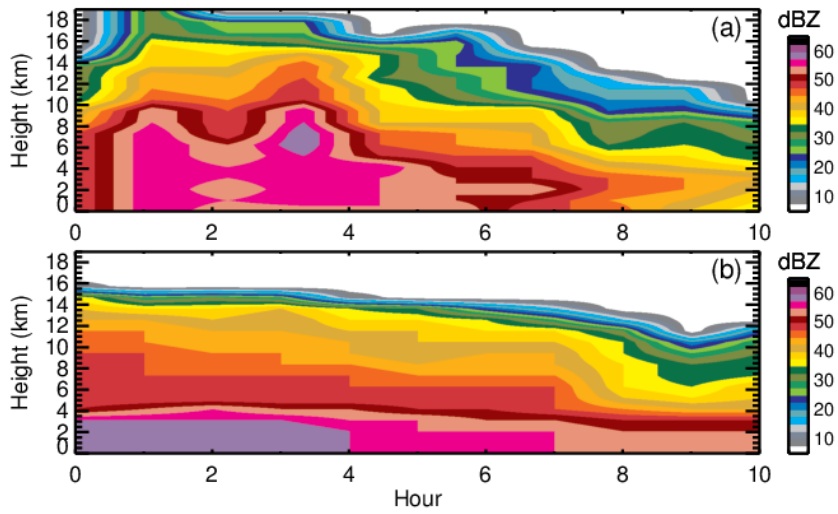


Fig. 6.2. Time evolution of maximum reflectivity values from (a) MIT radar observations and (b) GCE simulations for 8 September 2006. The abscissa corresponds to observed time in the radar domain in (a) and corresponding simulated time period.

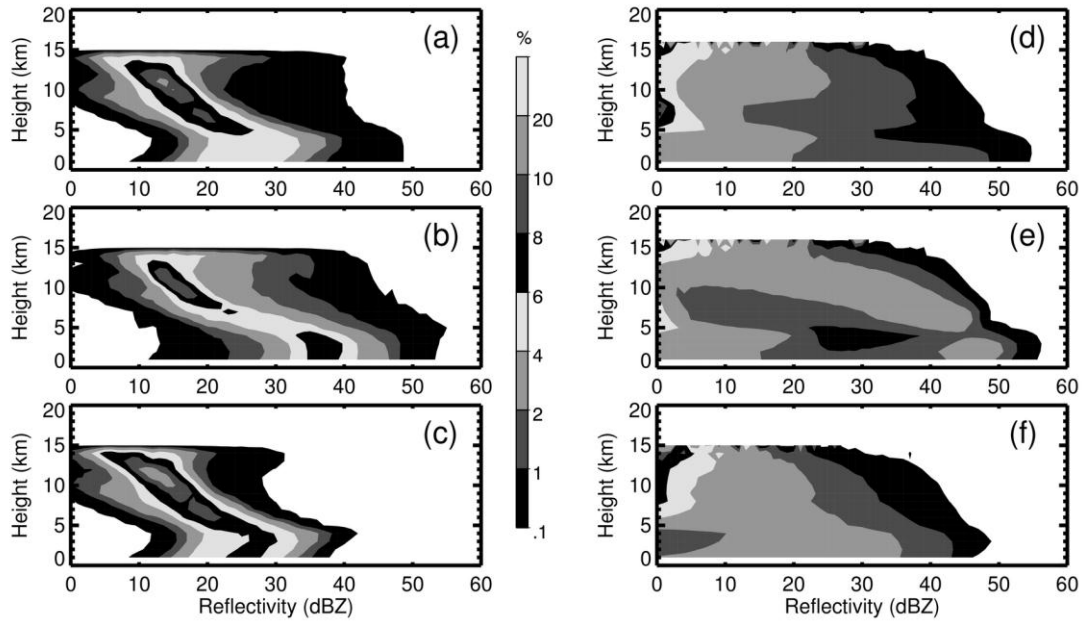


Fig. 6.3. CFADs of reflectivity for (a–c) MIT radar observations and (d–f) GCE simulations for the 8 September 2006 case. From top to bottom, rows correspond to all (a, d), convective (b, e), and stratiform (c, f) classified data. Shaded contour values for all plots are indicated in colorbar, with units of percentage at each vertical level.

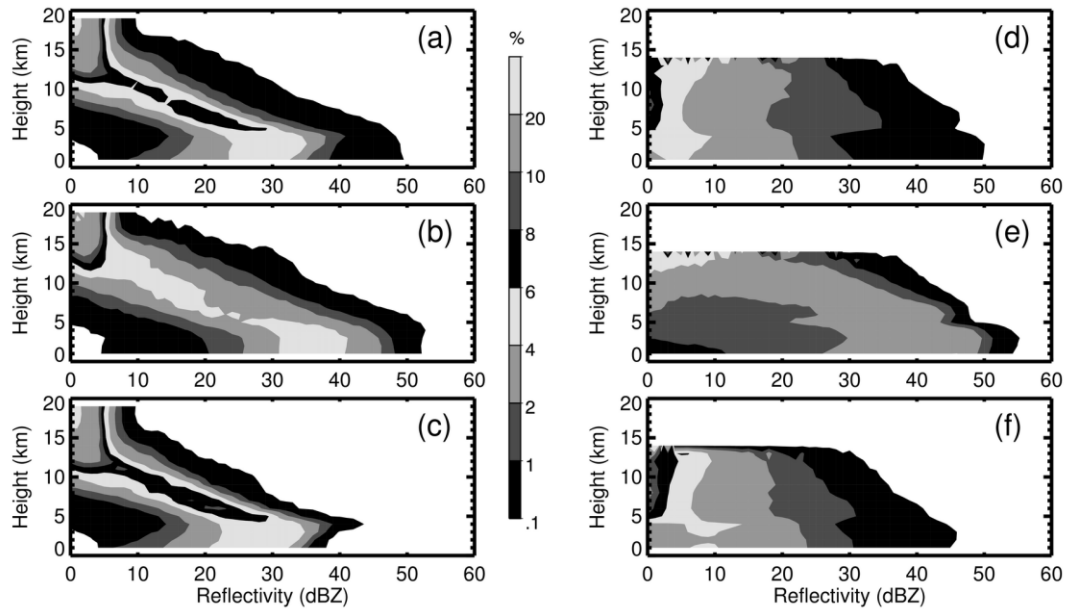


Fig. 6.4. As in Fig. 6.3, except for the 14 July 2006 case.

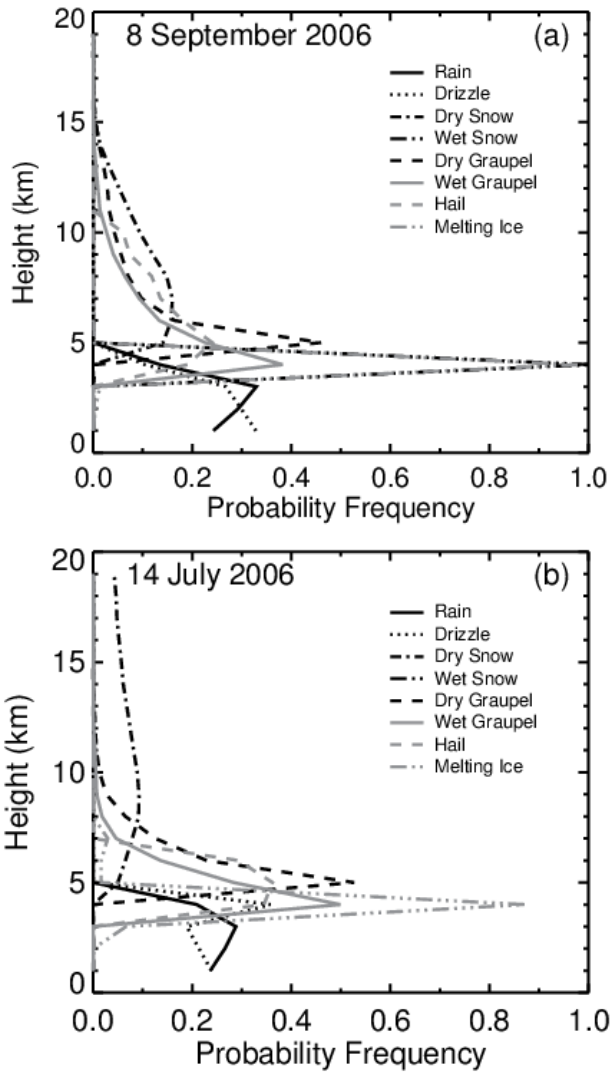


Fig. 6.5. Occurrence frequency –height distributions of identified hydrometeor types using MIT radar reflectivity and temperature profiles for a) 8 September and b) 14 July 2006 cases. Eight hydrometeor types were identified: rain (solid black), drizzle (dotted black), dry (dash-dot black) and wet (dash-dot-dot black) snow, dry (dashed black) and wet (solid gray) graupel, hail (dashed gray), and melting ice (brightband; dash-do-dot gray). Frequencies were calculated as the number of occurrences for each HID species at each vertical level divided by the total number for that specie over the column.

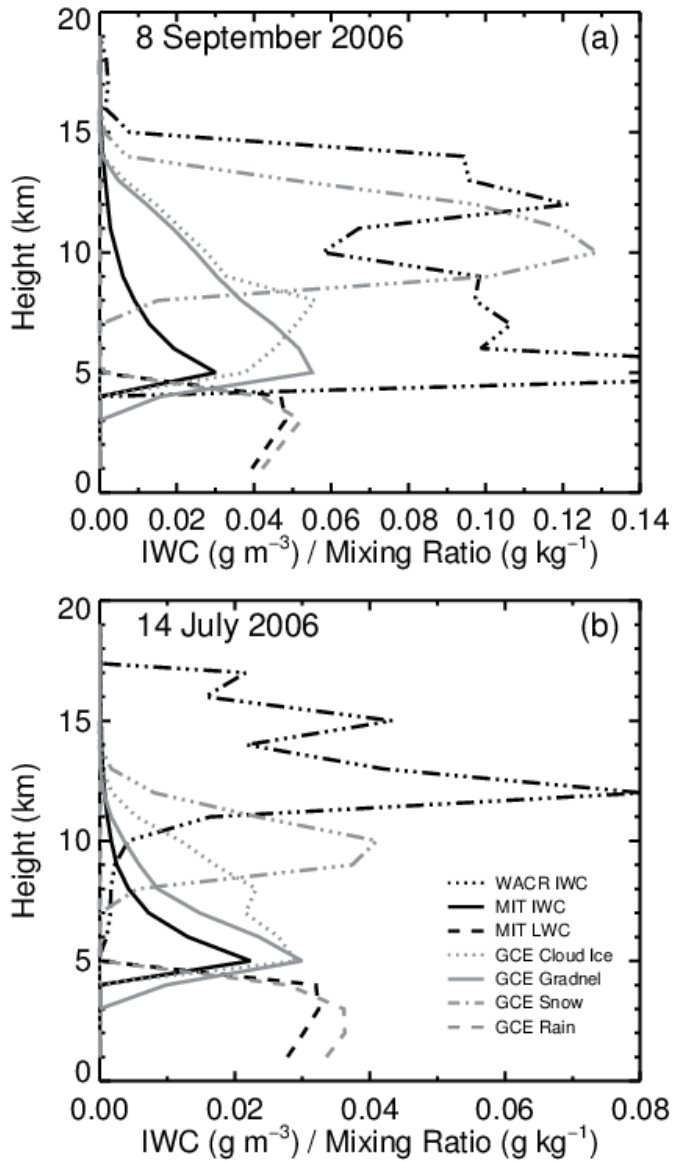


Fig. 6.6. Mean observed liquid (dashed black) and ice (solid and dotted black) water contents calculated using MIT and WACR radar data; and simulated rain (dashed gray), snow (dash-dot gray), graupel (solid gray), and cloud ice (dotted gray) mixing ratios during a) 8 September and b) 14 July 2006 cases.

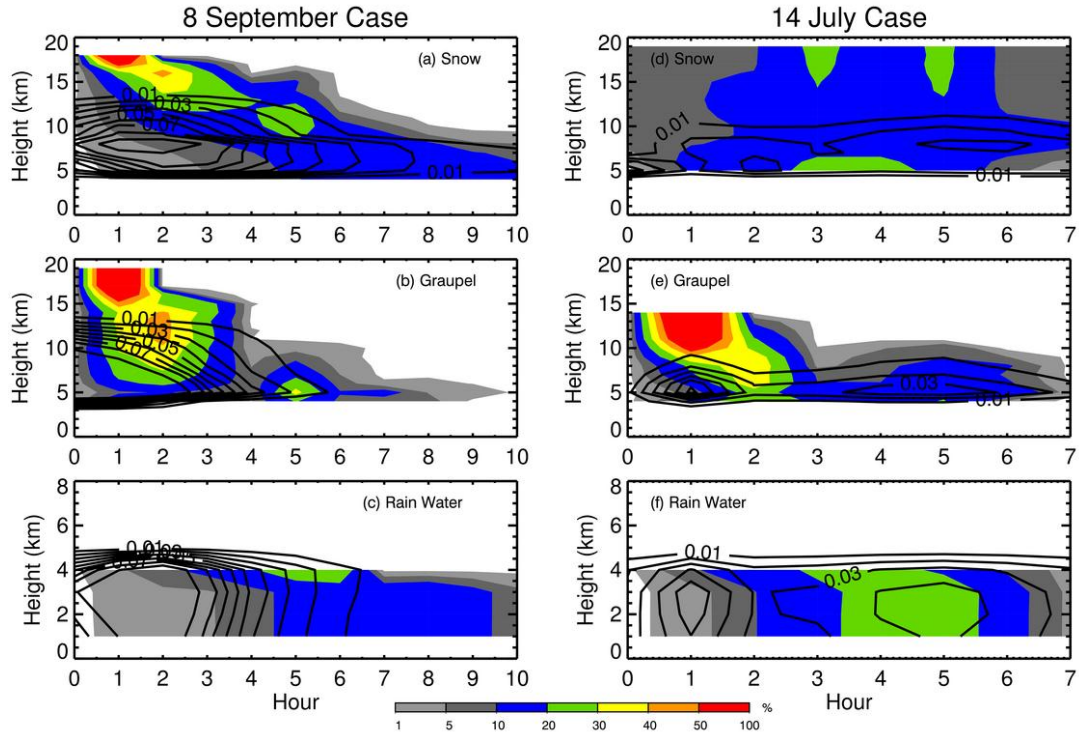


Fig. 6.7. Time evolution of hydrometeors during the 8 September (left column) and 14 July (right column) 2006 cases. Shading denotes probability frequency as a function of height for hydrometeors identified using MIT reflectivity and temperature profiles. Snow and graupel include both wet and dry identified components, while rain includes rain and drizzle hydrometeors. Overlaid are mixing ratios of corresponding hydrometeors with a contour interval of  $0.01 \text{ g kg}^{-1}$ .

## CHAPTER 7

### SUMMARY AND CONCLUSIONS

The 3D Goddard Cumulus Ensemble, a CRM, was used to simulate two West African MCSs during the 2006 WAM season. Model performance was explored through comparison with observational data obtained during the AMMA field campaign. Both MCSs were representative of the spectrum of convective systems that occur during the peak monsoon period. The 8 September case was associated with an AEW trough that later went on to generate Hurricane Helene, while the 14 July case showed no association to AEW synoptic forcing. Guy et al. (2011) showed that MCSs associated with AEWs in this region displayed larger stratiform areas and enhanced convective characteristics (e.g. 30–dBZ echo heights) using ground–based radar data over a limited time period during the same season. Analysis of 13 years of TRMM satellite data indicated similar vertical structures of reflectivity and other convective intensity characteristics, though stratiform area (fraction) was larger (smaller) for AEW–associated systems (Guy and Rutledge 2012). The cases chosen for this study were generally indicative of this behavior.

Both simulations produced convective systems that developed sooner as compared to the observations. Overall system size was underestimated in each case, though the 8 September case was larger than the 14 July, as observed in IR imagery. Reflectivity probability distributions were used to calculate FSS values that indicated

simulations exhibited good skill in reproducing the convective structure of each case. However, time series showed high reflectivity values were present at low-levels longer than observed. Despite the abundance of high reflectivity values, observations showed extremely high reflectivity values ( $> 50$  dBZ) reaching higher elevations (10 km) than simulations (5 km). Simulated bulk precipitation also showed an overestimation (underestimation) of the occurrence of high (low) rain rates.

The 8 September case revealed much larger IWC aloft than the 14 July case, despite the fact that the 14 July system exhibited higher observed echo top heights. Mean ice mass in mid-levels (especially directly above the melting level) was slightly larger for the 14 July case. Vertical profiles comparing mean IWC and LWC calculated from radar data to mean mixing ratios of simulated cloud ice, snow, graupel, and rain indicated good distributive agreement for liquid water mass. The 14 July simulations exhibited a reasonable vertical representation of ice mass, while graupel mass decreased more slowly above the 7 km level than observations during the 8 September simulations. In both cases the lower vertical extent in the simulations negatively affected agreement between simulated cloud ice and IWC derived from cloud radar. Cloud ice appeared at lower elevations for both simulations, with a narrower distribution.

Key features of CFAD distributions for each case were reproduced in simulations, such as stratiform brightband and low-level evaporative signature and diagonalization of all components. Broader distributions of the CFADs were found in the simulations, especially evident in the convective profiles. Higher frequencies in simulated distributions were offset to lower reflectivity values. In the 8 September case, this appeared to be due to an underestimation of graupel in mid-levels, contradictory to mean

profile results. Observed hydrometeor types were identified using a reflectivity and temperature profile algorithm to create a three-dimensional volume estimate. Vertical probability of each category indicated that while the 14 July case exhibited a higher overall probability of graupel, the distribution was confined to lower elevations than the 8 September case. A time series plot of the occurrence of select HID categories overlaid by analogous simulated hydrometeor mixing ratios confirmed that while the timing of graupel (and snow) were generally correct, they were located at lower heights which affected the vertical distribution of ice mass.

Characteristics of the GCE simulations generally agreed well with observations and reproduced the unique aspects of the two distinct MCSs favorably, with a few caveats. Deviations in vertical ice mass distribution existed between observations and simulations. While the microphysical scheme could contribute to these differences, it was also likely that representation of the dynamics of the MCSs also contributed to the deviation, as storm dynamics are closely tied to microphysics. Observed MCS initiation occurred outside the simulated domain and propagated into the study area. Large-scale forcing derived from a sounding network showed that the large-scale environment, while supportive of deep convection, was not optimal. This resulted in a less extensive system, which could affect the distribution of microphysical variables. Previous studies have found that reducing the grid size often results in better representation of the microphysical character of convective systems (e.g. Lang et al. 2007). Microphysics within MCSs can be complex and variable on small spatial scales, therefore decreased grid size can help to resolve some of these features.

Future work should look at the representation of these (or similar) MCSs using a GCM using an embedded CRM with longer simulation time. Results from a CRM that is allowed to simulate the environment, rather than using large-scale forcing would help quantify the effects of model dynamics. Better representation of system initiation would help to understand the contribution of dynamics to the microphysical differences observed in this study. Additionally, the use of a two-moment ice microphysics scheme may help to improve surface precipitation and hydrometeor fall speeds, leading to more realistic simulations. The bulk of previous work has focused on maritime systems. Analysis of a greater number of tropical continental cases would also help to find biases contributed by differences in kinematic (e.g. updraft and downdraft strengths) and therefore microphysical structure between continental and maritime convection.

## REFERENCES

- Agustí-Panareda, A., A. Beljaars, C. Cardinali, I. Genkova, and C. Thorncroft, 2010: Impacts of assimilating AMMA soundings on ECMWF analyses and forecasts. *Wea. Forecasting*, **25**, 1142–1160.
- Barthe, C., N. Asencio, J.-P. Lafore, M. Chong, B. Campistron, and F. Cazenave, 2010: Multi-scale analysis of the 25-27 July 2006 convective period over Niamey: Comparison between Doppler radar observations and simulations. *Quart. J. Roy. Meteor. Soc.*, **136**, 190–208.
- Bolton, D., 1984: Generation and propagation of African squall lines. *Quart. J. Roy. Meteor. Soc.*, **110**, 695–721.
- Carey, L. D., and S. A. Rutledge, 2000: The relationship between precipitation and lightning in tropical island convection: A C-band polarimetric radar study. *Mon. Wea. Rev.*, **128**, 2687–2710.
- Cetrone, J., and R. A. Houze, 2011: Leading and trailing anvil clouds of West African squall lines. *J. Atmos. Sci.*, **68**, 1114–1123.
- D’Amato, N., and T. Lebel, 1998: On the characteristics of the rainfall events in the Sahel with a view to the analysis of climatic variability. *Int. J. Climatol.*, **18**, 955–974.
- DeMott, C. A., and S. A. Rutledge, 1998: The vertical structure of TOGA COARE convection. Part I: Radar echo distributions. *J. Atmos. Sci.*, **55**, 2730–2747.
- Eldridge, R. H., 1957: A synoptic study of West African disturbance lines. *Quart. J. Roy. Meteor. Soc.*, **84**, 468–469.
- Evaristo, R., G. Scialom, N. Viltard, and Y. Lemaître, 2010: Polarimetric signatures and hydrometeor classification of West African squall lines. *Quart. J. Roy. Meteor. Soc.*, **136**, 272–288.
- Fabry, F., and I. Zawadzki, 1995: Long-term radar observations of the melting layer of precipitation and their interpretation. *J. Atmos. Sci.*, **52**, 838–851.

- Faccani, C., F. Rabier, N. Fourrie, A. Agusti-Panareda, F. Karbou, P. Moll, J. –P. Lafore, M. Nuret, F. Hdidou, and O. Bock, 2009: The impacts of AMMA radiosonde data on the French global assimilation and forecast system. *Wea. Forecasting*, **24**, 1268–1286.
- Fink, A. H., D. G. Vincent, and V. Ermert, 2006: Rainfall types in the West African Sudanian zone during the summer monsoon 2002. *Mon. Wea. Rev.*, **134**, 2143–2164.
- Guy, N., S. A. Rutledge, and R. Cifelli, 2011: Radar characteristics of continental, coastal, and maritime convection observed during AMMA/NAMMA. *Quart. J. Roy. Meteor. Soc.*, **137**, 1241–1256.
- Guy, N., and S. A. Rutledge, 2012: Regional Comparison of West African convective characteristics: A TRMM-based climatology. *Quart. J. Roy. Meteor. Soc.*, In press.
- Hamilton, R. A., J. W. Archbold, and C. K. M. Douglas, 1945: Meteorology of Nigeria and adjacent territory. *Quart. J. Roy. Meteor. Soc.*, **71**, 231–264.
- Houze, R. A., M. I. Biggerstaff, S. A. Rutledge, and B. F. Smull, 1989: Interpretation of Doppler weather radar displays of midlatitude mesoscale convective systems. *Bull. Amer. Meteor. Soc.*, **70**, 608–619.
- Janicot, S., C. D. Thorncroft, A. Ali, N. Asencio, G. J. Berry, O. Bock, B. Bourles, G. Caniaux, F. Chauvin, A. Deme, L. Kergoat, J. –P. Lafore, C. Lavaysse, T. Lebel, B. Marticorena, F. Mounier, P. Nedelec, J. –L. Redelsperger, F. Ravegnani, C. E. Reeves, R. Roca, P. De Rosnay, H. Schlager, B. Sultan, M. Tomasini, and A. Ulanovsky, 2008: Large-scale overview of the summer monsoon over West Africa during the AMMA field experiment in 2006. *Ann. Geophys.*, **26**, 2569–2595.
- Johnson, R. H., and P. E. Ciesielski, 2000: Rainfall and radiative heating rates from TOGA COARE atmospheric budgets. *J. Atmos. Sci.*, **57**, 1497–1514.
- Klemp, J. B., and R. B. Wilhelmson, 1978: The simulation of three-dimensional convective storm dynamics. *J. Atmos. Sci.*, **35**, 1070–1096.
- Lafore, J.-P., J.-L. Redelsperger, and G. Jaubert, 1988: Comparison between a three-dimensional simulation and Doppler radar data of a tropical squall line: Transports of mass, momentum, heat, and moisture. *J. Atmos. Sci.*, **45**, 3483–3500.
- Laing, A. G., R. Carbone, V. Levizzani, and J. Tuttle, 2008: The propagation and diurnal cycles of deep convection in northern tropical Africa. *Quart. J. Roy. Meteor. Soc.*, **134**, 93–109.

- Lang, S., W.-K. Tao, J. Simpson, and B. Ferrier, 2003: Modeling of convective–stratiform precipitation processes: Sensitivity to partitioning methods. *J. Appl. Meteor.*, **42**, 505–527.
- Lang, S., W.-K. Tao, J. Simpson, R. Cifelli, S. Rutledge, W. Olson, and J. Halverson, 2007: Improving simulations of convective systems from TRMM LBA: Easterly and westerly regimes. *J. Atmos. Sci.*, **64**, 1141–1164.
- Lang, S. E., W.-K. Tao, X. Zeng, and Y. Li, 2011: Reducing the biases in simulated radar reflectivities from a bulk microphysics scheme: Tropical convective systems. *J. Atmos. Sci.*, **68**, 2306–2320.
- Laurent, H., N. D’Amato, and T. Lebel, 1998: How important is the contribution of the mesoscale convective complexes to the Sahelian rainfall? *Phys. Chem. Earth*, **23**, 629–633.
- Le Barbé, L., and T. Lebel, 1997: Rainfall climatology of the HAPEX-Sahel region during the years 1950-1990. *J. Hydrol.*, **188**, 43–73.
- Lebel, T., D. J. Parker, C. Flamant, B. Bourles, B. Marticorena, E. Mougin, C. Peugeot, A. Diedhiou, J. M. Haywood, J. B. Ngamini, J. Polcher, J. –L. Redelsperger, and C. D. Thorncroft, 2010: The AMMA field campaigns: Multiscale and multidisciplinary observations in the West African region. *Quart. J. Roy. Meteor. Soc.*, **136**, 8–33.
- Lerach, D. G., S. A. Rutledge, C. R. Williams, and R. Cifelli, 2010: Vertical structure of convective systems during NAME 2004. *Mon. Wea. Rev.*, **138**, 1695–1714.
- Liu, H., and V. Chandrasekar, 2000: Classification of hydrometeors based on polarimetric radar measurements: Development of fuzzy logic and neuro-fuzzy systems, and in situ verification. *J. Atmos. Oceanic Technol.*, **17**, 140–164.
- Lucas, C., E. J. Zipser, and B. S. Ferrier, 2000: Sensitivity of tropical West Pacific oceanic squall lines to tropospheric Wind and moisture profiles. *J. Atmos. Sci.*, **57**, 2351–2373.
- Machado, L. A. T., J.-P. Duvel, and M. Desbois, 1993: Diurnal variations and modulation by easterly waves of the size distribution of convective cloud clusters over West Africa and the Atlantic Ocean. *Mon. Wea. Rev.*, **121**, 37–49.
- Mathon, V., H. Laurent, and T. Lebel, 2002: Mesoscale convective system rainfall in the Sahel. *J. Appl. Meteor. Climatol.*, **41**, 1081–1092.
- May, P. T., and T. D. Keenan, 2005: Evaluation of microphysical retrievals from polarimetric radar with wind profiler data. *J. Appl. Meteor.*, **44**, 827–838.

- May, P. T., and T. P. Lane, 2009: A method for using weather radar data to test cloud resolving models. *Quart. J. Roy. Meteor. Soc.*, **16**, 425–432.
- Miller, M. A., and A. Slingo, 2007: The Arm Mobile Facility and its first international deployment: Measuring radiative flux divergence in West Africa. *Bull. Amer. Meteor. Soc.*, **88**, 1229–1244.
- Mohr, C. G., L. Jay Miller, R. L. Vaughan, and H. W. Frank, 1986: The merger of mesoscale datasets into a common Cartesian format for efficient and systematic analyses. *J. Atmos. Oceanic Technol.*, **3**, 143–161.
- Moncrieff, M. W., 1992: Organized Convective Systems: Archetypal dynamical models, mass and momentum flux theory, and parameterization. *Quart. J. Roy. Meteor. Soc.*, **118**, 819–850.
- Nicholls, S. D., and K. I. Mohr, 2010: An analysis of the environments of intense convective systems in West Africa in 2003. *Mon. Wea. Rev.*, **138**, 3721–3739.
- Parker, D. J., 2002: The response of CAPE and CIN to tropospheric thermal variations. *Quart. J. Roy. Meteor. Soc.*, **128**, 119–130.
- Parker, D. J., C. D. Thorncroft, R. R. Burton, and A. Diongue-Niang, 2005: Analysis of the African easterly jet, using aircraft observations from the JET2000 experiment. *Quart. J. Roy. Meteor. Soc.*, **131**, 1461–1482.
- Payne, S. W., and M. M. McGarry, 1977: The relationship of satellite inferred convective activity to easterly waves over West Africa and the adjacent ocean during phase III of GATE. *Mon. Wea. Rev.*, **105**, 413–420.
- Penide, G., V. Giraud, D. Bouniol, P. Dubuisson, C. Duroure, A. Protat, and S. Cautenet, 2010: Numerical simulation of the 7 to 9 September 2006 AMMA mesoscale convective system: Evaluation of the dynamics and cloud microphysics using synthetic observations. *Quart. J. Roy. Meteor. Soc.*, **136**, 304–322.
- Petersen, W. A., H. J. Christian, and S. A. Rutledge, 2005: TRMM observations of the global relationship between ice water content and lightning. *Geophys. Res. Lett.*, **32**, L14819.
- Powell, S. W., X. Zeng, R. A. Houze, and W.-K. Tao, 2011: Heating rates of observed and simulated anvil clouds over Niamey. The 2011 Atmospheric System Research Science Team Meeting, San Antonio, TX.
- Protat, A., J. Delanoë, D. Bouniol, A. J. Heymsfield, A. Bansemmer, and P. Brown, 2007: Evaluation of ice water content retrievals from cloud radar reflectivity and temperature using a large airborne in situ microphysical database. *J. Appl. Meteor. Climatol.*, **46**, 557–572.

- Redelsperger, J.-L., A. Diongue, A. Diedhiou, J.-P. Ceron, M. Diop, J.-F. Gueremy, and J.-P. Lafore, 2002: Multi-scale description of a Sahelian synoptic weather system representative of the West African monsoon. *Quart. J. Roy. Meteor. Soc.*, **128**, 1229–1257.
- Redelsperger, J.-L., C. D. Thorncroft, A. Diedhiou, T. Lebel, D. J. Parker, and J. Polcher, 2006: African monsoon multidisciplinary analysis: An international research project and field campaign. *Bull. Amer. Meteor. Soc.*, **87**, 1739–1746.
- Roberts, N. M., and H. W. Lean, 2008: Scale-selective verification of rainfall accumulations from high-resolution forecasts of convective events. *Mon. Wea. Rev.*, **136**, 78–97.
- Russell, B., E. R. Williams, M. Gosset, F. Cazenave, L. Descroix, N. Guy, T. Lebel, A. Ali, F. Metayer, and G. Quantin, 2010: Radar/rain-gauge comparisons on squall lines in Niamey, Niger for the AMMA. *Quart. J. Roy. Meteor. Soc.*, **136**, 289–303.
- Ruti, P. M., J. E. Williams, F. Hourdin, F. Guichard, A. Boone, P. Van Velthoven, F. Favot, I. Musat, M. Rummukainen, M. Dominguez, M. A. Gaertner, J. –P. Lafore, T. Losada, M. B. Rodriguez de Fonseca, J. Polcher, F. Giorgi, Y. Xue, I. Bouarar, K. Law, B. Josse, B. Barret, X. Yang, C. Mari and A. K. Traore, 2011: The West African climate system: a review of the AMMA model inter-comparison initiatives. *Quart. J. Roy. Meteor. Soc.*, **12**, 116–122.
- Rutledge, S. A., and P. V. Hobbs, 1984: The mesoscale and microscale structure and organization of clouds and precipitation in midlatitude cyclones. XII: A diagnostic modeling study of precipitation development in narrow cold-frontal rainbands. *J. Atmos. Sci.*, **41**, 2949–2972.
- Schwendike, J., and S. C. Jones, 2010: Convection in an African Easterly Wave over West Africa and the eastern Atlantic: A model case study of Helene (2006). *Quart. J. Roy. Meteor. Soc.*, **136**, 364–396.
- Scialom, G., and Y. Lemaître, 2011: Vertical moistening by AMMA mesoscale convective systems. *J. Atmos. Oceanic Technol.*, **28**, 617–639.
- Slingo, A., N. A. Bharmal, G. J. Robinson, J. J. Settle, R. P. Allan, H. E. White, P. J. Lamb, M. I. Lele, D. D. Turner, S. McFarlane, E. Kassianov, J. Barnard, C. Flynn, and M. Miller, 2008: Overview of observations from the RADAGAST experiment in Niamey, Niger: Meteorology and thermodynamic variables. *J. Geophys. Res.*, **113**, 18 PP.
- Soong, S.-T., and Y. Ogura, 1980: Response of tradewind cumuli to large-scale processes. *J. Atmos. Sci.*, **37**, 2035–2050.

- Steiner, M., R. A. Houze, and S. E. Yuter, 1995: Climatological characterization of three-dimensional storm structure from operational radar and rain gauge data. *J. Appl. Meteor.*, **34**, 1978–2007.
- Tao, W.-K., 2007: Cloud Resolving Modeling. *J. Meteor. Soc. Japan*, **85B**, 305–330.
- Tao, W.-K., and J. Simpson, 1993: The Goddard cumulus ensemble model. Part I: Model description. *Terr. Atmos. Oceanic Sci.*, **4**, 35–72.
- Tao, W.-K., J. Simpson, D. Baker, S. Braun, M. –D. Chou, B. Ferrier, D. Johnson, A. Khain, S. Lang, B. Lynn, C. –L. Shie, D. Starr, C. –H. Sui, Y. Wang, and P. Wetzell, 2003: Microphysics, radiation and surface processes in the Goddard Cumulus Ensemble (GCE) model. *Meteor. Atmos. Phys.*, **82**, 97–137.
- Tao, W.-K., W. Lau, J. Simpson, J. –D. Chern, R. Atlas, D. Randall, M. Khairoutdinov, J. –L. Li, D. E. Waliser, J. Jiang, A. Hou, X. Lin, and C. Peters-Lidard, 2009: A multiscale modeling system: Developments, applications, and critical issues. *Bull. Amer. Meteor. Soc.*, **90**, 515–534.
- Tao, W.-K., S. W. Powell, P. Ciesielski, X. Zeng, R. A. Houze, J. Yuan, and R. Johnson, 2011: Numerical Simulations of the AMMA and TWP-ICE Mesoscale Convective Systems. The 2011 Atmospheric System Research Science Team Meeting, San Antonio, TX.
- Tokay, A., A. Kruger, W. F. Krajewski, P. A. Kucera, and A. J. P. Filho, 2002: Measurements of drop size distribution in the southwestern Amazon basin. *J. Geophys. Res.*, **107**, 15 PP.
- Tompkins, A. M., A. Diongue-Niang, D. J. Parker, and C. D. Thorncroft, 2005: The African easterly jet in the ECMWF Integrated Forecast System: 4D-Var analysis. *Quart. J. Roy. Meteor. Soc.*, **131**, 2861–2885.
- Vanvyve, E., N. Hall, C. Messager, S. Leroux, and J.-P. Ypersele, 2008: Internal variability in a regional climate model over West Africa. *Climate Dyn.*, **30**, 191–202.
- Yuter, S. E., and R. A. Houze, 1995: Three-dimensional kinematic and microphysical evolution of Florida cumulonimbus. Part II: Frequency distributions of vertical velocity, reflectivity, and differential reflectivity. *Mon. Wea. Rev.*, **123**, 1941–1963.
- Zawislak, J., and E. J. Zipser, 2010: Observations of seven African easterly waves in the East Atlantic during 2006. *J. Atmos. Sci.*, **67**, 26–43.

- Zeng, X., W.-K. Tao, S. Lang, A. Y. Hou, M. Zhang, and J. Simpson, 2008: On the sensitivity of atmospheric ensembles to cloud microphysics in long-term cloud-resolving model simulations. *J. Meteor. Soc. Japan*, **86A**, 45–65.
- Zeng, X., W.-K., Tao, M. Zhang, A. Y. Hou, S. Xie, S. Lang, X. Li, D. Starr, and X. Li, 2009: A contribution by ice nuclei to global warming. *Quart. J. Roy. Meteor. Soc.*, **135**, 1614–1629.
- Zeng, X., W.-K. Tao, T. Matsui, S. Xie, S. Lang, M. Zhang, D. O’C Starr, and X. Li, 2011: Estimating the ice crystal enhancement factor in the tropics. *J. Atmos. Sci.*, **68**, 1424–1434.

## **PART V: OVERALL SUMMARY AND DISCUSSION**

The West African monsoon (WAM), to a first order, is characterized by low-level moisture migration northward into otherwise dry continental regions. The Saharan heat low (SHL) in the north leads to the convergence of hot, dry northerlies and comparatively cool, moist southwesterly flow originating over the Gulf of Guinea. This strongly baroclinic convergence region is known as the inter-tropical discontinuity (ITD). The associated baroclinicity combined with temperature and moisture meridional gradients across the ITD results in the formation of the mid-level African easterly jet (AEJ), located between 600–700 hPa. Daytime heating over the highlands in the Darfur region provide perturbations near the AEJ entrance leading to the genesis of African easterly waves (AEWs; Thorncroft et al. 2008).

Recent work has shown the WAM system to be even more complex than the largely ‘airmass’ thermodynamic representation used until very recently (Lebel et al. 2011), with the need to understand the greater zonal and meridional variability. Monsoonal flow exhibits a discernible diurnal cycle, with a strong nocturnal low-level jet (LLJ; ~400 m) as the dominant mode of moisture delivery into the Sahel (~12–18°N) region (Lothon et al. 2008) and greater vertical mixing of the monsoon flux during the day (Parker et al. 2005). Extra-tropical dry air intrusions (Roca et al. 2005) and cold surges (Vizy and Cook 2009) have also been noted to influence convective activity.

Surface westerlies (including the aforementioned LLJ) underlie the drier AEJ, providing a strongly-sheared environment. Along with monsoonal moisture, this provides environmental conditions ideal for mesoscale convective system (MCS)

generation and maintenance (Aspliden et al. 1976; Payne and McGarry 1977; Houze and Betts 1981; Barnes and Sieckman 1984; Rowell and Milford 1993; Hodges and Thorncroft 1997; Mohr and Thorncroft 2006). Westward-propagating convective systems exhibit mostly linear (squall line; SLMCS) organization over the continent (e.g. Hamilton et al. 1945; Eldridge 1957; Bolton 1984), while amorphous (non-squall) MCSs dominate maritime populations (Schumacher and Houze 2003, 2006; Fuentes et al. 2008). Northern region convection (northward of 12°N) generally takes the form of highly organized, fast-moving systems. Southern regions (southward of 12°N; influenced by the close proximity of the coastal boundary) are characterized by slow-moving, smaller, and less organized systems during the peak of the WAM (July–September), with more highly organized systems surrounding the peak monsoon time period.

Phenomena associated with the WAM extend across spatial and temporal scales, with apparent two-way interaction (e.g. Redelsperger et al. 2002) between spatial scales. Many studies have shown the modulation of deep convection by AEWs (Carlson 1969; Burpee 1974; Duvel 1990; Diedhiou et al. 1999; Fink and Reiner 2003; and many others). Modification of the large-scale environment via MCSs may occur through the transport of moisture (Lafore et al. 1988) and momentum (Moncrieff 1992) or the reinforcement of cyclonic rotation of an AEW trough (Barthe et al. 2010). Previous studies concerning deep convection and AEW interaction focused on the composite view of an AEW introduced by Reed et al. (1977) and rarely considered events that were not associated with an AEW. Though MCSs have been noted to occur and form with no AEW forcing (Fink et al. 2006; Laing et al. 2008), very little work has been done to characterize differences between MCSs in each regime.

A study of 29 days of ground-based radar data collected at the peak of the WAM during the African Monsoon Multidisciplinary Analyses (AMMA) field campaign in 2006 examined both the difference between three distinct geographical locations (continental, coastal, and maritime) along a common latitude; and the differences between MCSs at each location occurring in association with an AEW trough and when no AEW forcing was present (Guy et al. 2011). Thermodynamic environments exhibited distinct distributions for each location, important for determining convective characteristics. Conditions at each location were generally favorable for deep convection, with more highly organized linear morphology observed at the coastal and continental sites. Despite similar median low-level vertical shear values at each location, the presence of an LLJ at the coastal and continental sites resulted in distributions skewed toward larger easterly shear, enhancing the probability of linear MCSs (confirmed by the radar observations).

When AEWs were present, differences in convective available potential energy (CAPE) and convective inhibition (CIN) were evident. Decreased CAPE and a weaker LLJ was observed at the coast during the AEW regime, though low-level shear actually increased. Precipitation did not change substantially between AEW and no-wave regimes. This suggested that MCSs at the coastal site (which did not substantially decrease in number when no AEW was present) evidently drew upon buoyancy in the absence of shear to maintain MCS precipitation efficiency. Overall precipitation volume increased over land and slightly decreased over water. When divided into convective and stratiform components, results were more complex.

At the coastal and continental sites, observed MCS area increased; a result of larger stratiform shields. Convective precipitation increased as well, and in the continental case larger populations of convective cells were identified. A larger population of convective cells indicated the possibility for enhanced stratiform growth due to increasing ice and water mass transfer into the stratiform region from a larger number of convective updrafts. These results suggested that microphysical and precipitation properties may vary as a function of synoptic regime. Despite the observed variations between AEW and no-wave characteristics, differences between regions were more striking than AEW and no-wave regime variability. Convection over the continent and at the coast was more intense (derived from metrics such as vertical reflectivity profiles and 30-dBZ echo top heights) than the maritime counterpart. Differences in MCS occurrence and characteristics (e.g. convective and stratiform contributions to precipitation and size) were also more pronounced according to geographic region.

These results were in agreement with findings from recent field projects which have increased awareness of the inhomogeneity of meridional and zonal precipitation and convective characteristics and underscore the need to improve our understanding and representation of the WAM system. Herrmann and Mohr (2011) have recently refined seasonal precipitation regimes throughout Africa, providing a much more detailed and quantitative representation of variability. Previous studies of mesoscale characteristics have illustrated regional differences using satellite data over Africa (Nesbitt et al. 2000; Geerts and Dejene 2005; Zipser et al. 2006; Fuentes et al. 2008; Liu et al. 2008, and others), though the diversity of smaller regions was not explicitly investigated.

A 13-year climatology of convective characteristics from May – October using precipitation radar and passive microwave data from the NASA Tropical Rainfall Measuring Mission (TRMM) satellite confirmed that regionality dominated AEW regime (and no-wave) variability of mesoscale convection in West Africa (Guy and Rutledge 2012). Seven  $6^\circ \times 6^\circ$  boxes defined regions that varied latitudinally (northern regions were centered about  $15^\circ\text{N}$  and southern regions were centered about  $9^\circ\text{N}$ ) and longitudinally (four continental, one coastal, and two maritime).

As in previous studies, continental systems were more vigorous than their maritime counterparts (Nesbitt et al. 2000; Geerts and Dejene 2005; Schumacher and Houze 2006; Zipser et al. 2006; Fuentes et al. 2008). Storms over land displayed higher storm top and 30-dBZ echo top heights, lower minimum 37- and 85-GHz brightness temperatures, a higher occurrence of storms extending above 10 km, and mean convective vertical profiles of reflectivity offset to higher values throughout the profiles. These characteristics all point to more intense convection. Stratiform reflectivity profiles were similar for all regions, except the southern maritime region where lower reflectivity was observed below the  $0^\circ\text{C}$  level ( $\sim 4.5$  km). As in Schumacher and Houze (2003, 2006) stratiform fraction decreased from the Atlantic eastward. Ice and liquid water path fractions (defined as ice or liquid water path divided by the sum of both components, respectively) revealed that ice precipitation processes played a greater role in northern regions when compared to southern counterparts. Maritime and the southwest continental regions showed a larger dependence on warm-rain processes in precipitation production.

Though the spectrum of characteristics suggested less variability between AEW phases and no-wave systems, results were used to characterize convection during each regime. The trough phase displayed a widespread convective signature, while the southerly phase generally indicated more isolated, intense convection. Convective characteristics during the ridge phase were slightly more intense than during the trough phase. A decrease in convective strength was observed during the northerly AEW phase. Convection occurring when no AEW was identified was similar to that in the southerly AEW regime, though characteristics corresponding to an increased stratiform component were observed.

Enhancement of the convective portions of MCSs was observed over land during the southerly and ridge regimes. Area distributions did not vary greatly between AEW regimes, however stratiform fractions did, which implies that varying latent heating profiles may exist between convective systems as a function of AEW regime. These properties led to differences in vertical profiles of liquid and ice water content between AEW regimes.

It is important for numerical weather prediction (NWP) and global climate (GCMs) models to represent these observed differences in order to provide meaningful mesoscale variability for long-term simulations. Historically, NWP models have performed poorly in representing characteristics of the WAM (e.g. Cook and Vizu 2006; Ruti et al. 2011), though progress is being made. Improved representation of AEWs has recently been achieved in GCMs; however, challenges still exist to understand the mechanisms driving discrepancies in simulations (Ruti et al. 2011). Despite

improvements in synoptic features, smaller-scale (mesoscale) variability is less reproducible (e.g. Vanvyve et al. 2008).

State-of-the-art GCMs, employing cloud-resolving models (CRMs) to simulate convective events, now utilize 1 km horizontal grid spacing. The Goddard Cumulus Ensemble (GCE) model (Tao and Simpson 1993; Tao et al. 2003) is an example of a CRM that uses an ensemble approach to represent the vertical structure of simulated clouds through a statistical representation of cloud and precipitation properties.

Improved representation of mesoscale variability is dependent upon capturing convective property variability approaching and down to the mesoscale.

A 3D version of the GCE model (Zeng et al. 2009, 2011), with parameterization to increase ice crystal concentrations, was used to simulate two MCS cases that occurred when an AEW was present (8 September 2006) and when no AEW was present (14 July 2006). These cases were typical of the similarities and differences found in Guy et al. (2011) and Guy and Rutledge (2012). The GCE model performance was investigated through comparison with observational data obtained during the AMMA field campaign.

Simulations produced convection earlier than observed for both cases. System size was underestimated in both cases, though relative observed differences were captured by the GCE. Simulations exhibited generally good skill in reproducing vertical convective structure, though large reflectivity values did not reach the vertical extent observed by ground-based radar. Reflectivity values tended to be higher in model simulations compared to the observations. Comparisons showed that the vertical distribution of liquid water mass was well represented, while ice mass distributions exhibited less agreement. Graupel distributions in the AEW case were too large above 7

km. Cloud ice distributions occurred too low in simulations due to reduced vertical extent in comparison to observations. The temporal evolution of snow, graupel, and rain showed good agreement for both cases, though located at lower elevations than observed.

Despite the caveats discussed above, GCE simulations generally agreed well with observations and reproduced the unique aspects of the two distinct MCSs favorably. The temporal distribution of simulated hydrometeors aligned well with observations; and water mass below the freezing level corresponded to observed vertical distributions. The stratiform brightband feature and degree of diagonalization indicated in contoured frequency-by-altitude diagrams (CFAD) were also well represented. Similar patterns of observed variability of the above properties between cases were also apparent in the simulations. Differences were likely a combination of the large-scale forcing used to drive simulations, ice microphysics parameterizations that continue to be modified to produce realistic strong tropical convection, and model dynamics which influence storm microphysics through the modification of storm dynamics.

Future work should include a detailed analysis of environments preceding, during and following AEW passage across West Africa. In addition, detailed study of MCS kinematics in multiple regions could help to illuminate feedback variability and scale interactions; and lead to a better understanding of the importance of various processes (e.g. momentum transfer, latent heating) in different locations. Expanding the analysis of climatological convective characteristics to the rest of Africa could help to understand microphysical processes in precipitation production and convective maintenance over a wide variety of regions, including tropical and mid-latitude (e.g. South Africa). These data would also be useful for comparison to future model simulations. Further

development of the GCE microphysical package could expand to other tropical continental locations to validate ice crystal concentrations used in the simulation portion of this research. It would also be useful to determine the origin of the reduced height of simulated convection now present in the GCE.

## REFERENCES

- Aspliden, C., Y. Tourre, and J. Sabine, 1976: Some climatological aspects of West African disturbance lines during GATE. *Mon. Wea. Rev.*, **104**, 1029–1035.
- Barnes, G. M., and K. Sieckman, 1984: The environment of fast- and slow-moving tropical mesoscale convective cloud lines. *Mon. Wea. Rev.*, **112**, 1782–1794.
- Barthe, C., N. Asencio, J.-P. Lafore, M. Chong, B. Campistron, and F. Cazenave, 2010: Multi-scale analysis of the 25-27 July 2006 convective period over Niamey: Comparison between Doppler radar observations and simulations. *Quart. J. Roy. Meteor. Soc.*, **136**, 190–208.
- Bolton, D., 1984: Generation and propagation of African squall lines. *Quart. J. Roy. Meteor. Soc.*, **110**, 695–721.
- Burpee, R. W., 1974: Characteristics of North African easterly waves during the summers of 1968 and 1969. *J. Atmos. Sci.*, **31**, 1556–1570.
- Carlson, T. N., 1969: Some remarks on African disturbances and their progress over the tropical Atlantic. *Mon. Wea. Rev.*, **97**, 716–726.
- Cook, K. H., and E. K. Vizy, 2006: Coupled model simulations of the West African monsoon system: Twentieth- and twenty-first-century simulations. *J. Climate*, **19**, 3681–3703.
- Diedhiou, A., S. Janicot, A. Viltard, P. de Felice, and H. Laurent, 1999: Easterly wave regimes and associated convection over West Africa and tropical Atlantic: results from the NCEP/NCAR and ECMWF reanalyses. *Climate Dyn.*, **15**, 795–822.
- Duvel, J. P., 1990: Convection over tropical Africa and the Atlantic Ocean during northern summer. Part II: Modulation by easterly waves. *Mon. Wea. Rev.*, **118**, 1855–1868.
- Eldridge, R. H., 1957: A synoptic study of West African disturbance lines. *Quart. J. Roy. Meteor. Soc.*, **84**, 468–469.

- Fink, A. H., and A. Reiner, 2003: Spatiotemporal variability of the relation between African easterly waves and West African squall lines in 1998 and 1999. *J. Geophys. Res.*, **108**, 17 PP.
- Fink, A. H., D. G. Vincent, and V. Ermert, 2006: Rainfall types in the West African Sudanian zone during the summer monsoon 2002. *Mon. Wea. Rev.*, **134**, 2143–2164.
- Fuentes, J. D., B. Geerts, T. Dejene, P. D’Odorico, and E. Joseph, 2008: Vertical attributes of precipitation systems in West Africa and adjacent Atlantic Ocean. *Theor. Appl. Climatol.*, **92**, 181–193.
- Geerts, B., and T. Dejene, 2005: Regional and diurnal variability of the vertical structure of precipitation systems in Africa based on spaceborne radar data. *J. Climate*, **18**, 893–916.
- Guy, N., S. A. Rutledge, and R. Cifelli, 2011: Radar characteristics of continental, coastal, and maritime convection observed during AMMA/NAMMA. *Quart. J. Roy. Meteor. Soc.*, **137**, 1241–1256.
- Guy, N., and S. A. Rutledge, 2012: Regional comparison of West African convective characteristics: A TRMM-based climatology. *Quart. J. Roy. Meteor. Soc.*, In press.
- Hamilton, R. A., J. W. Archbold, and C. K. M. Douglas, 1945: Meteorology of Nigeria and adjacent territory. *Quart. J. Roy. Meteor. Soc.*, **71**, 231–264.
- Herrmann, S. M., and K. I. Mohr, 2011: A continental-scale classification of rainfall seasonality regimes in Africa based on gridded precipitation and land surface temperature products. *J. Appl. Meteor. Climatol.*, **50**, 2504–2513.
- Hodges, K. I., and C. D. Thorncroft, 1997: Distribution and statistics of African mesoscale convective weather systems based on the ISCCP Meteosat imagery. *Mon. Wea. Rev.*, **125**, 2821–2837.
- Houze, R. A., and A. K. Betts, 1981: Convection in GATE. *Rev. Geophys.*, **19**, 541–576.
- Lafore, J.-P., J.-L. Redelsperger, and G. Jaubert, 1988: Comparison between a three-dimensional simulation and Doppler radar data of a tropical squall line: Transports of mass, momentum, heat, and moisture. *J. Atmos. Sci.*, **45**, 3483–3500.
- Laing, A. G., R. Carbone, V. Levizzani, and J. Tuttle, 2008: The propagation and diurnal cycles of deep convection in northern tropical Africa. *Quart. J. Roy. Meteor. Soc.*, **134**, 93–109.

- Lebel, T., D. J. Parker, C. Flamant, B. Bourles, B. Marticorena, E. Mougin, C. Peugeot, A. Diedhiou, J. M. Haywood, J. B. Ngamini, J. Polcher, J. -L. Redelsperger, and C. D. Thorncroft, 2011: The AMMA field campaigns: accomplishments and lessons learned. *Quart. J. Roy. Meteor. Soc.*, **12**, 123–128.
- Liu, C., E. J. Zipser, D. J. Cecil, S. W. Nesbitt, and S. Sherwood, 2008: A cloud and precipitation feature database from nine years of TRMM observations. *J. Appl. Meteor. Climatol.*, **47**, 2712–2728.
- Lothon, M., F. Saïd, F. Lohou, and B. Campistron, 2008: Observation of the diurnal cycle in the low troposphere of West Africa. *Mon. Wea. Rev.*, **136**, 3477–3500.
- Mohr, K. I., and C. D. Thorncroft, 2006: Intense convective systems in West Africa and their relationship to the African easterly jet. *Quart. J. Roy. Meteor. Soc.*, **132**, 163–176.
- Moncrieff, M. W., 1992: Organized Convective Systems: Archetypal dynamical models, mass and momentum flux theory, and parameterization. *Quart. J. Roy. Meteor. Soc.*, **118**, 819–850.
- Nesbitt, S. W., E. J. Zipser, and D. J. Cecil, 2000: A census of precipitation features in the Tropics using TRMM: Radar, ice scattering, and lightning observations. *J. Climate*, **13**, 4087–4106.
- Parker, D. J., C. D. Thorncroft, R. R. Burton, and A. Diongue-Niang, 2005: Analysis of the African easterly jet, using aircraft observations from the JET2000 experiment. *Quart. J. Roy. Meteor. Soc.*, **131**, 1461–1482.
- Payne, S. W., and M. M. McGarry, 1977: The relationship of satellite inferred convective activity to easterly waves over West Africa and the adjacent ocean during phase III of GATE. *Mon. Wea. Rev.*, **105**, 413–420.
- Redelsperger, J.-L., A. Diongue, A. Diedhiou, J.-P. Ceron, M. Diop, J.-F. Gueremy, and J.-P. Lafore, 2002: Multi-scale description of a Sahelian synoptic weather system representative of the West African monsoon. *Quart. J. Roy. Meteor. Soc.*, **128**, 1229–1257.
- Reed, R. J., D. C. Norquist, and E. E. Recker, 1977: The structure and properties of African wave disturbances as observed during phase III of GATE. *Mon. Wea. Rev.*, **105**, 317–333.
- Roca, R., J.-P. Lafore, C. Piriou, and J.-L. Redelsperger, 2005: Extratropical dry-air intrusions into the West African monsoon midtroposphere: An important factor for the convective activity over the Sahel. *J. Atmos. Sci.*, **62**, 390–407.

- Rowell, D. P., and J. R. Milford, 1993: On the generation of African squall lines. *J. Climate*, **6**, 1181–1193.
- Ruti, P. M., J. E. Williams, F. Hourdin, F. Guichard, A. Boone, P. Van Velthoven, F. Favot, I. Musat, M. Rummukainen, M. Dominguez, M. A. Gaertner, J. –P. Lafore, T. Losada, M. B. Rodriguez de Fonseca, J. Polcher, F. Giorgi, Y. Xue, I. Bouarar, K. Law, B. Josse, B. Barret, X. Yang, C. Mari and A. K. Traore, 2011: The West African climate system: a review of the AMMA model inter-comparison initiatives. *Quart. J. Roy. Meteor. Soc.*, **12**, 116–122.
- Schumacher, C., and R. A. Houze, 2003: Stratiform rain in the Tropics as seen by the TRMM precipitation radar. *J. Climate*, **16**, 1739–1756.
- Schumacher, C., and R. A. Houze, 2006: Stratiform precipitation production over sub-Saharan Africa and the tropical East Atlantic as observed by TRMM. *Quart. J. Roy. Meteor. Soc.*, **132**, 2235–2255.
- Tao, W.-K., and J. Simpson, 1993: The Goddard cumulus ensemble model. Part I: Model description. *Terr. Atmos. Oceanic Sci.*, **4**, 35–72.
- Tao, W.-K. J. Simpson, D. Baker, S. Braun, M. –D. Chou, B. Ferrier, D. Johnson, A. Khain, S. Lang, B. Lynn, C. –L. Shie, D. Starr, C. –H. Sui, Y. Wang, and P. Wetzell, 2003: Microphysics, radiation and surface processes in the Goddard Cumulus Ensemble (GCE) model. *Meteor. Atmos. Phys.*, **82**, 97–137.
- Thorncroft, C. D., N. M. J. Hall, and G. N. Kiladis, 2008: Three-dimensional structure and dynamics of African easterly waves. Part III: Genesis. *J. Atmos. Sci.*, **65**, 3596–3607.
- Vanvyve, E., N. Hall, C. Messenger, S. Leroux, and J.-P. Ypersele, 2008: Internal variability in a regional climate model over West Africa. *Climate Dyn.*, **30**, 191–202.
- Vizy, E. K., and K. H. Cook, 2009: A mechanism for African monsoon breaks: Mediterranean cold air surges. *J. Geophys. Res.*, **114**, 19 PP.
- Zeng, X. W.-K., Tao, M. Zhang, A. Y. Hou, S. Xie, S. Lang, X. Li, D. Starr, and X. Li, 2009: A contribution by ice nuclei to global warming. *Quart. J. Roy. Meteor. Soc.*, **135**, 1614–1629.
- Zeng, X., W.-K. Tao, T. Matsui, S. Xie, S. Lang, M. Zhang, D. O’C Starr, and X. Li, 2011: Estimating the ice crystal enhancement factor in the tropics. *J. Atmos. Sci.*, **68**, 1424–1434.
- Zipser, E. J., C. Liu, D. J. Cecil, S. W. Nesbitt, and D. P. Yorty, 2006: Where are the most intense thunderstorms on earth? *Bull. Amer. Meteor. Soc.*, **87**, 1057–1071.